Thesis: Zhibo Qu (2019) " SOI Waveguide Integrated Graphene Mid-Infrared Detector", University of Southampton, Faculty of Engineering ans Physical Sciences, Optoelectronics Research Centre, PhD Thesis, pagination.

Data: Zhibo Qu (2019), SOI Waveguide Integrated Graphene Mid-Infrared Detector. https://doi.org/10.5258/SOTON/D1100

UNIVERSITY OF SOUTHAMPTON

FACULTY OF ENGINEERING AND PHYSICAL SCIENCES
Optoelectronics Research Centre

SOI Waveguide Integrated Graphene Mid-Infrared Detector

by

Zhibo Qu

Thesis for the degree of Doctor of Philosophy

October 2019

UNIVERSITY OF SOUTHAMPTON

FACULTY OF ENGINEERING AND PHYSICAL SCIENCES

Optoelectronics Research Centre

Doctor of Philosophy

SOI WAVEGUIDE INTEGRATED GRAPHENE MID-INFRARED DETECTOR

by Zhibo Qu

ABSTRACT

Mid-infrared group IV photonics is a vibrant field, which aims to migrate techniques used for near-infrared silicon photonics to longer wavelengths in order to build photonic integrated lab-on-a-chip sensors that can be applied in areas such as remote sensing, homeland security, medical diagnostics or environmental monitoring.

In order to create mid-infrared lab-on-a-chip sensors, both passive and active devices are required. Passive deceives for wavelengths up to 4 μm can be created using the silicon-on-insulator waveguide platform, which is commonly used in the near-infrared, and is compatible with the standard and developed near-infrared fabrication techniques.

Graphene is a 2-D material that has excellent electronic and optical properties. It can interact with light from microwave to ultraviolet wavelengths, making it a potential candidate for light detection applications over a wide spectral range.

By taking advantage of the wide transparency range of group IV platforms in the mid-infrared and the 2-D nature of graphene, this project is aiming to investigate the integration of graphene mid-infrared photodetectors with silicon waveguides.

In this project, two different designs of SOI waveguide integrated graphene mid-infrared photodetectors have been fabricated and characterised, exhibiting responsivities of 2.2 mA/W at the 3.8 μm wavelength, which is the longest wavelength demonstration up date of waveguide integrated graphene photodetection. In addition, these devices exhibited photodetection at wavelengths up to 7.7 μm, confirming that graphene is a promising detector candidate for even longer wavelengths.

Contents

List of Figures

List of Tables

Acknowledgements

This project is the result of a multitude of meetings, fortunate coincidences, experiments, encouragement and having got to know a group of people which I am more than happy to acknowledge in the following.

First of all, my grateful thanks will go to Professor Goran Mashanovich, my principal supervisor, who accepted me to this project and for his countless help and unfathomable support in my work. He has been an excellent supervisor and giving me the right direction and encouragement all the time. Thanks also to my co-supervisors, Dr. Milos Nedljkovic and Professor Graham Reed and for giving me fruitful suggestion during the whole project. Especially thanks to Milos for co-supervision and bringing me into this field, invaluable support, all the lab work, and the scientific discussion.

All of the members in the Silicon Photonics group supported me on countless moments and they all helped me with things big or small. I would like to thank in particular Dr. Scott Reynolds, Dr. Ali Khokhar, Dr. Jordi Soler Penades, Yangbo Wu, for the kindness support during the last few years in the labs and cleanroom and being my valuable friends and colleagues. I would also like to thank Lorenzo Mastronardi, Wei Cao, Dr. Callum Littlejohns, Ahmed Osman, Dr. Dave Rowe, Callum Stirling, Lauren Reid, Bharat Pant, Dr. Mehdi Banakar and Dr Vinita Mittal.

Part of the results of this project is the result of collaborations from internal and external. Thanks to Dr. Junjia Wang from the University of Cambridge and Nikolaos Aspiotis and Dr. Chung Che Huang for their excellent job.

I received unmeasurable support from my lovely friends: Feimeng Cao, Jingyu Song, Junjie Gu, Jinxiao Wu, Hua Liu and Huaiyang Zeng thank you all for comfort and help to get through all the difficulties during the last years. My sincerest gratitude goes to my beloved family for their unconfitional love and faith.

Declaration of Authorship

I, Zhibo Qu , declare that the thesis entitled *SOI Waveguide Integrated Graphene Mid-Infrared Detector* and the work presented in the thesis are both my own, and have been generated by me as the result of my own original research. I confirm that:

- this work was done wholly or mainly while in candidature for a research degree at this University;
- where any part of this thesis has previously been submitted for a degree or any other qualification at this University or any other institution, this has been clearly stated;
- where I have consulted the published work of others, this is always clearly attributed;
- where I have quoted from the work of others, the source is always given. With the exception of such quotations, this thesis is entirely my own work;
- I have acknowledged all main sources of help;
- where the thesis is based on work done by myself jointly with others, I have made clear exactly what was done by others and what I have contributed myself;
- parts of this work has been published before submission

Signed:...

Date:..

Journal papers

[1] Tiantian Li and Milos Nedeljkovic and Nannicha Hattasan and Wei Cao and Zhibo Qu and Callum G. Littlejohns and Jordi Soler Penades and Lorenzo Mastronardi and Vinita Mittal and Daniel Benedikovic and David J. Thomson and Frederic Y. Gardes and Hequan Wu and Zhiping Zhou and Goran Z. Mashanovich. Ge-on-Si modulators operating at mid-infrared wavelengths up to 8μm. *OSA*, 8(7):828–836, 2019.

[2] Ahmed Osman, M. Nedeljkovic, J. Soler-Penades, Yangbo Wu, Zhibo Qu, A. Z. Khokhar, Kapil Debnath, and G. Z. Mashanovich. Suspended low-loss germanium waveguides for the longwave infrared. *Optics letters*, 43(24):5997–6000, 2018.

[3] G. Z. Mashanovich and M. Nedeljkovic and J. Soler-Penades and Z. Qu and W. Cao and A. Osman and Y. Wu and C. J. Stirling and Y. Qi and Y.X. Cheng and L. Reid and C. G. Littlejohns and J. Kang and Z. Zhao and M. Takenaka and T. Li and Z. Zhou and F. Y. Gardes and D. J. Thomson and G. T. Reed. Group iv mid-infrared photonics. *Optical Materials Express*, 8(8):2276–2286, 2018.

[4] Juan Gonzalo Wanguemert-Perez, Alejandro Sánchez-Postigo, Jordi Soler-Penades, Alejandro Ortega-Moñux, Milos Nedeljkovic, Robert Halir, Faysal El Mokhtari Mimun, YX Cheng, Z Qu, AZ Khokhar, and et al. Mid-infrared suspended waveguide platform and building blocks. *IET Optoelectronics*, 13, 2018.

[5] Benedetto Troia and Jordi Soler Penades and Zhibo Qu and Ali Z. Khokhar and Ahmed Osman and Yangbo Wu and Callum Stirling and Milos Nedeljkovic and Vittorio M. N. Passaro and Goran Z. Mashanovich. Silicon ring resonator-coupled Mach–Zehnder interferometers for the Fano resonance in the mid-IR. *Applied optics*, 56(31):8769–8776, 2017.

[6] G. Z. Mashanovich and C. J. Mitchell and J. S. Penades and A. Z. Khokhar and C. G. Littlejohns and W. Cao and Z. Qu and S. Stankovi and F. Y. Gardes and T. B. Masaud and H. M. H. Chong and V. Mittal and G. S. Murugan and J. S. Wilkinson and A. C. Peacock and M. Nedeljkovic. Germanium mid-infrared photonic devices. *Journal of Lightwave Technology*, 35(4):624–630, 2017.

[7] J. Soler Penades and A. Ortega-Moñux and M. Nedeljkovic and J. G. Wangüemert-Pérez and R. Halir and A. Z. Khokhar and C. Alonso-Ramos and Z. Qu and I.

Molina-Fernández and P. Cheben and G. Z. Mashanovich. Suspended silicon mid-infrared waveguide devices with subwavelength grating metamaterial cladding. *Optics express*, 24(20):22908–22916, 2016.

Conference papers

[1] A. Sánchez-Postigo, G. Wangüemert-Pérez, J. Soler Penades, A. Ortega-Moñux, M. Nedeljkovic, R. Halir, F. El Mokhtari Mimum, Z. Qu, A. Z. Khokhar, A. Osman, W. Cao, C. G. Littlejohns, G. Z. Mashanovich, P. Cheben, and I. Molina-Fernández. Suspended silicon integrated platform for the long-wavelength mid-infrared band. 121st International Conference on Transparent Optical Networks, ICTON 2019, Angers, France, 9-13 July 2019.

[2] G. Z. Mashanovich, J. Soler Penades, Y. Wu, V. Mittal, A. Osman. W. Cao, Z. Qu, Y. Qi, C. Stirling, M. Milosevic, L. Reid, D. J. Rowe, D. J. Thomson, M. Nedeljkovic. Mid-IR silicon and germanium photonic circuits for communications and sensing. IEEE Summer Topicals Meeting, Ft. Lauderdale, FL, USA, 8-10 July 2019.

[3] G. Z. Mashanovich, J. Soler Penades, A. Osman, A. Sánchez-Postigo, Z. Qu, Y. Wu, C. J. Stirling, D. P. Cheben, A. Ortega-Moñux, J. G. Wangüemert-Pérez, I. Molina-Fernández, and M. Nedeljkovic. Silicon and germanium-based mid-infrared platforms. PIERS 2019, Rome, Italy, 17-20 June 2019.

[4] G. Z. Mashanovich, W. Cao, Z. Qu, A. Osman, Y. Wu, D. Hagan, A. P. Knights, T. Li, Z. Zhou, J. Soler Penades, F. Y. Gardes, K. Li, D. J. Thomson, and M. Nedeljkovic. Silicon and germanium active devices for the mid-infrared. PIERS 2019, Rome, Italy, 17-20 June 2019.

[5] M. Nedeljkovic, Y. Qi, V. Mittal, D. J. Rowe, Z. Qu, Y. Wu, A. Osman, Z. Zheng, C. Wei, James S. Wilkinson, and G. Z. Mashanovich. Absorption spectroscopy in the mid-infrared using silicon and germanium waveguides. PIERS 2019, Rome, Italy, 17-20 June 2019.

[6] Y. Wu, Z. Qu, A. M. Osman, W. Cao, A. Z. Khokhar, J. Soler Penades, O. L. Muskens, G. Z. Mashanovich, and Milos Nedeljkovic. Mid-Infrared silicon waveguide-based bolometer. GFP 2019.

[7] M. M. Milosevic, W. Zhou, H. K. Tsang, A. Osman, S. Stankovic, Y. Qi, M. Nedeljkovic, Z. Qu, X. Yan1, A. Z. Khokhar, G. T. Reed, and G. Z. Mashanovich. Hyperuniform disordered polarisers for the mid-infrared. CLEO 2019, San Jose, CA, USA, 5-10 May 2019.

[8] J. Soler Penades, A. Osman, A. Sánchez-Postigo, Z. Qu, Y. Wu, C. J. Stirling, D. P. Cheben, A. Ortega-Moñux, J. G. Wangüemert-Pérez, M. Nedeljkovic, and G. Z. Mashanovich. Silicon and germanium mid-infrared platforms. SIOE 2019, Cardiff, Wales, 16-18 April 2019.

[9] A. Osman, M. Nedeljkovic, J. Soler Penades, Y. Wu, Z. Qu, A. Z. Khokhar, and G. Z. Mashanovich. Suspended low-loss germanium waveguides for the mid-infrared. Photonics West 2019, San Francisco, USA, 2-7 February 2019.

[10] Z. Qu,M. Nedeljkovic,Y. Wu,J. Soler Penades,A. Z. Khokhar,W. Cao,A. M. Osman,Y. Qi,N. K. Aspiotis,K. A. Morgan,C. C. Huang,G. Z. Mashanovich. Waveguide integrated graphene mid-infrared photodetector. 10537:105371N, Photonics West 2018, San Francisco, USA, 27 January 1 February 2018.

[11] Nedeljkovic Milos, Soler Penades Jordi, Osman Ahemd, Qi Yanli, Rowe Dave, Qu Zhibo, Wu Yangbo, Cao Wei, Mitta Vinita, Senthil Murugan Ganapathy, Khokhar Ali Z, Sánchez-Postigo Alejandro, Wang*ü*emert-Pérez Juan Gonzalo, Ortega-Moñux A, Halir Robert, Molina-Fernández Inigo, Cheben Pavel, S Wilkinson James, and Z Mashanovichs Goran. Group-iv material waveguide devices for mid-infrared absorption spectroscopy. EOSAM 2018, Delft, Netherlands, 8-12 October 2018..

[12] Cao Wei, Nedeljkovic Milos, Hagan David, G Littlejohns Callum, Qu Zhibo, Z Khokhar Ali, Y Gardes Frederic, P Knights Andy, J Thomson Dave, and Mashanovich Goran, Z. Mid-infrared modulation in silicon. MIOMD 2018, Flagstaff, Arizona, USA, 7-11 October 2018.

[13] J Rowe Dave, Qi Yanli, Mittal Vinita, Osman Ahmed, Qu Zhibo, Wu Yangbo, Banakar Mehdi, Soler Penades Jordi, Sánchez-Postigo Alejanro, Wang*ü*emert-Pérez Juan Gonzalo, Ortega-Moñux Alejanro, Halir Robert, Molina-Fernández Iinigo, S Wilkinson James, Nedeljkovic Milos, and Z Mashanovich Goran. Silicon photonics for mid-infrared sensing. The Ninth International Conference on Sensor Device Technologies and Applications, SENSORDEVICES 2018, The Ninth International Conference on Sensor Device Technologies and Applications, Venice, Italy, 16-20 September 2018.

[14] Z Mashanovich G, Soler Penades J, Cao W, Qu Z, Osmah A, Wu Y, Z Khokhar A, J Littlejohns C, Stankovic S, Reynolds S, Mittal V, S Murugan G, S Wilkinson J, Qi Y, Y Gardes F, J Thomson D, and Nedeljkovic M. Group iv mid-infrared devices and circuits. Photonics West 2018, San Francisco, CA, USA, 27 January 1 February 2018.

[15] Tiantian Li, Milos Nedeljkovic, Nannicha Hattasan, Ali Z Khokhar, Scott A Reynolds, Stevan Stanković, Mehdi Banakar, Wei Cao, Zhibo Qu, Callum G Littlejohns, et al. Mid-infrared ge-on-si electro-absorption modulator. In *Group IV*

Photonics (GFP), 2017 IEEE 14th International Conference on, pages 7–8. IEEE, 2017.

[16] Nedeljkovic Milos, Li Tiantian, G Littlejohns Callum, Hattasan Ninncha, Z Khokhar Ali, A Reynolds Scott, Stanković Steven, Banakar Mehdi, Wei. Cao, Qu Zhibo, Soler Penades Jordi, Grabska Kasia, Mastronardi Lorenzo, Crudgington Lee, Chen Xia, Nazir Ahmed Arifa, Saïd Rouifed M, Qiu H, Guo Xin T, Wang H, Wu H, Zhou Z, T Reed Graham, J Thomson Dave, Y Gardes Frederic, and Z. Mashanovich Goran. Silicon-on-insulator and germanium-on-silicon free carrier modulators for mid-infrared wavelengths. Conference on Lasers and Electro-Optics Pacific Rim, 2017.

[17] Nedeljkovic M, G Littlejohns C, Li T, N Hattasan, Z Khokhar A, A Reynolds S, Stanković S, Banakar M, Cao W, Qu Z, Soler Penades J, Grabska K, Mastronardi L, Crudgington L, Chen X, N Ahmed A, S Rouifed M, Qiu H, G Xin T, Wang H, Wu H, Zhou Z, T Reed G, J Thomson D, Y Gardes F, and Z Mashanovich G. Silicon and germanium free carrier injection modulators for the mid-infrared. SPIE 2017 Optics and Optoelectronics Symposium, Prague, Czech Republic, 24 -27 April 2017.

[18] Z Mashanovich G, Cao W, Qu Z, Osman A, Wu Y, Li T, Soler Pénades J, Stankovic S, Slavik R, Y Gardes F, Mittal V, S Murugan G, S Wilkinson J, J Thomson D, G Littlejohns C, and Nedeljkovic M. Mid-infrared integrated photonics in silicon and germanium. ECIO 2017, Eindhoven, Holland, 3-5 April 2017.

[19] Nedeljkovic M, Ortega-Moñux A, Soler Penadés J, Wangüemert-Pérez G, Z Khokar A, Halir R, Mittal V, Qu Z, Cao W, Mitchell C, Stankovic S, Gardes F, Alonso-Ramos C, Cheben P, Molina-Fernandez I, Murugan G, S, Wilkinson J, and Z Mashanovich G. Group-iv material waveguides for mid-infrared sensing. EOSAM 2016, Workshop on Sensing Applications Enabled by Silicon Photonics Berlin, Germany, 26-30 September 2016.

[20] M. Nedeljkovic, A. Ortega-Moñux, J. Soler Penadés, G. Wangüemert-Pérez, A. Z. Khokhar, R. Halir, Z. Qu, W. Cao, C. Mitchell, S. Stanković, F.Gardes, C. Alonso-Ramos, P. Cheben, and I. Molina-Fernández. Sub-wavelength cladded suspended silicon photonic components for the mid-infrared: fabrication and experiment. META16, 7th International Conference on Metamaterials, Photonic Crystals and Plasmonics, Malaga, Spain, 25-28 July 2016.

[21] Nedeljkovic Milos, Soler Penadés Jordi, Z. Khokhar Ali, Qu Zhibo, Cao Wei, Mitchell Colin, Stanković Stevan, Gardes Frederic, Alonso-Ramos Carlos, Ortega-Moñux Alejandro, Wangüemert-Pérez Gonzalo, Halir Robert, Molina-Fernández Iñigo, and Cheben Pavel. Design of integrated mid-IR photonic devices. Photonics North 2016,Quebec City, Quebec, Canada, 24-26 May 2016.

[22] M. Nedeljkovic, J. Soler Penadé, A. Z. Khokhar, Z. Qu, W. Cao, S. Stanković, C. J. Mitchell, S. A. Reynolds, C. Littlejohns, F. Gardes, A. V. Velasco, P. Cheben, R. Soref, and D. Thomson. Mid-infrared modulation mechanisms in germanium. Energy Material Nanotechnology Quantum Meeting, Phuket, Thailand, 8-11 April 2016.

List of Acronyms

2-D Two-dimensional

AMMI Angled Multimode interferometer

AWG Arrayed Waveguide Grating

APDs Si Avalanche Photodiodes

BP Black Phosohorus

BOX Buried Oxide

CMOS Complementary Metal-Oxide Semiconductor

CVD Chemical Vapor Deposition

CW Continuous Wave

CZ Czochralski

CMP Chemial Mechanical Polishing

DI Deionised water

EHP Electron Hole Pair

EQE External Quantum Efficiency

FIB Focused Ion Beam

FIR far-infrared

FWHM Full Width at Half Maximum

FZ Float Zone

FLG Few Layers Graphene

FMM Film Mode Matching

FDTD Finite-Difference-Time-Domain

FNA Fuming Nitric Acid

GOS Germanium in Silicon

GPIB General Purpose Interface Bus

GaAs Gallium Arsenide

GaSb Gallium Antimony

Ge Germanium

HF Hydrofluoric acid

h-BN Hexagonal Boron Nitride

ICP Inductively Coupled Plasma

IPA Isopropyl Alcohol

IQE Internal Quantum Efficiency

LOCOS Local Oxidation of Silicon

LPCVD Low-Pressure Chemical Vapor Deposition

LPE Liquid-Phase Exfoliation

MIR Mid-Infrared

MOSFET Metal-Oxide-Semiconductor Field-Effect

MZI Mach-Zehnder Interferometer

MoS$_2$ Molybdenum Disuflide

NIR Near-Infrared

NEP Noise Equivalent Power

PECVD Plasma-Enhanced Chemical Vapor Deposition

PMMA Poly Methyl Methacrylate

PDs Photodetectors

PET Polyethylene Terephthalate

QCL Quantum Cascade Laser

RF Radio Frequency

RIE Reactive Ion Etcher

RP-CVD Reduced Pressure Chemical Vapor Deposition

SOI Silicon on Insulator

SIN Silicon on Nitride

SOS Silicon on Sapphire

SON Silicon on Nitride

SEM Scanning Electron Microscope

SWG Sub-wavelength Grating

SiC Silicon Carbide

SR Spectral Response

SLG Single Layer Graphene

THz Terahertz

TMD Transition Metal Dichalcogenides

TE Transverse Electrical

TM Transverse Magnetic

UV Ultraviolet

vdW van der Waals

WS$_2$ Tungsten Diselenide

Chapter 1

Introduction

Silicon photonics investigates optoelectronic devices made from silicon (Si) and silicon compatible materials. It has been shown that silicon photonics has the capability of operating in the mid-infrared (MIR) (2-20 μm), although integrated silicon photonics devices for near-infrared (NIR) (780-2000 nm) data telecommunication applications (especially in 1.55 μm wavelength) are still drawing great attention. New techniques are required to extend silicon photonics from NIR to MIR wavelengths. If successful, applications such as spectroscopy, chemical and biological sensing, and free space communications can benefit from on-chip optoelectronic systems [1].

This project focuses on waveguide integrated photodetectors based on group IV materials. Silicon has the inherent disadvantage of being an indirect bandgap semiconductor with a centrosymmetric crystal structure, and it lacks many essential properties to be used for active optoelectronics devices such as lasing and electro-optic modulator. Thus, introducing new materials to silicon may be the best option for achieving complex photonic integrated circuits. Graphene can interact with light from the ultraviolet (UV) to terahertz (THz) range, which makes it a promising material for realising optical detection in the mid-infrared range when coupled with group IV platforms. This report presents the investigation of waveguide integrated graphene mid-infrared photodetectors for the 3.8 μm wavelength.

1.1 Near-infrared silicon photonics

The driver for the development of high data-rate and bandwidth in communication links originates from the increasing demand for high-speed internet services, and has boosted the investigation of silicon photonics. Long distance telecommunications have hugely benefited from the developed technology of low loss optical fibres but communication at shorter distances (such as inter-chip and intra-chip) is still under research [2]. The ever-improving clock speeds and high level of integration required means that using electrical signals and copper wires becomes a bottleneck for ever shorter distance data-links. Large scale data centres are limited by the demands of increasing bandwidth and energy consumption from copper interconnects. Thus the emergence of silicon photonics is promising for overcoming these limitations being a high volume low-cost data link choice.

Silicon photonics investigates devices that are mainly made from silicon and germanium, and it is also known as group IV photonics. Silicon photonics benefits from the previous development of fabrication processes by the microelectronics industry, which enables low-cost high-volume fabrication. Moreover, it is possible to integrate the optoelectronics components and complementary metal-oxide-semiconductor (CMOS) electronic devices on the same chip, which can be used to build a large bandwidth backbone system for optical interconnects required in multi-core CPUs [3]. Since the same materials and fabrication procedures can be applied as for current microelectronics fabrication, silicon photonics has become popular in both industry and academia and holds the promise of low cost and the potential to integrate both CMOS electronic and photonic components on the same chip. The principal research interests in silicon photonics have been targeted in the communication field and especially for data-centres, with the development of passive devices such as waveguides, wavelength division multiplexers [4–6], splitters [7, 8], and actives devices for example modulators [9–12] and detectors [13–15]. A number of commercial products have resulted from the development of silicon photonics in the near-infrared, such as the 100G optical transceiver by Intel [16], and embedded optical modules by Luxtera [17]. IBM [18] and Rockley Photonics [19] are also investigating silicon photonics.

Even though the majority of the interest is focused on communications, silicon photonics can play a strong role in sensing. The sensing area has a wide range of applications from measuring physical quantities, such as temperature [20], pressure [21], humidity [22], and strain [23], to bio-medical sensing [24–27]. For instance, the biomarker and protein digestion kits provided by Genalyte Maverick system [28] contain a silicon photonics ring resonator integrated with microfluidics that acts as a biosensor. When a sample flows through the chip, an analyte of interest that is present in the sample interacts with the biologically functionalised surface, resulting in a change of the refractive index. By monitoring the refractive index changes in the analyte can be detected in real time.

1.2 Mid-infrared photonics

The mid-infrared is commonly defined as the wavelength range from 2 μm to 20 μm. In the early stages of silicon photonics research, there were not many researchers across the world investigating the group-IV materials in the mid-infrared range. With the development of silicon photonics in the near-infrared, more and more attention has been paid to longer wavelengths. MIR silicon photonics can benefit from the well-developed processes and devices in the telecom wavelength range as many of the processing techniques and design methods can be implemented at longer wavelengths. It is also worth pointing out that, since MIR waveguides are inherently larger than those in the NIR, fabrication tolerances are more flexible in the MIR.

There are many potential applications for silicon photonics in the MIR. One of the most important fields is chemical and biological sensing, such technology could be used to fabricate "lab-on-a-chip" integrated sensors, as many organic molecules and gases have their vibrational states within the so-called fingerprint region (8-12 μm) [29]. Therefore, military and aerospace technologies can benefit from MIR photonic integrated circuits operating within the atmospheric transparency wavelength window from 8-13 μm, to develop products for missile detection and tracings, dangerous species detection [1], remote sensing, and free-space communication. In terms of medical and biological applications, there is interest in building small, cheap, portable and mass producible detectors, one example is a cocaine sensor in human saliva at 5.3 μm wavelength that was made from Ge-on-Si waveguides [30]. Another example is an environmental sensing system made up from mid-infrared sensors, that has been applied in real time monitoring of hazardous subsea pollutants for the purpose of protecting global water resources [31]. The attraction of building low cost, mass producible and portable sensors based on group-IV photonics in MIR will attract an increasing number of researchers and industrial companies in the near future. The trend is heading towards chip-scale integration, which could provide better performance, smaller sizes, lower power consumption, and higher reliability than existing optoelectronics systems, thus several building blocks are required to realise the lab-on-a-chip functionality [32].

- Integrated sources and detectors:

  Integration of light sources and detectors is crucial to achieving a lab-on-a-chip system, and it could greatly reduce the losses from coupling light in and out of the chip. To build a truly portable remote sensor, integrable sources and detectors are necessary since the commercial external sources and detectors available are not only bulky but also very expensive.

- Waveguides:

  Low loss waveguides are essential for routing light and for building other devices such as Mach-Zehnder interferometers (MZI) and ring resonators. In terms of sensing application, it is necessary that waveguides can operate over a wide wavelength range so that a variety of compounds can be sensed. This thesis presents a review for different platforms that can be used in the MIR.

- Splitter, couplers, and multiplexers:

  These structures are based on waveguides with optimised dimensions that can split, guide and combine light, such as directional couplers, y-splitters and multimode interferometers (MMI). As for multiplexers, several devices such as angled multimode interferometers (AMMI), arrayed waveguide gratings (AGW) and MZI or rings can also be applied for this purpose.

- Structure for enhancing optical interaction with analytes:

  In general, most of the optical mode is confined in a defined optical waveguide while propagating. For the purpose of increasing the light-matter interaction, resonant structures can be used such as resonators, Vernier devices or photonic crystal waveguides to slow the propagation of light.

- Modulators:

  For lab-on-a-chip sensors, integration of modulators can be ideal for on-chip signal processing purpose, using them as lock-in amplifiers to improve the signal-to-noise ratio. High-frequency modulation is not necessary for sensing applications. On the other hand, for free-space communication and data communication, modulation speed is very important.

The use of silicon-on-insulator (SOI) is a logical first step in MIR research because many of fabrication and characterisation procedures used in NIR can be implemented in the MIR.

1.3 Two-dimensional materials and graphene

Two dimensional (2-D) layered materials are defined as materials artificially derived from van der Waals solid formed layers where atoms are held together by ionic bonds along the 2-D surface plane (in-plane) directions, while atomic layers are bonded together along the perpendicular direction (out-of-plane) by the van der Waals force [33–36]. What makes it possible to cleave these layered through mechanical [37, 38] or liquid phase exfoliation [39, 40] into few-atom thick or even monolayer thick sheets is the weak van der Waals force. The most well known 2-D material is graphene, which was discovered in 2004 [41], and is made from a single layer of carbon atoms bonded together in a hexagonal lattice. Graphene has many appealing electronic, optical and mechanical properties [42–44]. For example, it has a gapless band-structure and is a semimetal material, which allows graphene to interact with light from ultraviolet to terahertz wavelengths [45, 46]. This makes graphene a promising material to be used in photodetectors over a very broad wavelength range. Even though graphene has a high absorption coefficient [47], only 2.3% of the incident light from the out-of-plane direction can be absorbed, which restricts the performance of photodetectors. Consequently, many approaches have been investigated for increasing the graphene-light absorption. Aside from graphene, there are many other 2-D materials such as MoS_2, black phosphorus (BP) and hBN that have few to monolayer thickness that exhibit distinct electric, optical, thermal and mechanical properties compared to their 3D (bulk) formations [48, 49]. Depending on the composition of materials these 2-D layered materials can be metals, insulators or semiconductors [50, 51].

The electric [52] and optoelectronic [53, 54] properties of 2-D layered semiconductors are dependent on the number of layers due to quantum confinement effects in the direction perpendicular to the 2-D plane [55]. For example, transition metal dichalcogenides (TMDs) [56] and black phosphorus [57] exhibit direct layer-dependent physical properties. Some 2-D layered materials have high transparency [58] and superb mechanical flexibility [59], such as graphene, that can be used for detection, in novel wearable, bendable and portable devices. Since the van der Waals interaction between neighbouring layers does not contain any dangling bonds at the surface, the 2-D layered materials break the lattice matching boundary and can be grown on various substrates [60]. Many heterostructures can be designed with various functions based on stacks of different 2-D materials. Moreover, 2-D layered materials provide a chance to tailor the carrier densities and polarity through electrostatic [61] or chemical doping [62]. This wide range of tunable material properties together with the possibility of designing multi-functional 2-D layered materials structures, provides a chance to develop high-performance optoelectronic devices, especially photodetectors that cover a wide spectral range.

Photodetectors convert absorbed light signal into an electrical signal and are now used throughout modern society. For example, they are used in biomedical imaging, optical communication, military, security checks, night vision, environmental monitoring, scientific research, and industrial processing control. Currently, the high-performance photodetector market is dominated by the crystal bulk silicon and germanium in the visible to NIR wavelengths, while in the mid-infrared region materials such as InGaAs and related III-V materials are primarily used because the operating wavelengths are beyond the detection limit of silicon-based devices. These materials are very expensive to grow and they must be cooled when operating. The appearance of 2-D layered materials with many appealing properties such as strong light-matter interaction and ease of fabrication fill the gap of current silicon-based technologies and offers great promise towards the achievement of novel 2-D material integrated photodetectors.

The device reproducibility and manufacturability of 2-D material devices remains a challenge, but 2-D material technology can widely be found in research labs worldwide, with work focusing not only on graphene, but also on other 2-D materials, such as, phosphorene and stanene or transition metal dichalcogenides.

1.4 Thesis outline

The aim of the project described in this thesis is to present and demonstrate a waveguide integrated graphene mid-infrared photodetector that could in the foreseeable future be part of integrated sensor devices. Most of the effort has been geared towards waveguide integrated mid-infrared photodetectors that could replace the currently available bulk mid-infrared photodetectors. In this thesis:

- Chapter 2 reviews the state-of-the-art for different mid-infrared waveguide platforms. This is followed by a review of 2-D materials, especially graphene in terms of their electronic and optoelectronic properties. Then, a review of the state-of-the-art graphene photodetectors is presented.
- Chapter 3 presents the simulation tools, fabrication processes, and experimental setup used to develop mid-infrared waveguides with which the detectors are to be integrated, and shows the results of their experimental characterisation.
- Chapter 4 investigates the experimental process for integrating graphene with silicon waveguides. Devices were made in three generations: the first included preliminary testing of graphene that was transferred by Nikolas Aspiotis in the University of Southampton, while the patterning and characterisation were carried out by myself. The second and third generations were collaborations with a commercial company, Applied Nanolayers, and Dr Junjia Wang from the University of Cambridge respectively, where the two collaborators carried out the graphene

transfer and patterning processes based on my design and all of the measurement was carried out by me personally.

- Chapter 5 details the experimental characterisation of the fabricated graphene mid-infrared photodetectors, and discusses the results. The electrodes were fabricated by Applied Nanolayers and Dr Junjia Wang based on my design. The electrical measurement was carried out at the University of Southampton.
- The conclusions for this project and possible future work are described in Chapter 6.

Chapter 2

Literature review

2.1 Introduction

This chapter includes a brief illustration of the theory and background of silicon photonic waveguides in the mid-infrared. A short description of 2D materials especially of graphene and its properties as well as photodetection mechanisms and fabrication methods are included, followed by a review of the state-of-the-art of graphene integrated photodetectors.

2.2 Waveguides

At the beginning of this section, the theory of fundamental principles of waveguiding will be discussed, followed by a review of different types of waveguides and platforms which can be used in the mid-infrared.

2.2.1 Planar photonic waveguides

The geometry of a planar photonic waveguide includes a high refractive index dielectric layer in the middle known as the core and it is covered by two materials with different refractive indices at the top (n_c) and bottom (n_s) (Figure 2.1). Light propagating along the waveguide is a transverse electromagnetic field; the direction of electric field and the magnetic field are perpendicular to the propagating direction (z).

According to the Maxwell's equations, when light propagates along a uniform refractive index medium, the following wave equations describe the transverse electrical and transverse magnetic fields respectively [32]:

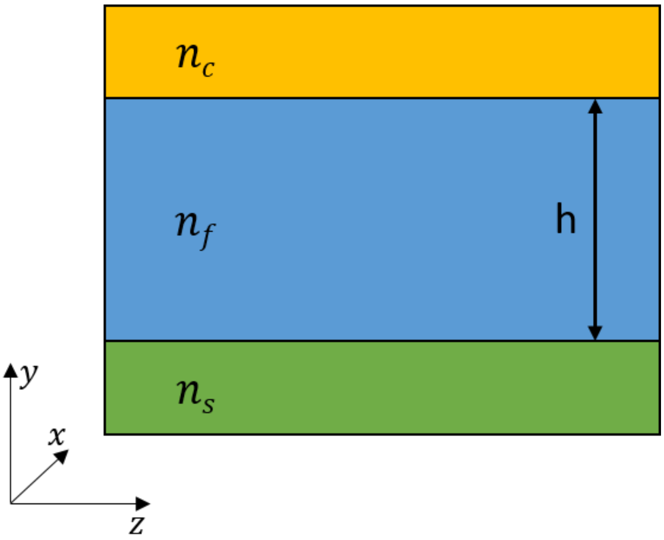

Figure 2.1: Planar waveguide diagram. n_s is the refractive index of the substrate, n_f is the refractive index of the core and n_c is the refractive of the upper cladding.

$$\frac{d^2H_x(y)}{dy^2} + [k_0^2n^2 - \beta^2]H_x(y) = 0 \tag{2.1}$$

$$\frac{d^2E_x(y)}{dy^2} + [k_0^2n^2 - \beta^2]E_x(y) = 0 \tag{2.2}$$

From the above equations, $E_x(y)$ is the x-axis polarised electric field along the y-axis direction and $H_x(y)$ is equivalent for magnetic field, n is the refractive index of the medium, β is the propagation constant and $k_0^2 = (\frac{2\pi}{\lambda_0})^2 = \mu_0\varepsilon_0\omega^2$ is the square of the wavenumber, where ω is the angular frequency, ε_0, μ_0, and λ_0 are the free-space permittivity, permeability, and operating wavelength respectively.

In order to solve the above equations, additional conditions are needed, which are obtained by introducing the boundary conditions at the interfaces, taking into account the $\beta = k_0n_{eff}$, where n_{eff} is the effective index of the mode. The solution of these equations has been well demonstrated elsewhere, which can be found in many publications, such as in [32], thus it will not be shown here.

The solution of the above equations includes a sinusoidal electric (and magnetic) field along the central dielectric region and exponentially decaying fields (evanescent fields) in the cladding. The field inside the waveguide core can be considered as a transverse standing wave, in order to fulfil the boundary conditions, therefore only discrete field distributions are allowed, which are referred as the guided modes. Depending on the number of the modes one waveguide supports, it can be classified as single mode (if only one mode is permitted) or multimode (if more than one mode satisfies the boundary conditions). The number of modes that one waveguide can support is dependent on both the waveguide geometry and the refractive indexes of the core and claddings. In general, larger waveguides can support more modes, however, single mode waveguides are more preferable.

For a rib or strip waveguide that can confine light in the two dimensions, the solution is more complicated. Solving analytical equations for these complex waveguides is unrealistic, therefore numerical methods are introduced and will be discussed in chapter 3. For transverse electrical (TE) polarisation, for single mode operation, a strip width must be smaller than the width for which the first order mode starts to propagate. Similarly, for the transverse magnetic (TM) polarisation, the height of the waveguide has to be limited. There are some parameters that can be adjusted in order to optimise the waveguide performances. In general, such limitation for operation at the waveguide dimension is designed for a specific wavelength. Nevertheless, waveguide dimensions increase for operation at longer wavelengths due to the expand size of the optical modes.

The single mode conditions for large rib waveguides are described below [63]:

$$r = \frac{h}{H} < 0.5 \quad t = \frac{\omega}{H} \tag{2.3}$$

$$t < 0.3 + \frac{r}{\sqrt{1 - r^2}} \tag{2.4}$$

where r is the ratio between thickness of the rib (H) and slab height (h), and t is the ratio between the width of the waveguide (ω) and the height of the waveguide (H) (shown in Figure 2.2). This allows micron-scale level waveguides to have the ability to work at even shorter wavelengths, and a wider waveguide should have lower scattering loss when the mode propagates along the waveguide. However, a thicker waveguide heright might be more difficult to fabricate, thus a shallow etch is introduced during fabrication, which

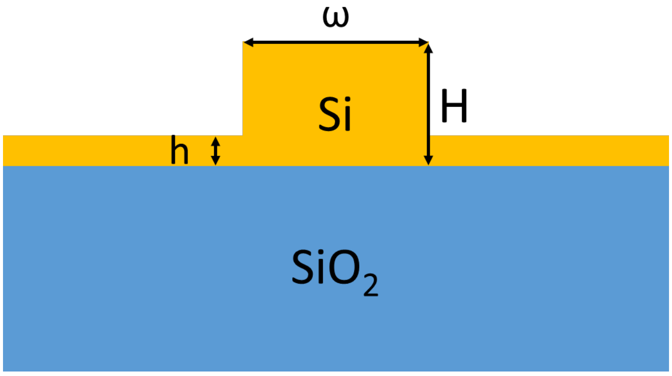

Figure 2.2: Diagram of a silicon-on-insulator rib waveguide.

on the other hand might increase the footprint of the device as the lateral leakage from the cladding restricts the minimum bend radius of the waveguide.

2.3 Non group-IV integrated optics

Before presenting the state-of-the-art of mid-infrared group-IV material photonic components, it is necessary to review novel non-group-IV integrated photonic components for the MIR briefly.

MIR systems generally adopts unconventional materials with less developed protocols, attributing to much higher fabrication costs than their NIR equivalents. For example, mid-infrared optical components are often made from chalcogenides or halide crystals which are not standard optical materials such as polymers or oxide glasses, because they both are opaque in the MIR.

From literature, infrared-transparent chalcogenides and halides can be monolithically deposited on Si or dielectric substrates through thermal evaporation or sputtering methods, and waveguides can be defined by using two compositions with different refractive indices for the core and cladding. Several non-group-IV platforms have been demonstrated in the MIR. Recently, ZnSe rib waveguides with low loss of 0.6 dB/cm between 2.5-3.7 μm have been reported [64]. A Gallium Antimony (GaSb) waveguide is demonstrated with losses of 0.7 dB.cm and 1.1 dB/cm at 2 μm and 4 μm wavelengths, respectively [65]. Moreover, chalcogenide materials provide a potential solution at longer wavelengths and a waveguide made from two different refractive index chalcogenides showed 2.5 dB/cm propagation loss at a wavelength of 7.7 μm [66].

However, chalcogenide materials are fragile and none of these chalcogenides and halides platforms can provide refractive index contrast as high as Si or Ge platforms. Moreover, chalcogenides and halides are not compatible to CMOS foundry processes whilst Si and Ge have the possibility for CMOS integration which make group-IV materials more favourable. III-V materials are more expensive than group-IV materials and have large footprint.

2.4 Silicon photonics waveguides in the mid-infrared

Silicon-on-insulator (SOI) is the most commonly used waveguide platform in the NIR silicon photonics. The SOI platform is made from a silicon layer at the top, followed by a thick silicon dioxide layer which is also called the ”buried oxide” (BOX), then followed by a silicon substrate at the bottom. The waveguide is formed by etching down the top silicon layer. The performance of a waveguide is highly affected by the difference of refractive indices between the waveguide core and claddings. For SOI, the waveguide core is Si, which has a refractive index n = 3.48 at $\lambda = 1.55$ μm, and top cladding air n = 1, and the bottom cladding is silicon dioxide $n = 1.45$ at $\lambda = 1.55$ μm. These differences directly determine the optical confinement of the mode inside the waveguide core and thereby determine the dimensions of the waveguide and the minimum bend radius that the waveguide can support.

There are many sources that contribute to the waveguide loss, the main factors being the material absorption loss from the waveguide, scattering loss from the surface roughness and radiation loss from the confined mode in the waveguide, Material absorption loss is intrinsic and unavoidable for a chosen waveguide platform, while scattering loss mainly comes from the sidewall roughness, which can be reduced by modifying the fabrication process and recipes. The smallest propagation loss of SOI rib waveguides that has been achieved was 0.272 ± 0.0012 dB/cm at 1.55 μm wavelength [67].

When it comes to the mid-infrared wavelength region, SiO_2 has absorption loss more than 10 dB/cm in the wavelength ranging from 2.6 - 2.9 μm, and above 4 μm, and Si has the same behaviour when the wavelength is over 8 μm. So the design of the silicon photonics platform in the mid-infrared range should consider different material combinations. Here, a brief illustration of different platforms that can be used in the mid-infrared wavelength range is given and Figure 2.3 shows the predicted transparency windows in the mid-infrared for each platform.

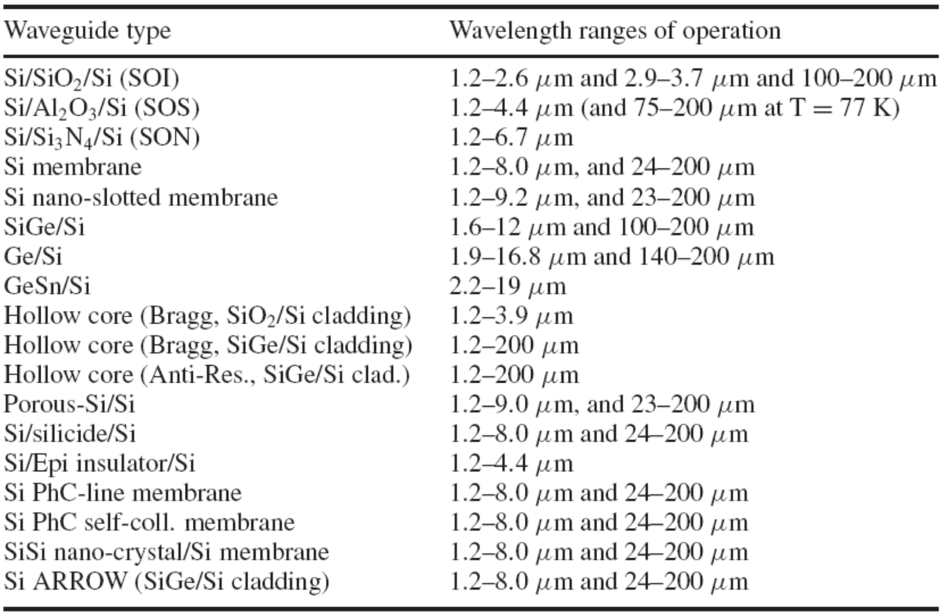

Waveguide type	Wavelength ranges of operation
$Si/SiO_2/Si$ (SOI)	1.2–2.6 μm and 2.9–3.7 μm and 100–200 μm
$Si/Al_2O_3/Si$ (SOS)	1.2–4.4 μm (and 75–200 μm at T = 77 K)
$Si/Si_3N_4/Si$ (SON)	1.2–6.7 μm
Si membrane	1.2–8.0 μm, and 24–200 μm
Si nano-slotted membrane	1.2–9.2 μm, and 23–200 μm
SiGe/Si	1.6–12 μm and 100–200 μm
Ge/Si	1.9–16.8 μm and 140–200 μm
GeSn/Si	2.2–19 μm
Hollow core (Bragg, SiO_2/Si cladding)	1.2–3.9 μm
Hollow core (Bragg, SiGe/Si cladding)	1.2–200 μm
Hollow core (Anti-Res., SiGe/Si clad.)	1.2–200 μm
Porous-Si/Si	1.2–9.0 μm, and 23–200 μm
Si/silicide/Si	1.2–8.0 μm and 24–200 μm
Si/Epi insulator/Si	1.2–4.4 μm
Si PhC-line membrane	1.2–8.0 μm and 24–200 μm
Si PhC self-coll. membrane	1.2–8.0 μm and 24–200 μm
SiSi nano-crystal/Si membrane	1.2–8.0 μm and 24–200 μm
Si ARROW (SiGe/Si cladding)	1.2–8.0 μm and 24–200 μm

Figure 2.3: Estimated wavelength range for different platforms that have less than 2 dB/cm propagation loss at 300 K, reproduced from [68].

2.4.1 Silicon on insulator

The SOI platform was first demonstrated in the MIR at 3.39 μm, when large rib waveguides (height x width: 2 μm × 2 μm) with 2 μm thick BOX layer were demonstrated with low propagation losses of 0.6 - 0.7 dB/cm after using thermal oxidation to smooth the roughness of the sidewalls [69].

A 4.6 dB/cm propagation loss at 3.74 μm wavelength from a strip waveguide with dimensions of 1400 nm width and 500 nm height has been presented [70]. It is the first demonstration that showed SOI waveguides can be used at wavelengths greater then 3.7 μm and even probably beyond, where SiO_2 has high absorption. A low loss waveguide made from 500 nm SOI was published with only 1.3 dB/cm loss at 3.8 μm wavelength [68], which proved that SOI can be used up to 3.8 - 3.9 μm.

2.4.2 Germanium on silicon

A germanium on silicon (Ge-on-Si) waveguide was first published in 2012 [71]. For the purpose of growing Ge on silicon, 10 μm thickness of intrinsic Si is deposited on the silicon wafer as a buffer layer, followed by a 2 μm thickness Ge layer deposited by reduced pressure chemical vapour deposition (RP-CVD) [72]. A 3.6 dB/cm propagation loss at the 5.8 μm wavelength has been achieved. After that, the modified design of 2.0-2.6 μm thick [73] and 2 μm thick [74] with reported minimum losses of 2.3-5.4 dB/cm to 2.3-3.5 dB/cm for TE polarisation and 3-4 dB/cm losses for TM polarisation were reported in the literature.

A rib waveguide has been demonstrated with 2.9 μm height and 2.7 μm width with 1.7 μm etch depth made from a 3 μm thick Ge-on-Si platform with 0.6 dB/cm loss at 3.8 μm wavelength for TE polarisation, Figure 2.4 shows the SEM image of the cross-section of the waveguide [75]. A recent demonstration of a Ge-on-Si waveguide of 2.5 dB/cm propagation loss has been reported at 7.575 μm wavelength but with larger losses at 8.8 μm ($\sim$ 15 dB/cm) [76].

Due to the transparency range of Ge, Ge-on-Si waveguides are expected to have the widest operation range of the platforms considered here. In terms of the longer wavelengths (λ = 8 - 16 μm), silicon is not considered as an ideal substrate material due to the high absorption of silicon in this range, which may restrict the transparency window of Ge-on-Si platform, moreover, due to the small refractive contrast between Ge (n = 4) and Si, the integration density when embedded in photonic circuits may be limited. Another problem is threading dislocations that appear at the Ge-Si interface as a result of different lattice constants between Ge and Si.

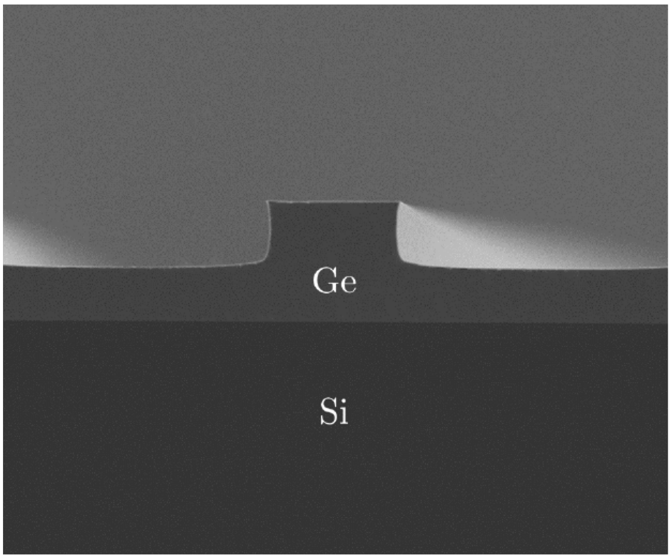

Figure 2.4: SEM image cross-section of a Ge-on-Si waveguide, from [75].

2.4.3 Silicon on silicon nitride

Silicon on silicon nitride (SON) is a promising substrate as it is transparent across visible, NIR and MIR up to 7 μm wavelength. Research on SON waveguides has demonstrated propagation losses of 5.2 dB/cm for TE and 5.1 dB/cm for TM waveguides with 2 μm height, 2 μm width and 0.8 μm etch depth dimension [77]. The substrate was fabricated by bonding an oxidised Si die with a SOI die coated with Plasma-Enhanced Chemical Vapor Deposition (PECVD) low-stress silicon nitride, then the back Si was removed by lapping and wet-etching in TMAH and the SiO_2 layer was etched by HF (Figure 2.5). The loss of such waveguides is highly dependent on the ration of the thickness of the Si layer and the operating wavelength, and scattering from sidewall roughness. Since it was a bonding process which was carried out under atmospheric pressure, bubble formation has been found in the fabricated SON sample, which could contribute to further losses. Silicon on nitride is one potential material as it is transparent in the visible and up to 7 μm wavelength, however, the smaller refractive index compared to Si or Ge , which is around 2, leads to smaller refractive index contrast with the substrate material, having potential leakage problems if the SiN layer is not sufficiently thick.

SON has also been demonstrated with 2.1 dB/cm propagation loss at 3.7 μm wavelength [78], by using Low-Pressure Chemical Vapor Deposition (LPCVD) to produce the SON films. Depending on the Si and N ratio during deposition, the SON refractive index can change from 1.57 to 2.7. Due to this property, the SON platform can be used in different applications: lower refractive index substrates can be used as a cladding and higher refractive index material can be used as the core of the waveguide. SON waveguides integrated with III-V lasers have been demonstrated and showed the potential of operating up to 8.5 μm [79]. Another advantage of the SON platform is that it can be deposited by a wide range of tools such as PECVD, hot-wire Chemical Vapor Deposition

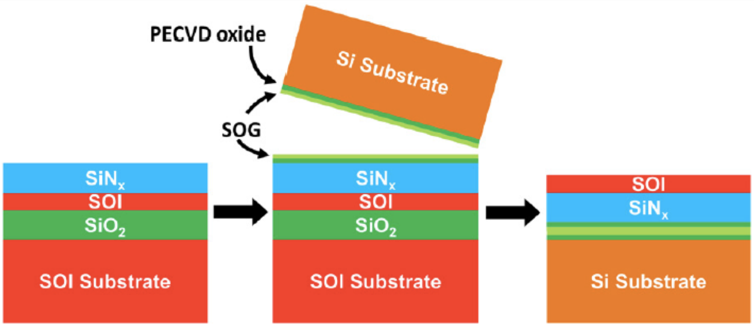

Figure 2.5: Fabrication processes diagram of SON, from [77].

(HWCVD), or using LPCVD [78]. However, the deposition condition needs to be controlled carefully, because it severely influences the optical performance of the material, making it necessary to build special deposition recipes that can be complex and time consuming.

2.4.4 Silicon on sapphire

Silicon on sapphire (SOS) offers high confinement from the telecom-wavelengths up to 5.5 μm [80]. One epitaxially grown 1.9 μm wide, 0.6 μm height strip SOS waveguide has been demonstrated by using e-beam lithography and RIE etching [81]. It has been reported that the propagation loss was reduced from 9.6 dB/cm down to 4.7 dB/cm at 4.5 μm wavelength after removing the resist residues. There is another demonstration of SOS waveguide with 1.8 μm width and 0.6 μm thickness having been reported with a loss 4.0±0.7 dB/cm at 5.5 μm wavelength [82] (Figure 2.6).

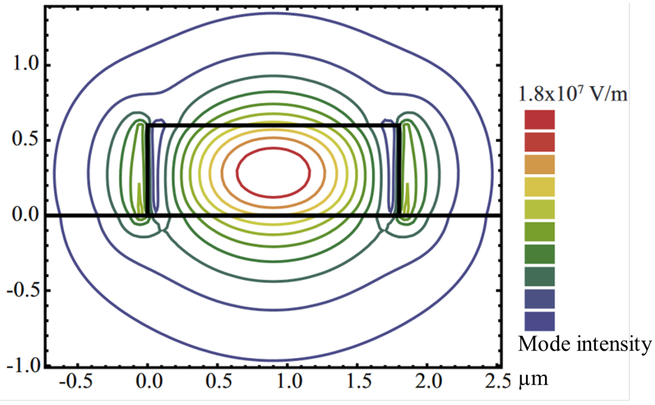

Figure 2.6: SOS contour diagram of the optical mode within the waveguide, from [82].

Both waveguides had similar waveguide dimensions and operating wavelengths, however, the propagation losses were not that low compared with other platforms which might be due to localised defects in the silicon. Another SOS waveguide has been published with 2 dB/cm loss at 5.18 μm wavelength [83].

It is necessary to point out that the hardness of sapphire causes difficulties during facet preparation for butt coupling, even with the help from dicing to prepare the facets for coupling instead of conventional polishing. Sapphire is transparent up to 5 μm. However, it does have got any other advantages compared to other potential candidates such as SON, Silicon on Silicon Nitride, Si-on-porous Si or suspended Si which are much easier to fabricate, have lower cost, and exhibit lower propagation losses. Even though SOS wafers are used in electronics, it is more difficult to find good SOS wafers unlike SOI.

2.4.5 Silicon on porous silicon

Silicon on porous silicon has been demonstrated with 4 μm wide and 2 μm thick strip waveguides with 3.9 dB/cm propagation loss at 3.39 μm wavelength, which is shown in Figure 2.7 [69].

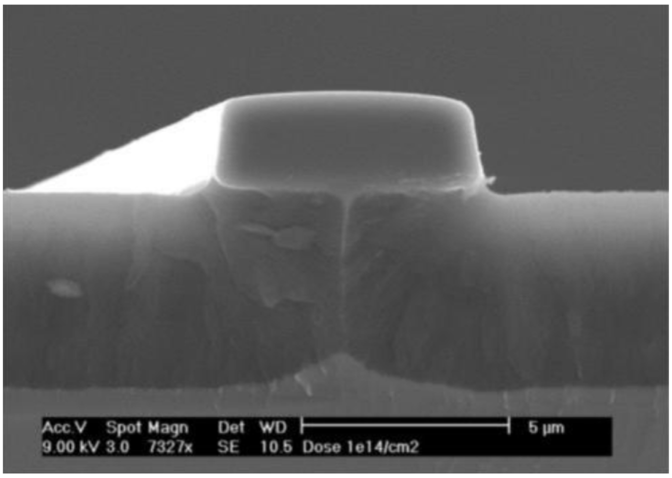

Figure 2.7: SEM image of cross-section of a Si on porous silicon waveguide, from [69].

The waveguide core is made of porous silicon which is fabricated by large area irradiation and oxidised after etching for the purpose of reducing surface roughness and therefore the scattering loss. It has been discussed that the loss might come from surface roughness and low resistivity Si has been used during processing. The refractive index of the porous silicon is determined by the porosity of Si and thus the refractive index can be adjusted for different applications. Since this material is made of Si it should be transparent up to 8 μm wavelength, however pores may oxidise and cause larger losses than predicted.

2.4.6 Suspended Si (Silicon membrane)

Suspended Si refers to SOI waveguides where the SiO_2 lower cladding has been removed. These waveguides have the ability to be transparent up to 8 μm. A low loss suspended Si waveguide with 0.8 dB/cm at 3.8 μm wavelength has been demonstrated with the lateral cladding comprising a sub-wavelength grating metamaterial to support the silicon waveguide and to access the bottom oxide at the same time [84] as is shown in Figure 2.8.

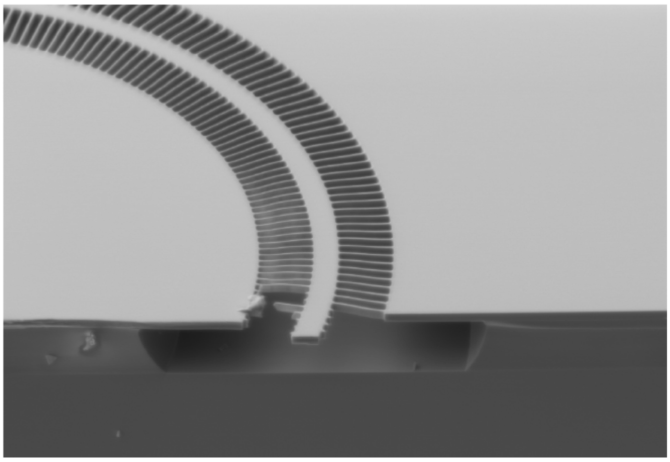

Figure 2.8: SEM image of cross-section of a bend that has been suspended after the isotropic etching, the inside and outside of the bend were fully etched, from [84].

There is another demonstration of suspended silicon waveguides with low loss of 3.1 dB/cm that operate at 7.67 μm wavelength, and other passive devices such as 90° bends and s-bends show losses of 0.06 ± 0.02 dB/bend and 0.08 ± 0.02 dB/bend respectively [85].

The main advantages of this approach are a simplified fabrication that includes only 1 etch step and better mechanical robustness since there is no reduction of the original SOI thickness, as the full top Si layer is used for both the core and the cladding and slab regions.

2.4.7 SiGe/Si graded index waveguide

There are demonstrations of the SiGe/Si graded index waveguides with very low propagation losses of 1 dB/cm at 4.5 μm and 2 dB/cm at 7.4 μm. Passive components such as Y-junctions, couplers and crossing were also demonstrated in same platform [86]. A linear graded stack is designed with 40% Ge concentration and a 10 μm thick Si layer as cladding, Figure 2.9 shows the waveguide cross-section.

The dimensions of the waveguide are: 3.3 μm width and 7 μm width for operation at 4.5 μm and 7.4 μm wavelengths respectively. An uncladded SiGe waveguide on graded index SiGe substrate is reported with a flat 2-3 dB/cm propagation loss from 5.5 μm to 8.5 μm wavelength range, with 6 μm waveguide thickness [87]. Compared with Ge-on-Si platform, the graded waveguide dimensions are larger and thus lead to less optical confinement which results in potential higher bend loss and vertical leakage.

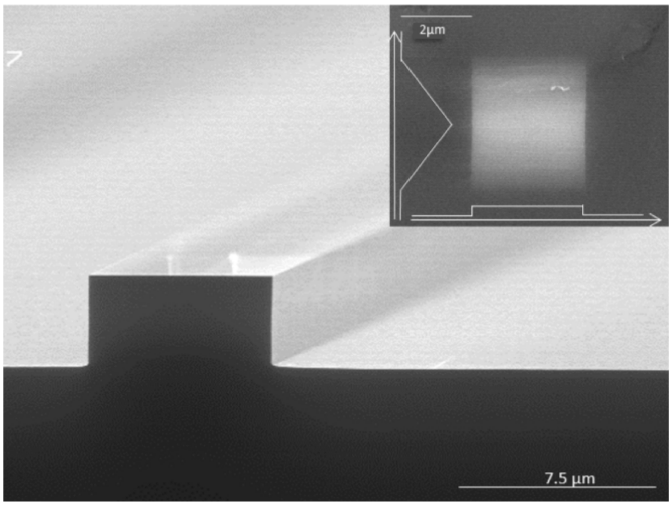

Figure 2.9: SEM image of cross-section of a SiGe waveguide after etching the core. Inset: cross-section of fabricated waveguide with Si cladding, vertical direction represents the intensity grading which is related to the variation of Ge concentration, from [86].

Also depending on the SiGe concentration, the transparency can be more restricted than when using Ge-on-Si platform. These waveguides can also have limited sensing application due to lower evanescent field.

There are also other demonstrations of GeSn integrated with Ge devices that can be potential candidates for integrated lasers or photodetectors around 2.5 μm. More information can be found in [73].

In this project, SOI has been chosen as the platform for the investigation of waveguide integrated photodetectors at 3.8 μm wavelength, considering the low loss nature of SOI in the targeting wavelength and the conveniency of SOI availability. It is necessary to introduce a high absorbance, integrable material as the “active region” for realising photodetection. 2D materials have attracted attention due to many advantages. The next section is going to demonstrate different types of 2D materials which are promising for photodetection, and why graphene has been chosen to be used in this project.

2.5 2-D materials and graphene for photodetection applications

This section will discuss different types of 2D materials, and the reason why graphene is chosen in this project. It will also give a literature review of graphene integrated with optical devices, and finally a review of graphene photodetectors will be presented.

2.5.1 2-D materials

Compared with traditional 3D photonic materials such as gallium arsenide (GaAs) and silicon, 2-D materials have advantages in many aspects: first, quantum confinement in the direction perpendicular to the 2-D plane leads to many distinctively different optical and photonic properties compared to their bulk parental materials [88–90]. Second, 2-D materials can easily be integrated with other photonic devices such optical cavities and waveguides, due to 2-D materials being released from the issue of "lattice mismatch" where layers of 2-D materials can form the heterostructures by van der Waals forces [91]. Third, 2-D materials have stronger optical absorption, for example a monolayer of MoS_2 absorbs 10% of normal incident light vertically from 610 nm to 660 nm [92], and finally a wide range of the electromagnetic spectrum can be covered by 2-D materials due to diverse electronic properties. Figure 2.10 shows the optical absorption spectra of some popular 2-D materials.

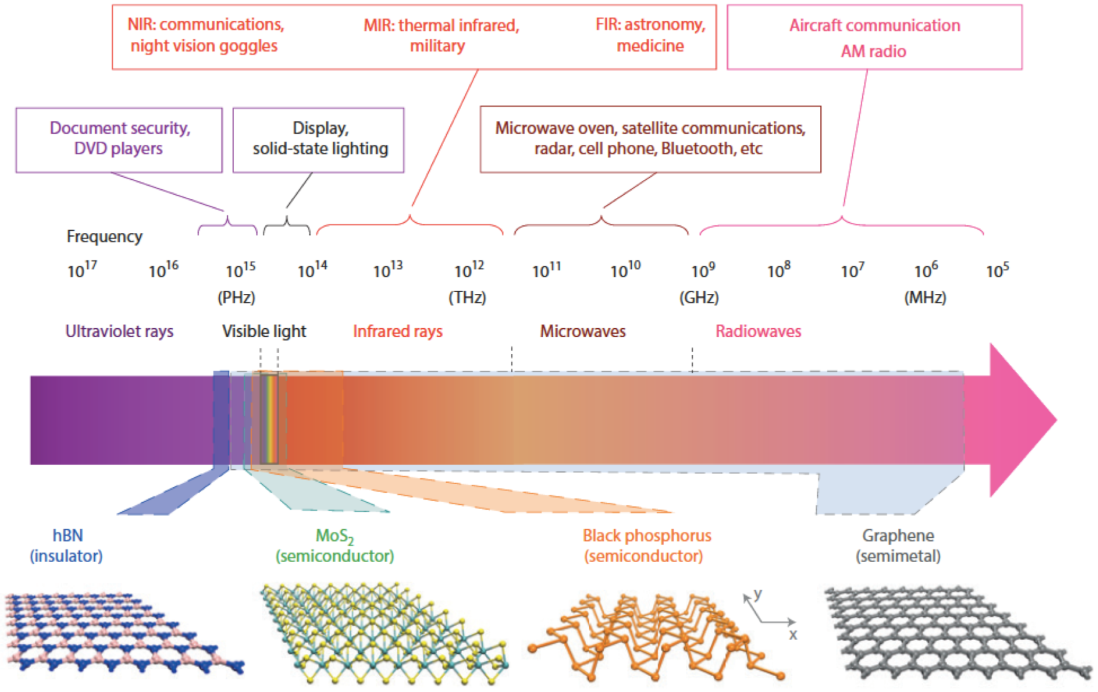

Figure 2.10: Electromagnetic spectrum, correspondent to the possible application to different spectral range, different 2D materials' spectral range and their atomic structures, from [53].

Graphene interacts with light from microwave to UV wavelengths [46], therefore having a great potential for various applications: light detection, modulation and manipulation across a wide spectral range. However, its gapless and semimetallic structure prevents graphene from being used for light emission. By contrast, single layer transition metal dichalcogenides (TMDs) such as molybdenum disulfide (MoS_2) and tungsten diselenide (WSe_2) are direct-bandgap structure semiconductors [89, 90], which indicates that they are promising for light emission applications in the near-infrared range. Hexagonal boron nitride (h-BN) is another type of 2-D material with around 6 eV bandgap which is larger than other 2-D materials. This makes it an ideal dielectric and it is used for electrostatic gating in 2-D material formed heterostructures since the “lattice match” is not critical in stacking of 2-D materials. Besides the mentioned 2-D materials, black phosphorus (BP) is another candidate with a direct bandgap of 0.3 eV in its bulk formation [93]. It should be noted that when decreasing the number of layers the bandgap will increase, because the enhancement of electronic confinement in the direction perpendicular to the 2-D plane, and the bandgap of monolayer BP is approximately 2 eV [94]. Benefiting from the wide selection of and combination of 2D materials, there is great promise for creating diverse photonic and optoelectronic devices and extending the frontiers of existing optical sciences.

In terms of this project, for the purpose of developing a waveguide integrated mid-infrared photodetector, graphene has a dominant advantage compared to other 2-D materials not only for the wide working wavelength but also the outstanding electronic and optical properties. The following subsection will discuss these properties of graphene.

2.5.2 Electronic and optical properties of graphene

In order to maximise the amount of photons that need to be converted into electron-hole pairs, a high material absorbance is necessary. The integration of 2-D materials into photonic devices has drawn much attention and it is very promising as 2-D materials intend to absorb a large amount of incident photons per layer. This subsection is mainly focused on the electronic and optical properties of graphene as the active region in a photodetector.

Single layer graphene was first demonstrated by Novoselov, Geim and their colleagues by graphite exfoliation in 2004 [41]. Graphene has excellent electrical properties, such as high carrier mobilities, high thermal conductivity, and linear dispersion [95], but it also attracts attention due to its optical properties. For instance, graphene can be utilised as a wideband absorber due to the gapless band structure. Terahertz detectors were also accomplished due to the high and tunable absorption [96]. As monolayer and few-layer graphene can be grown on copper foil commercially, a range of potential applications can be realised, among which one of the most attractive is graphene photodetectors.

The optical absorption mechanisms in graphene are divided into two processes: interband transition and intraband transition, which can be seen in Figure 2.11. Interband transition occurs when one electron in the “valence” band of graphene absorbs a photon and is excited to an empty state in the “conduction” band with the same momentum [97]. Interband transition can only happen when the filled state has the energy of ε = -$\hbar\omega/2$, and the empty state ε = + $\hbar\omega/2$, where ε is called Dirac energy. The interband transition is only permitted under the condition that the state of filled energy $\hbar\omega/2$ is larger than the absolute value of the chemical potential $|\mu_c|$. Otherwise this mechanism is blocked when $|\mu_c|$ is greater than $\hbar\omega/2$ due to the Pauli blocking. On the other hand, intraband transitions occur under the phonon assisted process, which happens in the far-infrared (FIR) to terahertz wavelength regions [97].

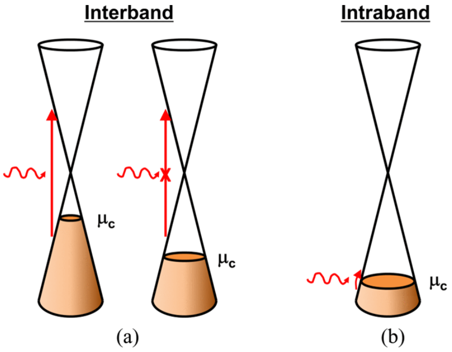

Figure 2.11: Two absorption mechanisms in graphene, (a) Interband transition, electron in the valence band of graphene absorbs a photon and get excited to the conduction band when the absolute value chemical potential $|\mu_c|$ is less than filled state energy $\hbar\omega/2$ (left), otherwise the interband transition is prohibited which is shown in left ; (b) intraband transition happens in the band and under the assistance from phonon, from [98].

With the control of absorption mechanism, waveguide-coupled graphene optoelectronic devices have potential to operate in the mid-IR wavelength region, and under such circumstances the absorption mechanism is dominated by the interband transitions [99–101]. Figure 2.12 sketches two different coupling methods [102]. The single layer graphene has a 3.3 $\mathring{A}$ thickness and the universal absorption of 2.3% for each monolayer under normal incidence [97]. By using the coplanar integration methods, the optical mode propagates in the silicon photonics waveguide and interacts with graphene at the same time, and thus can achieve a greater interaction length compared to the normal incidence situation, in which the interaction length is limited by the thickness of graphene.

In order to calculate the real part of the conductivity of graphene, from Ohm's law, the density of surface current can be expressed[97]:

$$\mathbf{J}_s\left(\mathbf{r},t\right) = \sigma_0 \mathbf{E}_t\left(\mathbf{r},t\right) \tag{2.5}$$

where $\mathbf{J}_s\left(\mathbf{r},t\right)$, is the surface current density, $\mathbf{E}_t$ is the electric-field component that is in the plane of graphene, σ_0 is the constant conductivity from interband transition $\sigma_0 = \mathrm{e}^2/4\hbar = 6.08\times10^{-5}\Omega^{-1}$, t is the component in the graphene plane. Thus, the time-averaged ohmic power dissipation per unit area Q_s (W/m^2) in the graphene layer is given by:

$$\left(Q\right)_s\left(\mathbf{r}\right) = \left\langle \mathbf{J}_s\left(\mathbf{r},t\right)\cdot\left(\mathbf{E}_t\left(\mathbf{r},t\right)\right)\right\rangle = \frac{1}{2}\sigma_0\left\langle(\mathbf{E}_t(\mathbf{r},t))(\mathbf{E}_t^*(\mathbf{r},t))\right\rangle = \frac{1}{2}\sigma_0\left|\mathbf{E}_t\right|^2 \tag{2.6}$$

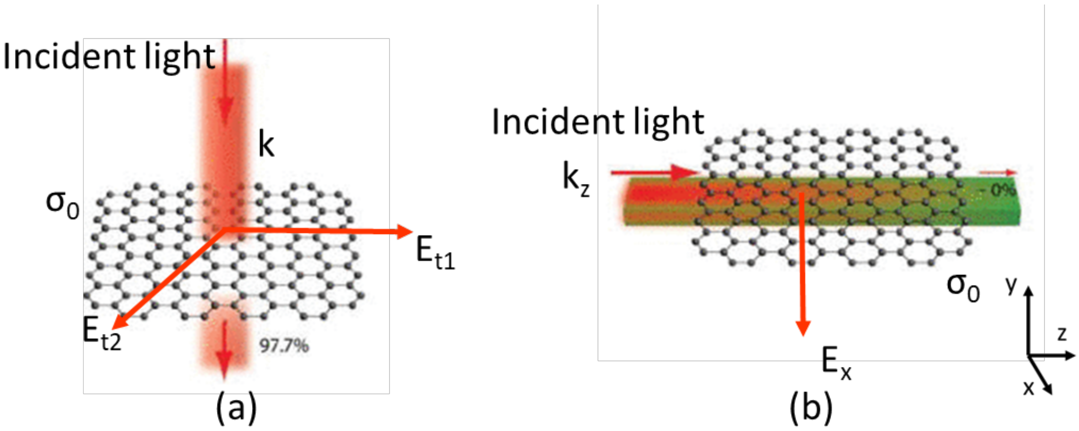

Figure 2.12: Schematics of two coupling methods. (a) In a normal incidence scenario, graphene exhibits the “universal” absorption coefficient of 2.3 %. (b) By integrating graphene on a silicon waveguide, the graphene/light interaction length is only governed by the length of the device, thus high absorption can be achieved, reproduced from [102].

In Equation 2.6, the factor one-half from the peak value is used in the electric field $\mathbf{E}_t$, which has two transverse components.

$$\mathbf{E}_t = E_{t1}\hat{\mathbf{t}}_1 + E_{t2}\hat{\mathbf{t}}_2 \tag{2.7}$$

$$(Q)_s = \frac{1}{2}\sigma_0 \mathbf{E}_t \cdot \mathbf{E}_t^* = \frac{1}{2}\sigma_0 \left(|E_{t1}|^2 + |E_{t2}|^2\right) \tag{2.8}$$

where $\hat{\mathbf{t}}_1$ and $\hat{\mathbf{t}}_2$ are two orthogonal unit vectors in the plane of graphene, while E_{t1} and E_{t2} are complex field amplitude.

The solution above can be used to solve absorption from interband transition under normal incidence. Ratio between the absorbed power by graphene compared to the total incident power can be expressed as:

$$\frac{(Q)_s}{I_{inc}} = \frac{\frac{1}{2}\sigma_0 \mathbf{E}_t \cdot \mathbf{E}_t^*}{\frac{1}{2}\varepsilon_0 c \mathbf{E}_{inc} \cdot \mathbf{E}_{inc}^*} = \frac{\sigma_0}{\varepsilon_0 c} = \pi\alpha = 2.3\% \tag{2.9}$$

where $e^2/4\pi\varepsilon_0\hbar c = 1/137$, ε_0 is the fine structure constant, c is the speed of light. In Equation 2.9, the relation $\mathbf{E}_t = \mathbf{E}_{inc}$ has to be fulfilled due to the boundary limitations, where $\mathbf{E}_t$ is complex field amplitude and $\mathbf{E}_{inc}$ is the absorbed optical power under normal incident [100].

The propagation loss of waveguide is negligible when compared to the optical absorption from graphene. Thus, in the z-direction, the power $P(z)$ of the waveguide mode decreases exponentially:

$$P(z) = P_0 exp(-\alpha z) \tag{2.10}$$

where P_0 is the waveguide mode power at z=0, α is the linear absorption coefficient (m^{-1}), and α is defined as the power absorbed by graphene per unit length normalised to total waveguide mode power:

$$\alpha = -\frac{1}{P(z)}\frac{dP(z)}{dz} = \frac{1}{P(z)}\int_W (Q(x))_s \, dl. \tag{2.11}$$

Here, from Figure 2.12 the SLG is parallel to the x-z plane, and has width W in the x-direction. The integral for the TE mode from Equation 2.8 can be expressed as:

$$\alpha(y_0) = \frac{\sigma_0}{2P(z)}\int_W \left|E_{in-plane}(x, y_0)\right|^2 dx \tag{2.12}$$

where y_0 is the position of the graphene plane [97, 103].

Compared to graphene, TMDs such as molybdenum disulfide MoS_2, tungsten disulfide WS_2, and molybdenum diselenide $MoSe_2$, exhibit much higher absorption in the visible to the near infrared range that extends beyond their energy band gaps, which makes these materials ideal candidates for ultra-thin photo-active materials [104]. The high optical absorption in TMDs is due to dipole transitions between the localised d states and the excitonic coupling of such transitions, which is well explained in [104, 90]. Due to its high bandgap and absorption in the deep UV region, hexagonal boron nitride (h-BN) has been considered as a promising UV photodetector [105]. Among all these 2-D materials, only graphene can interact with whole spectrum of MIR, makes it the only candidate to be used in this project.

2.5.3 Technology of graphene production

The key to future commercial uptake of 2-D technology is the availability of large scale material growth or synthesis methods. Chemical vapour deposition (CVD) is a well established technique in the semiconductor industry for growing a variety of conventional materials. Today, CVD can in principle fulfil the requirement of the large-scale growth of graphene and many 2-D materials of the TMDs family. However, the reproducible synthesis of TMDs on a large scale is still challenging, and the process technology is far from optimised. For example, it is not possible today to control exactly the number of atomic layers across a wafer or to grow monocrystalline films without grain boundaries [49, 106].

In terms of graphene production, various methods have been investigated, and they are divided into two categories: (1) top-down methods and (2) bottom-up methods. In the top-down methods graphene can be synthesised by isolation or exfoliation from the bulk formation under the application of external energy, such as micromechanical exfoliation, liquid-phase exfoliation or electrochemical exfoliation. On the contrary, the bottom-up methods represent approaches where atoms are deposited through chemical or thermal reactions onto the target substrate resulting in graphene synthesis. Such as chemical vapour deposition epitaxial growth on SiC, and other methods.

Right now, graphene production aims to achieve high yield, large areas, and controllable growth on various platforms. Some principle graphene synthesis methods are briefly described below.

1. Micromechanical exfoliation

   Micromechanical exfoliation involves using adhesive tape to peel off graphite pieces to obtain graphene as first demonstrated in 2004 [41]. It is the most basic way to fabricate single layer graphene, and the maximum graphene size that has been achieved was around millimetres size, after modification of the process [33]. Due to its versatility and low cost, great contribution has been achieved into fundamental research for example in the investigation of intrinsic properties of graphene. However, this method is unsuitable for large-scale application because of low throughput, and it is hard to control the shape, size and location of graphene.

2. Reduced graphene oxide

   Due to the limitations of using micromechanical exfoliation synthesis graphene, efforts have been paid to develop other approaches that can produce high quality graphene in high quantity, and without sacrificing high mobility. These approaches should provide a controllable graphene sheet thickness with uniform performance, as well as compatible integration with various substrates. Graphene oxide is developed from chemical oxidation of graphite, which has been widely used [107]. Single layer graphene oxide can be obtained as graphite oxide can be easily exfoliated through ultrasonication or mechanical stirring in a aqueous environment for long time [108]. Graphene can be produced from thermal or chemical reduction of graphene oxide to restore its structure. This method takes a long time but the chemical exfoliation approach restricts residue defects caused by incomplete reduction process. Compared with micromechanical exfoliation method, the reduced graphene oxide method produces lower quality graphene because conductivity and carrier mobility are degraded.

3. Chemical vapour deposition

   Using chemical vapour deposition (CVD) to make few layers graphene (FLG) has been reported almost 50 years ago [109]. There are many carbon sources that can be used during the CVD growth process, such as CH_4 gas, methanol or polymethyl methacrylate (PMMA), catalysed by metals to deposit carbon atoms on metal surfaces and large areas of graphene can be formed. The reaction occurs under high temperatures (usually 800-1000 °C) and vacuum environments [110–112]. In terms of metal substrates to be used during the CVD process, Cu is the most favourable because Cu surfaces lead to larger areas of monolayer graphene with larger grain sizes after annealing [113–116]. Recently, growth of 60 cm large areas has been achieved [117]. A simpler way of growth without a catalyst has been demonstrated by plasma-enhanced CVD [118]. Metal substrates can be easily removed after graphene is synthesised, making CVD grown graphene easily transferable to arbitrary substrates. Moreover, CVD grown graphene could be processed by microfabrication techniques, making it compatible for applications in high density optoelectronic devices and circuits.

4. Epitaxial growth on SiC

   Graphene can be grown by carbon segregation from silicon carbide (SiC) [119] or metal substrates [120], and high temperature annealing is required after the growth. It has been reported that with one method graphite can be produced from SiC, and methods of segregating graphene from graphite through Ni (111) have been under investigation for the last 30 years [113]. High quality graphene layers can be obtained from such a method in an argon environment and the following segregation from the SiC substrate can be achieved from an electronic decoupling process in hydrogen, which is suitable for wafer scale applications [121]. On the other hand, this method also has limitations, where SiC is more difficult to remove compared to metals used in CVD grown graphene mentioned above [122, 123].

Table 2.1 summarises different graphene synthesis approaches. In this project, CVD grown graphene is chosen due to fast synthesis speed and large scale can be achieved at the same time.

Table 2.1: Different graphene synthesis methods, reproduced from [124]

Catgory	Method	Thickness	Lateral	Advantages	Disadvantages	References
Top-down methods	Micromechanical exfoliation	Few layers	μm to cm	Directly from graphite Low cost	Very small scale producation	[41]
	Liquid phase exfoliation	Single and few layers	μm to sub μm	Low cost Unmodified graphene	Low yield sepatation	[125, 126]
	Electrochemical exfoliation	Single and few layers	500-700 nm	Single step action high electrical conductivity of functionalised graphene	High cost of ionic liquid	[127]
	Acid dissolution of graphite	Monolayer	300-900 nm	Scalable Unmodified graphene	Hazard acid	[128]
Bottom-up methods	Self-assenbly	Monolayer	100’s nm	Thickness controllable	Exist defects	[129]
	CVD	Single and Few layers	Very large	Fast	Low yield contains impurities	[109, 130, 131, 118]
	Epitaxial growth on SiC	Few layers	Up to cm size	Large area of pureness	Very small scale	[120, 113, 132–134]
	Unzipping of carbon tubes	Multi layers	few μm long	Controllable size	High material cost	[135, 136]

2.5.4 Photodetection mechanisms in graphene

The working mechanism of a photodetector is the conversion of absorbed optical power into electrical signal in the presence of a photocurrent or photovoltage. This subsection gives a review of the mechanisms related to graphene photodetectors. Photodetection mechanisms in graphene can be categorised into five main types: photovoltaic effect, photo-thermoelectric effect, bolometric effect, plasma-wave-assisted effect, and photogating effect [137]. This section gives a brief illustration of how each photodetection mechanism works.

2.5.4.1 Photovoltaic effect

The photocurrent generated from the photovoltaic effect is based on the separation of photogenerated electron-hole pairs by built in electric fields at junctions between positive (p-type) and negative (n-type) graphene doping regions. Photocurrent generated by photovoltaic effect is controlled by junctions. There are many ways to achieve the built-in field, such as chemical doping (adding chemical reactants) [138], using a split gate electrostatically [139], or by using materials with different work functions for the two contact electrodes [140–142]. In terms of split gate situations, the doping profile can be tuned to be p - or n - type depending on the gate voltages applied at the junction. The direction of the photocurrent only depends on the direction of the electric field, it has no dependance on the doping level [143, 144]. On the other hand, this process is different to conventional semiconductor ionisation process, where the carriers are accreted by a strong electric field, and known as avalanche break down. In graphene photodetectors, the density of photo-generated carriers decreases with increasing doping level. Moreover, photovoltaic current decreases with distance from the charge neutral point. Benefiting from the high carrier mobility, photovoltaic effect is very useful in high-speed applications [145].

2.5.4.2 Photo-thermoelectric effect

A temperature gradient is produced during the photo-thermoelectric effect. The electrodes act as heat sinks in the uniform doping channel, and the temperature gradient happens at the graphene-metal junction. Transportation of hot carriers plays an important part in graphene to be used in photodetection [146–149]. Electron-electron interactions result in photo-excited electron-hole pairs heating carriers in graphene very quickly ($\sim$ 10 - 50 fs) compared to several picoseconds needed to heat the lattice [150, 151]. The phonon energy in graphene is high ($\sim$ 200 meV), thus the carriers can hold a higher temperature than the lattice temperature (over several picoseconds time scale) before relaxation of lattice temperature begins [152]. Therefore, hot carriers created by the radiation field have an electronic temperature ($\mathrm{T_E}$) greater than the lattice temperature ($\mathrm{T_L}$). The equilibration of hot carriers in graphene takes nanoseconds time scale due to slow scattering rate between electrons and phonons. Therefore, a considerable photo-response can be created due to temperature differences between carriers by the Seebeck effect [148]. The seebeck effect represents the conversion of heat directly into electricity at the junction of electrodes with different work functions. Photoresponse from hot carriers contributes a large bandwidth and high operating speed.

2.5.4.3 Bolometric effect

The bolometric effect happens when the transport conductance is changed by heating caused by incident photons and further changes the conductivity of the channel. Bolometric effect is a photoconductive process, which does not generate photocurrent under zero-bias but only changes the conductivity of graphene under external bias. The changes of conductivity contains two parts: change of temperature dependent carrier density and change of carrier mobility. A bolometer measures the power of electromagnetic radiation by absorbing the incident radiation $\mathrm{d}P$, and reading out the resulting temperature difference $\mathrm{d}T$. Bolometers are commonly made from semiconductors or absorptive materials such as a-Si or VO_2 and are widely used at longer wavelength applications, even up to sub-millimetre wavelength range [153]. The sensitivity is defined by the thermal coefficient of resistance, $R_h = \mathrm{d}T/\mathrm{d}P$, and the response time of the bolometer, $\tau = R_h C_h$, is dependent on the heat capacity C_h [154]. The advantages of graphene is that for a given area it has a small volume and low density of states, which results in low C_h, giving a fast response time. Cooling by acoustic phonons is slow due to the point of Fermi surface of graphene, and it needs high T_e by phonons, making R_h high. Both reasons contribute to high sensitivity of the bolometric effect.

Compared to the photo-thermoelectric effect, that happens mainly at the metal-graphene junctions and in which the response is proportional to the incident light power, bolometric phenomenon is very strong under high-bias situation and mainly occurs at the centre of the junction.

2.5.4.4 Plasma-wave-assisted effect

Plasma-wave-assist effect (PET) in the nanoscale has the ability to detect THz radiation by the plasma-wave assisted mechanism, where a FET hosting a 2D electron gas can be act as a cavity for plasma waves. For example, a DC output signal can be generated in response to the plasma waves, when plasma waves are launched at the source. This is due to coupling of electromagnetic fields drives an electric field between the source and drain, the detection of radiation exploits constructive interference of the plasma waves in the cavity and thus results in a resonantly enhanced photoresponse [155]. Graphene's high carrier mobility makes it a promising material to be used for a room temperature THz detector [96]. However, no demonstrations of plasma assistant graphene detector integrated with silicon photonics has been demonstrated.

2.5.4.5 Photogating effect

Besides all the photodetection mechanisms that have been discussed above, photoresponse can also be generated by charge trapping at trap centers or by charge transfer between graphene and other materials. In terms of the photogating effect, one type of photo-generated carrier is trapped by the external trapping centers or transferred from external sources [156–160]. This charge transfer process leads to a change of carrier density within a graphene channel. As a consequence the conductivity of the graphene channel can be modified by the incident light. Before the generated photo-carriers recombine, they can transport multiple times along the graphene channel, contributing a large optical gain, thus the responsivity from the photogating effect can be very high, up to millions of A/W under the help from quantum dots [156]. As a comparison, responsivity in photo-thermoelectric and bolometric effects is limited to a few mA/W. It can be noted that longer photo-carrier life times represent higher photo-gain and larger responsivity, at the cost of lower operating speed. These devices saturate for high optical power, and the saturation threshold power is controlled by the density of trapping centres.

2.6 State-of-the-art graphene integrated photodetectors

As we demonstrated before, only 2.3% of incident light can be absorbed by monolayer graphene, even though the light-matter interaction is very strong with one-atom thickness [103]. This limits the overall responsivity of conventional graphene detectors, which are normally a few mA/W. Specifically, improving the optical absorption and responsivity have been investigated and also is one main challenges in this field. There are many approaches, such as a plasmonic antenna, that can be used to enhance light absorption, however they are often limited by narrow resonance peaks [161, 162]. Graphene and quantum dots or other light absorbers is another approach. High photoresponse can also be achieved through a photogating effect while sacrificing the operating speed.

2.6.1 Performance metrics of photodetectors

Several figures of merit are described in this subsection which are normally used to evaluate the performance of a photodetector, including responsivity, quantum efficiency, detectivity, and operating speed [144].

2.6.1.1 Responsivity

Responsivity (R) is one of the most important characteristics for a photodetector. It is defined as the photocurrent I_{ph} divided by the incident power P_{in}, where $R = I_{ph}/P_{in}$, or if the photovoltage V_{pv} is measured, responsivity is defined as $R = V_{pv}/P_{in}$. Responsivity commonly features the sensitivity of a photodetector converting optical input signal into electrical output signal.

2.6.1.2 Quantum efficiency

Quantum efficiency can equivalently describe responsivity, where the external quantum efficiency (EQE) is defined as the number of electron-hole pairs collected to produce photocurrent in unit time divided by the total number of incident photons at the same time: $\mathrm{EQE} = (I_{ph}/q)/(P_{in}/E_{ph})$, where q is charge of an electron, E_{ph} is the total incident photon energy. Internal quantum efficiency (IQE) is defined similarly as EQE, except that the absorbed photon number is considered instead of the total incident photon number in EQE. IQE is expressed as: $\mathrm{IQE} = (I_{ph}/q)/(A_{abs}P_{in}/E_{ph})$, where A_{abs} is the absorption coefficient in a given wavelength.

2.6.1.3 Detectivity

Detectivity and noise equivalent power (NEP) are normally used to determine the minimum detectable signal of a photodetector. NEP is depended on the noise power density (S_n) and responsivity of a photodetector, which is: $\mathrm{NEP} = S_n/R$. Detectivity (D) is defined as : $D = 1/NEP$, the inverse of the NEP.

2.6.1.4 Bandwidth

Definition of spectral bandwidth is the full width at half maximum (FWHM). Optical bandwidth values can be defined in either wavelength or frequency. Due to the inverse relationship between frequency ($\Delta\nu$) and wavelength ($\Delta\lambda$), the conversion factor is determined on the center wavelength (λ) or frequency and can be defined as: $\Delta\nu = \frac{c}{\lambda^2}\Delta\lambda$. A bandwidth can also indicate the maximum frequency with which modulated light can be detected with a photodetector.

2.6.2 Photodetectors based on graphene

A review of different types of the graphene integrated detectors is presented in the following.

2.6.2.1 Metal-graphene-metal photodetectors

The first demonstration of a graphene photodetector was based on a graphene transistor, in which the metal-graphene junction was illuminated by IR and visible light [145]. In the AC response from the metal (Pd)-graphene junction at the 1.55 μm wavelength, up to 40 GHz photoresponse was observed. The measurement was restricted by the upper frequency limit of the setup, however, modelling based on the RC constant of the graphene photodetector suggested that the bandwidth could reach up to 40 GHz [145]. For a symmetric junction configuration, no net photocurrent can be generated due to both contacts producing the same but opposite currents under illumination. A modified design was presented and is shown in Figure 2.13, an extraordinary increase in photoresponse was observed, which also allowed using the whole area to form the photodetector. This device contained electrodes with different work functions, so that asymmetric doping can be produced. Still, this device was tested under 1.55 μm pulses and the highest achieved data rate was 10 Gbits/s [163].

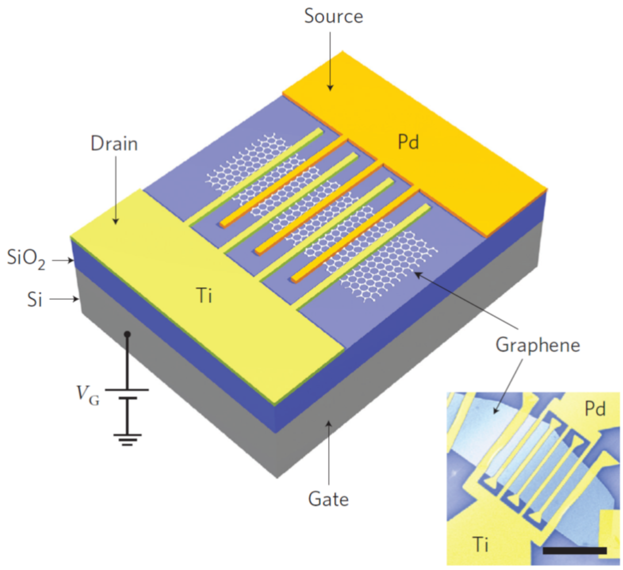

Figure 2.13: Schematic of the photodetector, electrode arms with different work functions can increase photoresponse efficiently, [163].

Benefiting from high carrier mobility and short carrier lifetime of graphene, graphene photodetectors based on metal-graphene-metal configuration can operate at high data rates. The drawback of this method was only 2.3% of incident light can be absorbed by graphene, which limited the responsivity of the device. Also two types of electrodes materials increased the number of fabrication processes and might damage the graphene during multi-lithography steps.

2.6.2.2 Sensitivity enhancement by cavities, waveguides and plasmonics

In order to further increase the photoresponse, monolithic integration of graphene transistor and optical cavities has been demonstrated. Graphene was transferred at the place where the maximum field was, and a 20-fold enhancement of the photocurrent was obtained at the resonant wavelength [164]. A study presented the enhancement for photoresponsivity when graphene was integrated with silicon waveguides and also proved the possibility of graphene silicon integration [165]. A wide band CMOS compatible graphene photodetector has been published. Graphene was placed on the silicon waveguide and a top gate and two side electrodes were fabricated. A few gigahertz bandwidth was achieved over all telecommunication bands, with maximum responsivity of 0.05 A/W, which was higher than that of normal incident light. The internal quantum efficiency was about 10%. Compared with examples that applied back gates, adding top gates on top of the waveguides required more critical fabrication tolerances. The schematic is shown in Figure 2.14 [165].

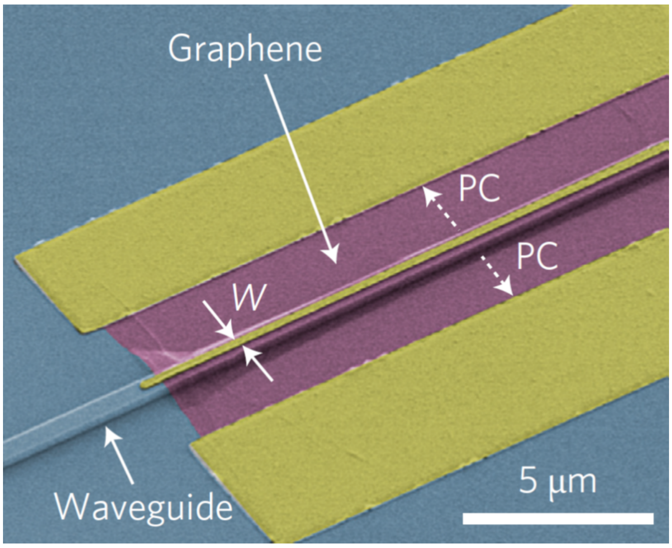

Figure 2.14: Photodetector based on the graphene integrated silicon waveguide, in which the evanescent field of the optical mode in SOI is coupled was the graphene [165].

Graphene integrated with optical waveguides is particularly interesting since this combination provides a clear enhancement of sensitivity. The optical mode propagates in the silicon-on-insulator waveguide and couples with the single layer graphene on the top of the waveguide as an evanescent field. A nearly flat and stable photoresponse covers all optical telecommunication ranges. A 20 GHz bandwidth and an open eye diagram at 12 Gbit/s with photoreponsivity of 0.1A/W in the near-infrared with (Figure 2.15) was presented in [166].

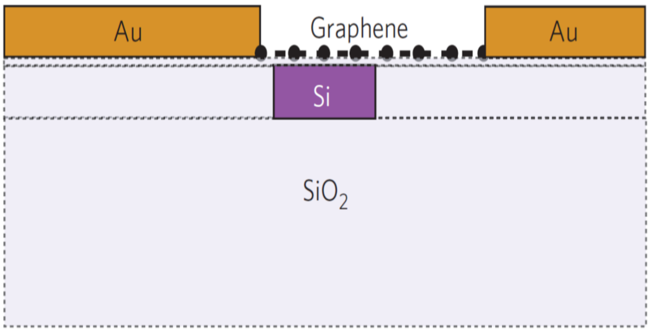

Figure 2.15: Schematic of a graphene photodetector that has the asymmetric electrodes structure [166].

A third method to improve photoresponse of graphene photodetectors is introducing surface plasmons. A combination of graphene and localised plasmons in metal nanostructures was adopted to realise strong field enhancement in nanometre gaps [167], where plasmonic nanostructures were fabricated near the contacts. Additionally, particular wavelengths can be selectively amplified based on dedicated nanostructure designs, making it possible to realise photodetection for selective wavelengths. By modifying the plasmon wavelength plus the excellent carrier mobility of graphene, this configuration can be used as both photodetector and plasmon enhancer. An investigation based on an array of 140 nm graphene ribbons on SiO_2 was demonstrated as a tunable IR photodetector with an enhancement of photocurrent on the order of 15 but the photoresponsivity was only 8 μA/W [168].

2.6.2.3 Graphene-semiconductor heterojunction photodetectors

Combined graphene planar junctions, with group IV materials and compound semiconductors can be treated like Schottky diodes [169, 170]. The performance of such devices is largely dependent on the semiconductor material. In order to maintain low dark current operation, a reverse bias working condition is compulsory for semiconductor-graphene photodetectors. A photodetector based on Graphene/Si heterojunctions was reported, with photovoltage responsivity over 10^7 V/W in photovoltage mode and with a responsivity of 0.435 A/W in photocurrent mode [171]. The drawback was that light was coupled into the detector from the out-of-plane direction which limited the light that could be absorbed by graphene.

The waveguide coupled photodetector achieved a 0.13 A/W detection at 2.75 μm wavelength under 1.5 V bias voltage, which shows that high performance MIR photodetectors are possible (Figure 2.16) [172]. Moreover, it was fabricated on suspended silicon waveguides. Also, no electrode was fabricated above the waveguide and there was no SiO_2

spacer between the graphene and the waveguide, which made the fabrication simpler compared to the designs with a spacer. Recently, a silicon-graphene plasmonic Schottky photodetector has been demonstrated, and at a reverse bias of 3 V, 0.37 A/W responsivity at 1550 nm wavelength has been reported. Figure 2.17 shows the cross-section of the device, which uses two metals with different working functions to form the Schottky diodes [173]. The LOCOS waveguides had smooth edge surfaces that can maintain the quality of the graphene without breaking, however, two different types of metals and LOCOS waveguides made fabrication more complex.

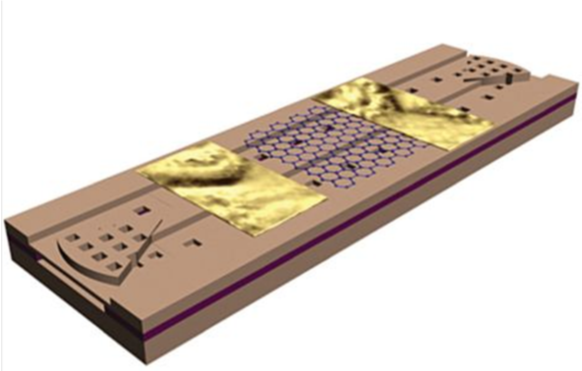

Figure 2.16: The schematic of the integrated suspended Si waveguide photodetector [172].

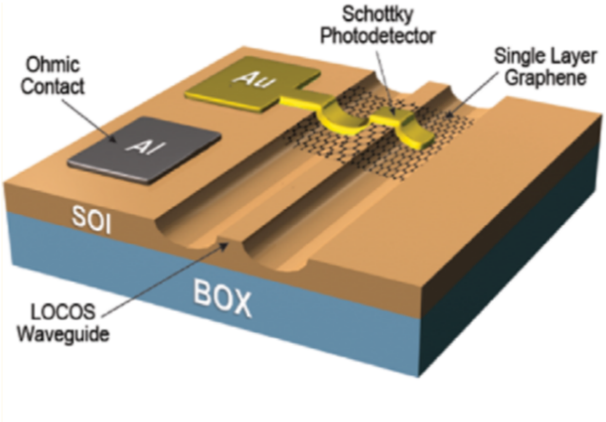

Figure 2.17: Graphene photodetector based on Schottky diodes, in which metals with different work functions were used for the electrodes, from [173].

2.6.2.4 Hybrid phototransistors

When combining graphene and another photosensitive material to form a graphene transistor, the residual opposite charges get amplified due to the charge transferring between graphene and the photoactive materials. Hybrid phototransistors can be used for photon detection at low intensities, by adapting appropriate sensing centres which have high absorption, and a single incident photon can provide multiple generated carriers [174, 175].

For example, a large field enhancement was observed when graphene and gold nanoparticles were illuminated at the plasmonic resonance wavelengths of the nanomaterials [161]. Arrays of semiconductor nanoparticles (PbS) have also been applied to increase photodetection. Carrier transfer to graphene results from the photo-excitation of PbS quantum dots. A significant enhancement of the device capacitance and huge gains up to 10^8 have been observed corresponding to responsivity of 10^7 A/W at room temperature and low light intensities. By contrast, large RC resonance restricts the device speed and shortens the operating wavelength spectrum of the nanoparticles [156].

2.6.2.5 Graphene based bolometers

Because graphene has no bandgap, the temperature dependence of the resistivity is low [176]. In order to increase the sensitivity of bolometric response, several approaches have been investigated. One approach has provided a large temperature dependence and low noise power by utilising the combined structure of superconducting wires and tunnel junctions between graphene and superconducting arms, which achieved 10^5 V/W responsivity but with low response time (10^{-8} s). The method takes advantage of the gap between metal wires and the contacts, which gives high temperature dependence around the critical temperature, instead of using the dependence of graphene itself. However, the performance was limited by the low tunnel barrier quality [177]. Graphene acts like an absorber and heat conductor in such a configuration while the superconducting arms act as the active components. Finally a single layer graphene detector with regular metal, which was based on Johnson noise thermometry, was presented as a potential approach for high sensitivity graphene bolometry with 80 MHz bandwidth [178].

2.6.2.6 Terahertz photodetectors

The terahertz (THz) range covers from 0.1 - 10 THz or 30 - 300 μm, and is also defined as the far-infrared (FIR) wavelength range. Photodetection in FIR was achieved by SLG plasma wave assisted FETs, involving a top gated FET with antenna structure. A maximum responsivity of 1.3 mA/W has been published, making such a configuration a candidate in fast imaging applications [179]. Graphene based broadband THz detectors were presented with 5 nA/W responsivity and 50 ps response rise times at 2.5 THz under room temperature operation [180]. So this type of photodetectors had low responsivities.

Table 2.2 summarises different types of graphene integrated photodetectors with related performance parameters.

Table 2.2: Summary of the state-of-the-art integrated graphene detectors.

Graphene Devices	Layer Number	Technology	EQE/IQE/PCE(%)	Response (mA/W)	Ref.
Graphene/Si Schottky junction	SLG	CVD	-	270 at 992 nm 0.17 at 2000nm	[181]
	3LG p-doped		IQE >65	435 (850-900 nm)	[171]
	SLG		-	320(850-900 nm)	[171]
Graphene on SiO_2	SlG on Si		-	0.13 A/W at 2.75 μm	[172]
Graphene/GaN Schottky diode	SLG		-	0.23 A/W at 360 nm	[182]
Graphene on SiO_2/Si	Bilayer	Exfoliated flake	-	1.3 at 0.292 THz	[179]
Metal-graphene-metal	Bilayer		EQE = 0.5 IQE = 10	6.1 at 1550 nm VIS - NIR	[163]
Graphene p-n junction	SLG (electr. Doping)		-	1.5 at 532nm (P = 30 μW)	[139]
	Bilayer		-	5 at 850 nm (T = 40 K)	[147]
	Trilayer	Exfoliated, edge contacted	-	10 at 514.5 nm	[183]
Flexible organic PDs	Graphene/PEDOT:PSS ink	Spray coating	-	0.16 A/W at 500 nm	[179]

2.6.3 Photodetectors based on other 2D materials

2D transition metal dichalcogenides (TMDs), such as MoS_2, compared to graphene, exhibit even higher optical absorption but narrower spectral bandwidth because of their limited electronic bandgaps. A short review of the TMD based photodetectors follows.

A TMD photodetector that used the built-in field at the MoS_2-metal interfaces Schottky configurations to drive the photocurrent with an impressive 880 mA/W responsivity at 561nm from an exfoliated MoS_2 flake has been presented [184]. The result was characterised under ultra-low illumination intensities of 24 μWcm^{-2}. However, compared to the novel Si avalanche PDS (3×10^{-14} WHz$^{-1/2}$) the noise equivalent power (NEP) of the MoS_2 photodetector is much smaller, 1.8×10^{-15} WHz$^{-1/2}$ [185]. Moreover, similar work has been carried out on CVD-grown monolayer MoS_2 and showed a remarkable responsivity of 2200 A/W in the vacuum condition and down to 780 A/W in ambient air [186]. Such a difference occurred because the carrier recombination in ambient air is enhanced compared to in vacuum. A more sophisticated device structure which contains two independent electrodes to produce a lateral, tuneable p-n junction in monolayer exfoliated tungsten disenlenide (WSe_2) has been reported. The WSe_2 flake was electrostatically doped and can be treated as either a PD, a solar cell or a LED, and under PD mode, a responsivity of 16 mA/W was achieved [187].

There are some groups working on photodetectors with heterostructures based on 2-D materials only, also known as van der Waals (vdW) heterostructures. An atomic-p-n diode made from exfoliated flakes of monolayer MoS_2 and monolayer WSe_2 showed a responsivity of 11mA/W at 650 nm wavelength [188]. One similar design has also been demonstrated with relatively low responsivity of 2 mA/W at 532 nm [189]. Another gallium telluride (GeTe) photodetector is demonstrated with a high responsivity of 800 A/W under liquid nitrogen environment by Wang et al. [190]. A multilayer detector made from a stack of layers of h-BN, graphene and TMDs was fabricated on a polyethylene terephthalate (PET) film, showing responsivity of 0.1 A/W at 633nm [191].

From the above short review we can see that photodetectors based on TMDs are more promising at shorter wavelengths due to the limited bandgap of the materials. TMDs can not only provide what conventional classical direct-bandgap semiconductors have, but also offer additional optoelectronic advantages in terms of mechanical flexibility and easy processing. Table 2.3 summarises the some of the TMDs detectors.

Table 2.3: Summary of the TMDs photodetectors.

TMD devices	**Layer number**	**Technology**	**-EQE/IQE/PCE (%)**	**Response (mA/W)**	**Ref.**
MoS_2 on SiO_2 photodetector	SL	Exfoliated flakes	-	880 A/W at 561 nm	[184]
WSe_2	SL (electr. doped)		PCE = 0.5	Electroluminescent at 1.547 eV	[187]
WSe_2/MoS_2	SL		EQE = 2.1	11 at 650 nm	[188]
h-BN/Graphene/WS_2/Graphene/h-BN	SL		EQE = 30	0.1 at 633 nm	[191]
MoS_2/Si Schottky junction	12 layers (8.26 nm)	CVD	-	8.6	[192]
WSe_2/MoS_2 p-n junction	SL p-n diode		EQE = 2.1	11 at 650 nm	[188]
MoS_2/graphene photodetector	SLG		IQE $\approx$ 15	10^7 at 650 nm	[193]

Table 2.4 summarises the photodetectors based on 2D materials with rapid photoresponse, and Table 2.5 summarises the photodetectors based on 2D materials with high responsivity.

Table 2.4: Fast photoresponse of photodetectors based on 2D materials

Materials	Wavelength (nm)	Frequency	Respond time	Reference
Ge/Si	1310	340 GHz	40 G bit/s	[194]
G/Si waveguide	1550	41 GHz	50 G bit/s	[195]
Graphene	1450-1550	20 GHz	12 G bit/s	[166]
BP/Si	1550-1580	0.2 MHz - 3 GHz	3 G bit/s	[196]
Graphene	1550	262 GHz	2.1 ps	[197]
MoS_2	452	300 GHz	5.5 ps	[198]
WS_2/G	390	-	1 ps	[199]
G/MoS_2/Si	365-1310	-	270 ns , 350 ns	[200]

Table 2.5: High responsivity photodetectors based on 2D materials

Materials	Wavelength (nm)	R (A/W)	Bias (V)	Respond time	Reference
WSe_2/G/MoS_2	400-2400	1 x 10^4	1	53.6 μs	[201]
PbS/MoS_2	400-1500	6 x 10^5	1	0.35 μs	[202]
Graphene/BiI_3	400-750	6 x 10^6	-	8 ms	[203]
WSe_2	500-900	1.8 x 10^5	2	23 ms	[204]
GaTe/MoS_2	473	21.83	1	7 ms	[205]
BP	310-1240	9 x 10^4	3	1 ms, 4 ms	[206]
PbSe/TiO_2/G	350-1700	0.506	1	50 ns, 83 ns	[207]
WSe_2/G	532	350	1	50 μs, 30 μs	[208]

2.7 Summary

This chapter describes the theory of planar photonic waveguides and multiple detector platforms that can be used in the mid-infrared. A short review of 2-D materials is also presented. Due to its electronic and optical properties graphene, is a promising material to be used for photodetection. A detail description of graphene synthesis methods, graphene photodetection mechanisms and a review of graphene integrated photodetectors are presented. From the literature, investigation of graphene based photodetectors have been more focused on the telecommunication band and NIR range, while fewer demonstrations in the MIR can be found in the literature. The longest demonstration of graphene waveguide integrated photodetector is at 2.75 μm [172].

In this project, SOI waveguide integrated graphene mid-infrared detectors are demonstrated at 3.8 μm wavelength due to the existence of the quantum cascade laser, by using the evanescent coupling method, realising long graphene-light interaction lengths and achieving larger absorption than 2.3 % from normal incidence. In terms of electrodes design, a metal-graphene-metal configuration is adopted, where asymmetry electrodes are fabricated on the sides of SOI waveguides. Photocurrent is generated under the photo-thermoelectric effect.

The next chapter will present the simulation, fabrication processes, experimental setup and the characterisation result of the SOI waveguides that are designed for building up a graphene integrated photodetector in the mid-infrared.

Chapter 3

Simulation, fabrication and characterisation of mid-infrared waveguides

This chapter describes the simulation software, the fabrication processes for the passive devices, the experimental setup for characterising integrated photonic devices, and the characterisation results of silicon-on-insulator mid-infrared waveguides at 3.8 μm wavelength. The instruments that have been used for testing both passive and active photonic components are presented.

3.1 Simulations

Commercial simulation tools are very helpful in simulating the performance of photonic components and devices. In this project, Photon Design Fimmwave [209] and Lumerical [210] were used to aid the design and optimisation of both the passive and active devices. This section briefly introduces both software packages.

3.1.1 Fimmwave

In Fimmwave, a basic 2-D cross-section of the waveguide is simulated using the Film Mode Matching (FMM) solver, which is based on Sudbo's FMM method [209] taking into account the losses of the material used. The FMM is used due to higher accuracy than other available approaches within the software when simulating rectangular geometries with high-index-contrast interfaces. As the FMM is a semi-analytical algorithm, high-index-contrast interfaces can be treated as a relatively low number of uniform refractive index regions, thus improving the simulation efficiency.

3.1.2 Lumerical

Lumerical MODE solutions software package [210] has also been used in this project. MODE solutions is capable of mode analysis, and bidirectional eigenmode expansion. The finite difference eigenmode (FDE) solver in MODE solutions is used to calculate the spatial profile and frequency dependence of modes by solving Maxwell's equations on a cross-sectional mesh of the waveguide. The FDE solver calculates the mode field profiles, effective index, and loss. Integrated frequency sweep can be also used when calculating group delay, dispersion, etc.

3.1.3 Mask design

The layout of the chip for both waveguides and other components was carried out adopting a combination of the L-edit [211] layout design software and a group of C++ functions written for the purpose of drawing generic integrated photonic components as well as system components. The C++ functions can be called from the L-edit program, where all parameters can be defined through the C++ code. By doing so, a large amount of time can be saved when drawing complex layouts with a great number of variations.

A library of C++ functions was created for automating alignment between various components and to create a series of devices with changeable parameters. Examples for such scenario can simply be waveguides with increased lengths for propagation loss characterisation or to investigate the grating coupler efficiency. Two types of functions were created: one is devices that are commonly used in various designs and remain the same, such as grating couplers, tapers and waveguides with a certain width, others are files that combine different functions to build up a complete structure at a higher level or an entire system design.

3.2 Fabrication

The fabrication process flow which takes place at the Southampton Nanofabrication Centre is described here. Layout design was carried out by myself, while Dr Ali Khokhar transferred the mask design into an e-beam file and implemented the e-beam lithography, rest of the fabrication were carried out by myself.

1. Layout design and transformation into the e-beam file

   L-edit software is used to design the chip layout and it is then exported in the GDS-II file format. GenlSys [212] is used to convert the GDS-II file to .V30 file format before importing it into the e-beam BEAMER software. This powerful software tool can perform logic editing operations on desired layers, and can also adjust e-beam resolution, e-beam dose, spot size and other parameters for different exposure needs.

2. Initial wafer clean

   Before any fabrication processes start, the wafers are cleaned. The initial cleaning processes are to put wafers into RCA1 (NH_4OH:H_2O_2:H_2O mixture with ratio 1:1:5), RCA2 (HCL:H_2O_2:H_2O mixture with ratio 1:1:5) and followed by dipping in buffered HF (1:20 with HF: NH_4F). The RCA1 clean is used to remove organic contaminants left on the wafer surfaces, polarised H_2O and NH_4OH molecules attach themselves to any of those contaminants and then drive each other away. RCA2 removes metallic ions completely because it can react with most of the metals and form soluble chlorides. Then, buffered HF will strip the oxide layer and passivate the silicon surface with a hydrogen termination.

3. Electron-beam lithography (Figure 3.3 (a)-(c))

   ZEP 520A photoresist is spun onto the wafer at a speed of 2360 rpm, which produces a photoresist layer of 500 nm thickness. After that, the wafer is baked for 3 minutes at 180°C. Then Espacer is spun on to the wafer at a speed of 2000 rpm, which can increase the conductivity of the resist during writing. The wafer is written using a JEOL JBX-9300FS e-beam tool. In order for the e-beam tool to be able to write all components from different layers in the designed places, detail and fine alignment marks are crucial, thus alignment marks have to be written in the first step. Figure 3.1 shows a GDS design with alignment marks at the corner of one chip. To decide whether other components are written together with the alignments is dependent on the etch depth of the first passive devices, such as waveguides, grating couplers and tapers. In this project, alignment marks have the same etch depth as other passive components, thus all these devices and alignment markers are written in the same step.

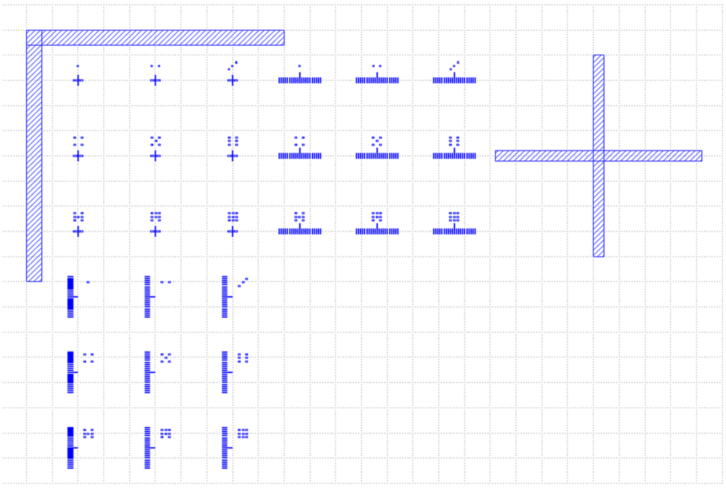

Figure 3.1: GDS with algnment marks at the corner of each chip.

After the writing, the wafer needs to be developed in ZEDN50 photoresist developer for 2 minutes and 30 seconds, and then the wafer is rinsed in IPA for 30 seconds and blow dried with N_2.

4. ICP silicon etching (Figure 3.3 (d))

   The written wafers are etched in the Oxford Instruments ICP 380 system. Before the etching process, a 20 minutes conditioning period is necessary, so as to create a chamber atmosphere that is the same as during the later etching. The conditioning wafer is made from a plain silicon wafer with thick S1813 photoresist after hard baking on the hotplate. The ICP silicon etch uses SF_6 (25 sccm) and C_4F_8 (45 sccm) gases, at the pressure of 15 mTorr and temperature of 15°C with 100 W DC power and 800 W RF power. The etch rate of silicon is around 3.5 nm/sec, and the thickness of the etching layer is monitored by using an ellipsometer to measure it in a 1×1 mm metrology box that has been defined in the mask design and has the same GDS number as the waveguide layer. The remaining photoresist ZEP is removed from the wafer by using Asher for standard cleaning process for 15 mins. Figure 3.2 shows an ICP chamber [213].

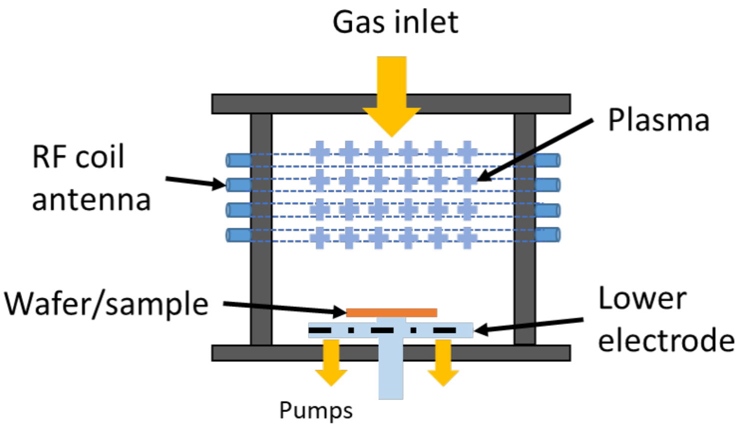

Figure 3.2: ICP chamber diagram, modified from [213].

5. Wafer dicing

   After the lithography and etching processes, the wafer is diced into 30 mm × 40 mm samples by a dicing saw. Before dicing, a thick layer of S1813 photoresist is spun onto the wafer and baked for 1 minute under 110 °C to act as a protection layer, and then the back side of the wafer is stuck onto an adhesive plastic film. The wafer is secured by a supporting ring and then fitted into the dicing saw.

After dicing, all the samples are rinsed in acetone, IPA and DI water for 3 minutes each in an ultrasonic bath, and are blown dry with a N_2 gun, and finally the O_2 plasma asher is used to remove any remaining solvent for 10 minutes.

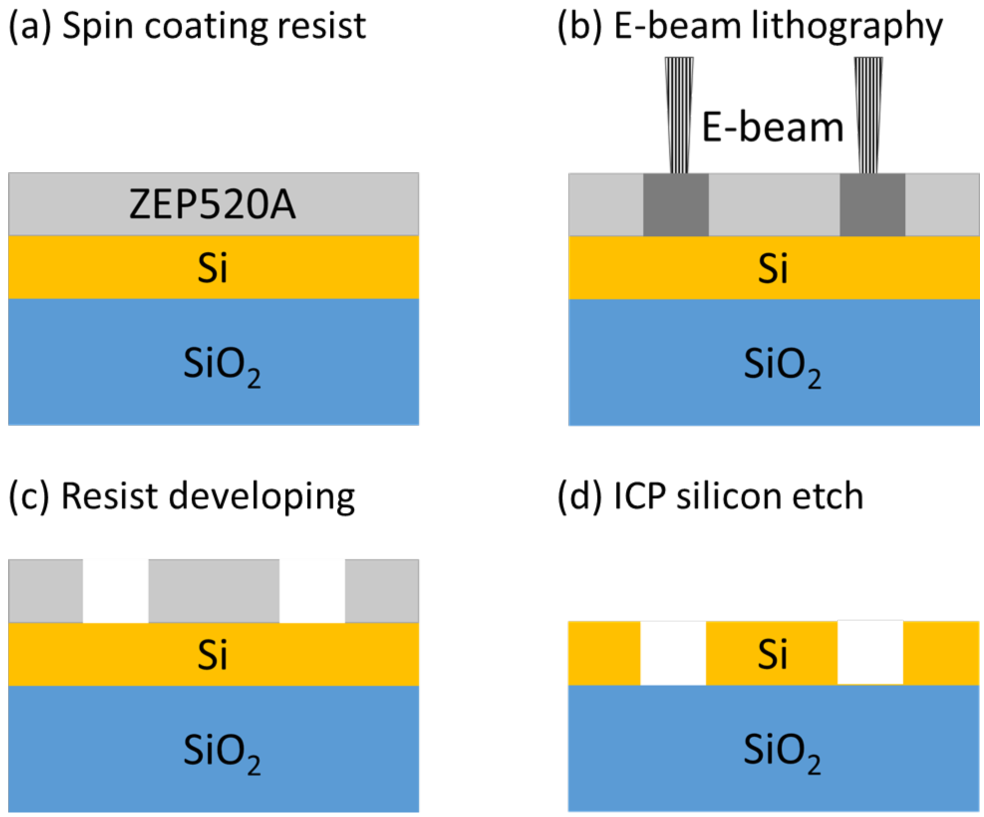

Figure 3.3: Diagram of cross-section images of silicon waveguide fabrication processes.

3.3 Experimental setup

The illustration of the experimental setup for characterising MIR passive components is shown in Figure 3.4 [214].

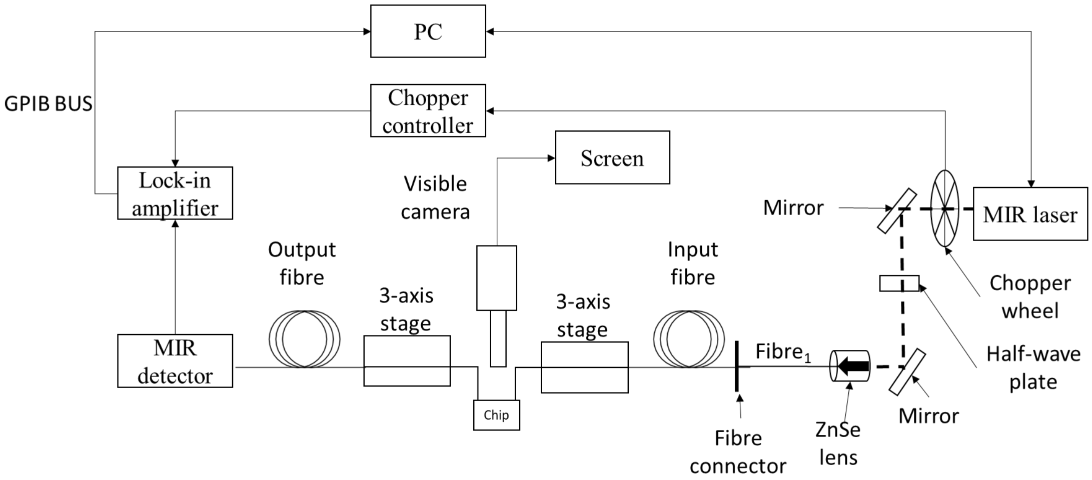

Figure 3.4: The schematic of the experimental set up used for characterisation of MIR photonic devices. The dash line represents the free-space beam, modified from [214].

A tunable quantum cascade laser (QCL) which operates at 3.71-3.90 μm is utilised as the source. Light from the laser passes through a chopper which operates at a frequency 400 Hz, before passing through a half-wave plate for controlling the polarisation and two mirrors that are used to control the angle of the incident light. The beam is then coupled through a ZnSe lens (0.5-20 μm transmission) into the mid-IR optical fibres, which have low loss within this range. Then, light is transmitted through mid-IR optical fibres and is coupled to the chip via grating couplers.

The test sample is placed on a stage, while the optical fibre holders are placed on three-axis stages. The stages can be manually tuned for rough alignment and also tuned by piezo-controllers for fine adjustments. A visible camera was used for visual control of the optical fibre position relative to the grating couplers. All the characterisation equipment is connected by GPIB bus and controlled by LabView program or Python scripted programs.

3.3.1 Equipment details

3.3.1.1 Quantum cascade laser

The QCL is a commercial product manufactured by Daylight Solutions [215], and it has an operating range from 3.71 to 3.90 μm in either continuous wave (CW) or pulsed modes. The laser operates at room temperature ($21°C$), thus a chiller is required to maintain the temperature. The circulating coolant is a mixture of water and isopropanol. In CW mode, the laser has a maximum output power of around 150 mW at the peak operating wavelength of 3.8 μm Figure 3.5. The laser has a nominal tuning accuracy of $\pm$ 0.5 cm^{-1} ($\pm$ 1.9 nm at $\lambda = 3.8$ μm), whilst the nominal linewidth is $\pm$ 0.003 cm^{-1} ($\pm$ 11 pm at $\lambda = 3.8$ μm). The optical power is determined by the laser current, the operating wavelengths are tuned by a laser controller which is supplied by the manufacturer, and which can be controlled through a LabView [216] program on the PC (Figure 3.4).

3.3.1.2 Detector

The detector is model IS-1.0 from InfraRed Associates Inc [216]. The detector needs liquid nitrogen to cool down, which is achieved by pouring the liquid nitrogen into the detector's cavity using a funnel. Based on the information provided by the manufacturer, the bandwidth is 150 kHz. In order to improve the signal to noise ratio, the output of the detector is connected to a pre-amplifier (INSB-1000 Pre-Amp [216]) which is connected to a lock-in amplifier. Figure 3.6 [214] shows the detectivity spectrum of the InSb IS-1.0 detector.

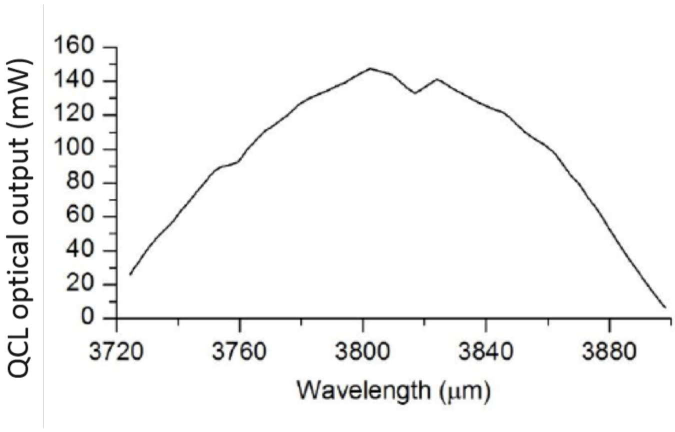

Figure 3.5: QCL output power vs emission wavelength; data are provided by Daylight Solutions.

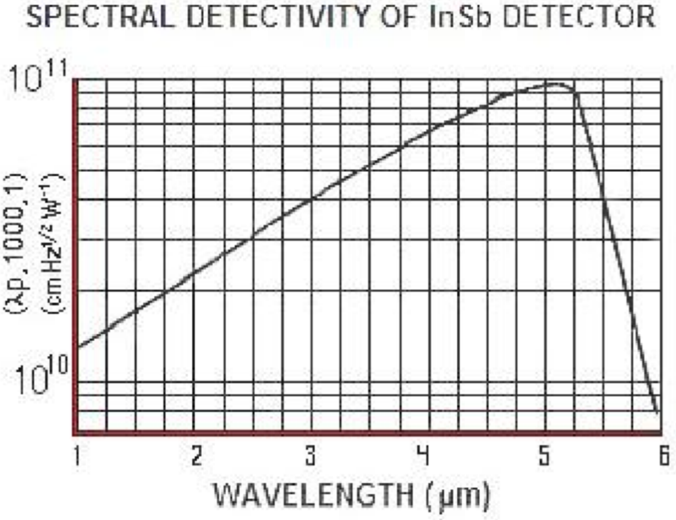

Figure 3.6: The detectivity spectrum of the InSb IS-1.0 photodetector, modified from [216].

Another HgCdTe based detector made by Vigo System [217] is available and it can be also used for detecting the MIR light. This photodetector features a four-stage thermoelectrically cooled IR photovoltaic detector. The detector has a 400 MHz bandwidth with a detectivity of $6 \cdot 10^{10}$ cmHz$^{1/2}$W^{-1}. Another advantage of this detector is that it does not need liquid nitrogen. This detector is also connected to the pre-amplifier and the lock-in amplifier to extract the measurement signal.

3.3.1.3 Optical fibres and fibre preparation

The fibres used for the characterisation of MIR devices are fluoride based MIR single mode fibres fabricated by Thorlabs [218]. The fibres are transparent from 300 nm to 4100 nm.

Before the fibres can be used, they need to be stripped and cleaved:

1. The external coating is around 4 mm in diameter and can be cut by a stripper.
2. The second coating layer is a buffer layer, which is around 800 μm in diameter, this layer can also be stripped directly by a stripper.
3. The final coating contains a 250 μm diameter outer layer and a 125 μm diameter inner layer. The fibre needs to be dipped into acetone for about 2 minutes, and then the fibre can be stripped carefully, using a Miller type stripper. The fibre core is 9 μm in diameter.
4. The stripped fibre is cleaved by a York FK11 fibre cleaver. The cleaver contains two clamping levers that ensure the fibre is secured. Then tension is applied upon the fibre by pulling one lever to make the clamps part. In the end, the lever is pulled and forces a diamond blade to move forward and finish cleaving. After each cleaving, both the fibre holder and the diamond blade must be cleaned by isopropanol.

3.3.1.4 Lock-in amplifier

The output of the detector pre-amplifier is connected to a Signal Recovery SR7265 lock-in amplifier [219]. The lock-in amplifier is also connected to the chopper wheel controller that modulated the laser output, thus it can lock onto a signal at this frequency in the detector output, increasing the signal to noise ratio. The lock-in amplifier is also connected to the PC through the GPIB bus and provides the LabView program with the measured transmission which is plotted against the laser output wavelength.

3.3.1.5 Polarisation control

As already mentioned, it is important to control the polarisation state of light that is coupled into the sample. The QCL laser produces TM polarised light ($>$ 100: 1, TM: TE). To obtain TE polarised light at the input of the chip, the QCL polarisation is rotated by a 90° by a half-wave plate, which is placed between the output of the QCL laser and the fibre input. The half-wave plate is made from cadmium thiogallate ($CdGa_2S_4$), which is transparent from 0.47 - 9.5 μm, and there is also an anti-reflection coating to eliminate the back reflection into the laser.

3.4 MIR silicon waveguide

3.4.1 Waveguide simulation and design

The SOI waveguide was simulated as a 2-D waveguide using the Lumerical MODE package as described before. Figure 3.7 shows the optimised TE mode profile by changing the width of the strip waveguide, which 1.3 μm wide and 500 nm thick for single mode propagation was chosen with the simulated propagation loss of 0.27 dB/cm for TE mode at 3.8 μm wavelength. The waveguide width is chosen to be 1.3 μm because it is the largest width to support a single mode and it also reduces the sidewall roughness. The minimum waveguide propagation loss of 1.3 μm width waveguide at the 3.8 μm wavelength is 1.28 ± 0.65 dB/cm [220].

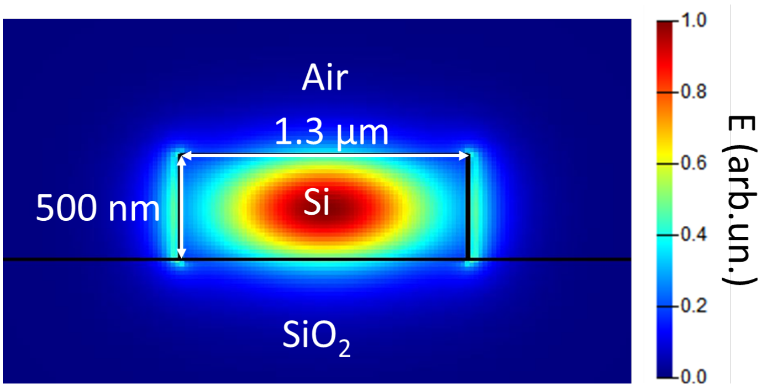

Figure 3.7: Diagram of the rib waveguide cross-section, and the fundamental TE mode.

By using the same mask design method mentioned before, the layout of the waveguide propagation loss section is presented in Figure 3.9. Light can be coupled into the chip from the fibre by either "in-plane coupling" method or "out-of-plane coupling" method. In the "in-plane coupling " method also known as butt-coupling method, the fibre is in the plane of the waveguides and is aligned to the waveguide facet. On the contrary, for the "out-of-plane coupling" method also known as grating coupling method, the fibres are held on 3-axis fibre holders with a fix input angle to the chip surface. The grating coupling method is easier for optical alignment compared to the butt coupling, because the position of fibre can be determined accurately by the fibre holder. The grating coupling has higher alignment tolerance than butt the coupling method, where a NIR source is needed for initial alignment.

By using the grating coupling method in this project for the purpose of avoiding potential inconsistencies that might appear compared to the in-plane coupling method, light can be coupled in and out of the waveguides through focusing surface grating couplers (Figure 3.8). The focusing grating couplers that have been published in [221] have been used in this project.

At each side of the grating coupler, there is a taper that is connected to the end port of the grating coupler. The taper was designed to improve the performances of the grating coupler and to make the coupling from the grating to the waveguide more efficient. Figure 3.8 shows the GDS design of the focusing surface grating. The magnified image (a) shows the dimensions of the design. The arrayed holes (in blue colour) are the structures that been etched by the ICP and the red area are the top silicon surface remained. Each etched hole had 1 μm width and 0.25 μm height, and 1 μm period.

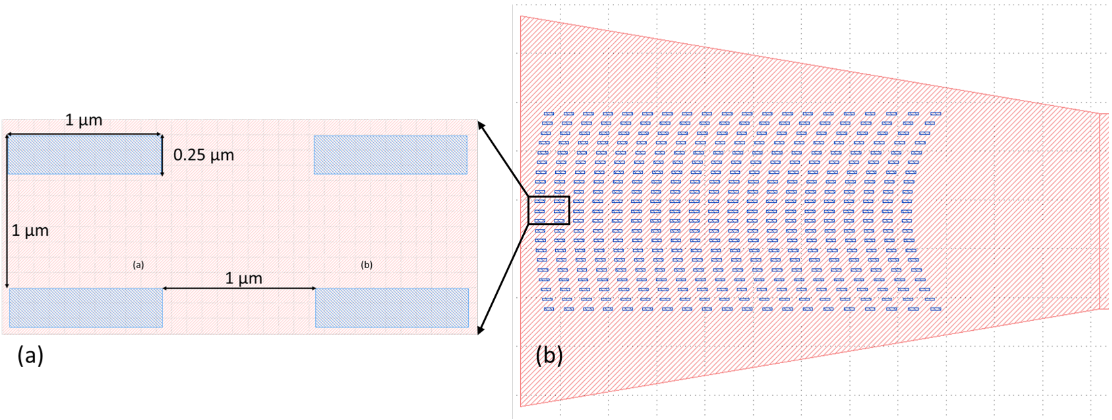

Figure 3.8: (a) Magnified image of the GDS design of the grating coupler, (b) GDS design of the focusing surface grating coupler. The arrayed holes (blue colour) represent the holes get etched and the rest of the silicon surface remained (red colour).

3.4.2 Waveguide propagation loss measurement

For all the waveguides, propagation loss is measured by the cut-back method [222], which is sketched in Figure 3.9.

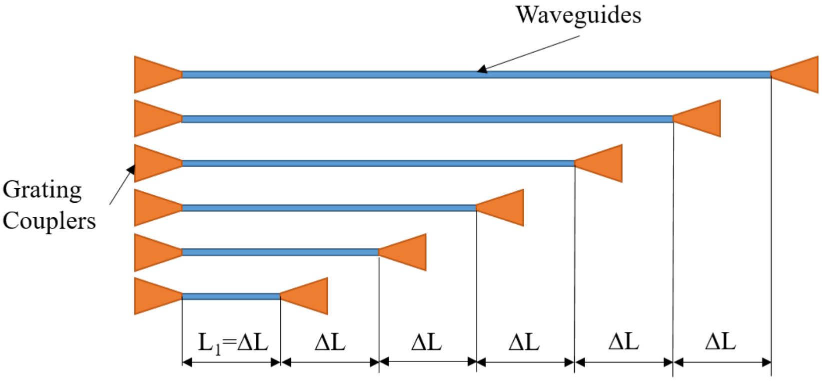

Figure 3.9: Schematic of the cut-back method, in which the waveguide length is varied while other parameters are kept same, from [222].

The power loss per unit length of the waveguide can be obtained by measuring the optical transmission through waveguides with increased length with the same input and output grating couplers. By using the method, many components that influence the total loss can be removed, such as the bend loss, grating coupling loss and variance across the wafer surface during the fabrication. The waveguide loss can be calculated from:

$$\alpha = (\frac{1}{L_1 - L_2}) ln(\frac{I_2}{I_1}) \tag{3.1}$$

where α is the propagation loss (cm^{-1}), L_1 and L_2 are the lengths (cm) of two waveguides, and I_2 and I_1 are the measured transmission powers for each waveguide. The absorption in dB/cm^{-1} can be obtained by using the following relation: α [dB/cm] = 10 $\times$ $log_{10}\alpha$ [cm^{-1}] = 4.34 $\times$ α [cm^{-1}]. With a number of measured waveguides, a graph of normalised optical loss (dB) against propagation length (cm) can be plotted, and the gradient of the best-fitted line will give an estimate of the waveguide loss in dB/cm.

Within all the measurements, the scanned transmission after passing the device is measured and normalised to a straight waveguide, which can eliminate the influence from dependences of the QCL output power and any other wavelength variation from the setup. The grating coupler design is modified for the 3.8 μm design and more details can be found in [223].

3.4.3 Waveguide characterisation

The fabricated samples were tested utilising the MIR characterisation setup mentioned before for passive measurements, in the 3715 - 3880 nm wavelength range. Figure 3.10 shows the loss measurement of the 1.3 μm wide waveguide using the cut-back method at the 3.8 μm wavelength. The x-axis is the length difference and y-axis the normalised transmission. The propagation loss of the waveguide is the gradient of the fitting line, which is approximately 2.5 dB/cm (seen in Figure 3.10).

Compared with the simulated propagation loss value 0.27 dB/cm, the measured 2.5 dB/cm is larger, the increasing of propagation loss might come from the roughness of the waveguide sidewall from etch, there might be other contamination or dirt on the chip.

3.5 Summary

This chapter presented a brief review of the simulation tools that have been used in this project, and fabrication processes for passive components, and a detailed illustration of all the equipment that is needed for passive optical measurements. Moreover, the characterisation results of silicon waveguide in the MIR are presented.

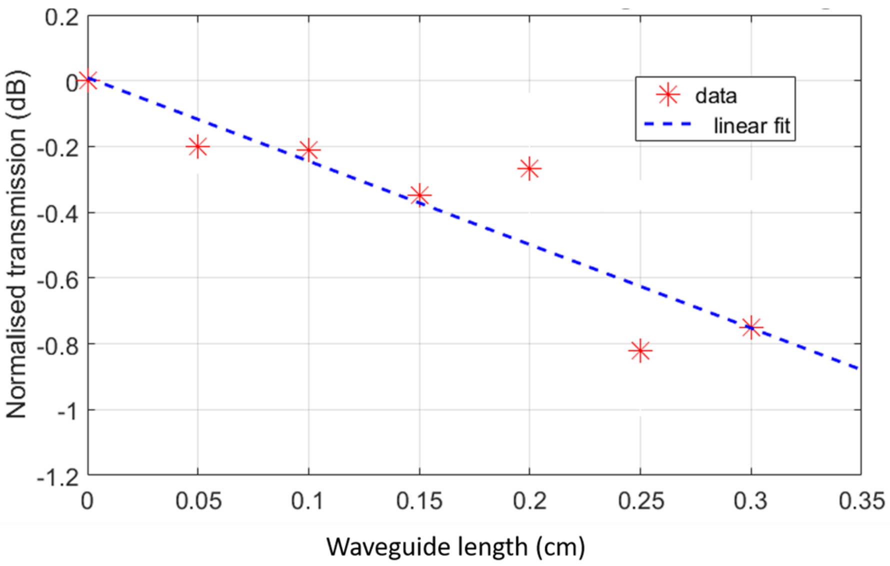

Figure 3.10: Loss measurement of 1.3 μm width waveguide by the cut-back method at 3.8 μm wavelength, the propagation loss is around 2.50 dB/cm.

In terms of the simulation software: Fimmwave and Lumerical packages are chosen due to not only their popularity but also their efficient performance. MODE solutions from Lumerical packages is used to simulate the mode profile in the waveguide.

The mask design is carried out by combining C++ code with L-edit for the purpose of reducing repetitive jobs and performing accurate layout design and generation.

For passive components fabrication procedures, all the lithography steps are carried out by the e-beam, thus ZEP520A photoresist is used and alignment markers and passive devices such as waveguide, grating couplers and tapers are etched at the same step in the ICP. After etching process, remaining ZEP520A is removed in the O_2 plasma asher. Diced chips are washed under acetone and then IPA in the ultrasonic bath and blown dry with N_2.

The fully etched waveguides with 500 nm height and 1.3 μm width had a propagation loss of 2.5 dB/cm the 3.8 μm wavelength. This is acceptable performance for the MIR.

Chapter 4

Mid-infrared waveguides and graphene

4.1 Introduction

This chapter describes the investigation of the performance of transferred graphene on top of the mid-infrared silicon waveguides which has been demonstrated in the previous chapter. The mask design, simulations, related fabrication, characterisation and results are presented.

There are three stages of such investigation. The first stage is the initial investigation that the graphene has been transferred directly on top of the silicon-on-insulator strip waveguides. Part of this work was a collaboration with Nikolaos Aspiotis from the University of Southampton. Nikolaos Aspiotis transferred graphene on top of the silicon waveguide, and I performed the graphene patterning process. The second stage of the work is a collaboration with a commercial company, Applied Nanolayers (ANL), where graphene is transferred and patterned by ANL based on my design after the silicon waveguides are fabricated by myself. The third stage of the project is a collaboration with Dr. Junjia Wang from the University of Cambridge. Same as the second stage, Dr. Junjia Wang carried out the graphene transferring and patterning processes after I fabricated the silicon waveguides. All characterisation has been performed by myself.

4.2 Graphene on silicon-on-insulator strip waveguides

This section demonstrates the initial investigation of the performance of graphene absorption after it has been transferred and patterned onto the SOI waveguides. The SOI strip waveguides are fabricated with the same method and with the same dimensions as those described in Chapter 3. First of all, the graphene transferring process that is adopted in the initial investigation stage is described here.

4.2.1 Design and simulation

By using the mask design mentioned before, a GDS design of the waveguides with increased lengths of graphene was created (Figure 4.1). Graphene length is increased by every 50 μm and a normalisation waveguide is also included.

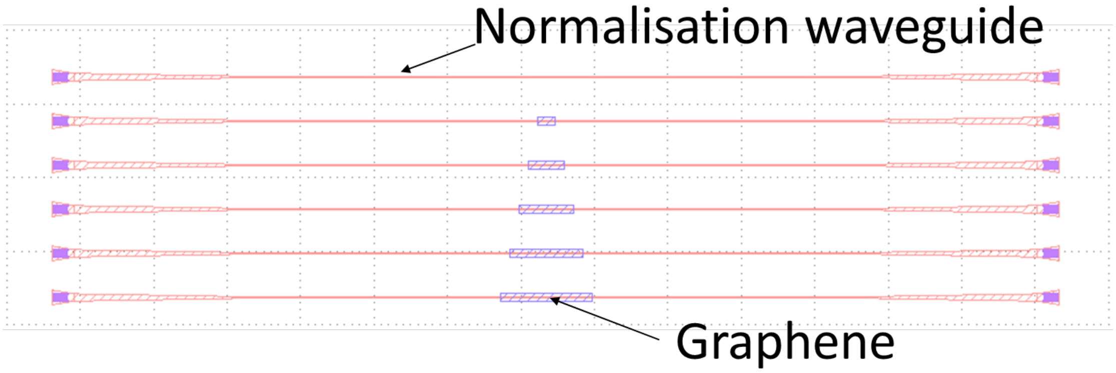

Figure 4.1: The mask design of the test structures for measuring the absorption coefficient when graphene is transferred onto the silicon waveguides.

Simulation of graphene coupled silicon waveguides is carried out in Lumerical MODE solutions, where a layer of graphene can be introduced using the surface conductivity material model [224]. The surface conductivity for a monolayer graphene is given by the combination of interband and intraband terms which are described in [225]. The surface conductivity material function is available in the material database in MODE solutions. Equation 4.1 and Equation 4.2 give expressions for surface conductivity,

$$\sigma_{intra} \approx \frac{-je^2 k_B T}{\pi H^2(\omega - j2\Gamma)}[\frac{\mu_c}{k_B T} + 2ln(e^{-\mu_c/(k_B T)}) + 1] \tag{4.1}$$

$$\sigma_{inter} \approx \frac{-je^2}{4\pi\hbar} ln(\frac{2\left|\mu_c\right| - (\omega - j2\Gamma)\hbar}{2\left|\mu_c\right| + (\omega - j2\Gamma)\hbar}) \tag{4.2}$$

where e is the electron charge, ω is the angular frequency, k_B is the Boltzmann constant, $\hbar$ is the reduced Plank constant, T is the temperature in Kelvin, τ is the electron relaxation time, and $\Gamma = 1/(2\tau)$ is the electron scattering rate. In this work, for the most common condition $T = 300K$ and $\tau = 1ps$. Chemical potential of graphene is constant (0.093 eV) under no external voltage [226], more information can be found in [227, 228]. Once an instance of graphene material type is added into the database, it can be assigned to a 2D rectangle. Figure 4.2 shows the simulated window of the waveguide coupled with graphene (marked white dash line). The simulated propagation loss of the waveguide is 315 dB/cm at 3.8 μm wavelength.

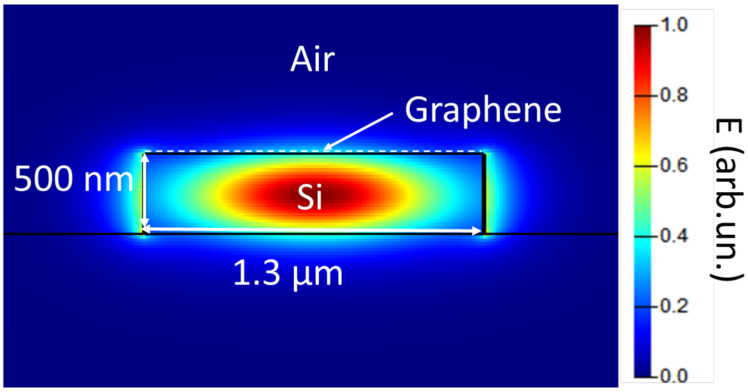

Figure 4.2: Cross-section of the graphene/Si waveguide.

4.2.2 Graphene transferring process

Because Cu has low solubility in C, graphene can be grown on Cu foils (Figure 4.3 (a)) and transferred to target substrates under the assistance of polymethyl-methacrylate (PMMA). The transfer procedure is briefly described below.

1. A PMMA layer is spun on graphene/copper film by a resist spinner, and then cured under 180°C for 1 minute. (Figure 4.3 (b))
2. The Cu is totally etched away inside the ammonium persulfate. (Figure 4.3 (c))
3. The dried graphene/PMMA film is placed on the silicon waveguide after being washed by the DI water. (Figure 4.3 (d) and Figure 4.3 (e))
4. The last step is to use acetone to dissolve the remaining PMMA above the graphene. (Figure 4.3 (f))

In order to examine the quality of graphene that has been transferred above the sample, Raman spectroscopy is used. Raman spectroscopy (Renishaw InVia Raman Spectrometer [230]) is widely used in lab- and mass-production scales for graphene examination, it offers high resolution and gives maximum structural and electronic information. Under laser excitation, the phonon energy shift in graphene can create scattering processes responsible for the graphene Raman peaks [231].

In pristine graphene, two main peaks in the Raman spectrum can be seen, G peak (1580 cm^{-1}) and 2D (or G') peak (2690 cm^{-1}). G peak represents primary in-plane vibrational mode, and 2D peak is a second-order overtone of another vibrational mode [232]. Disorder peaks will appear if the graphene shows defects, they are D (1350

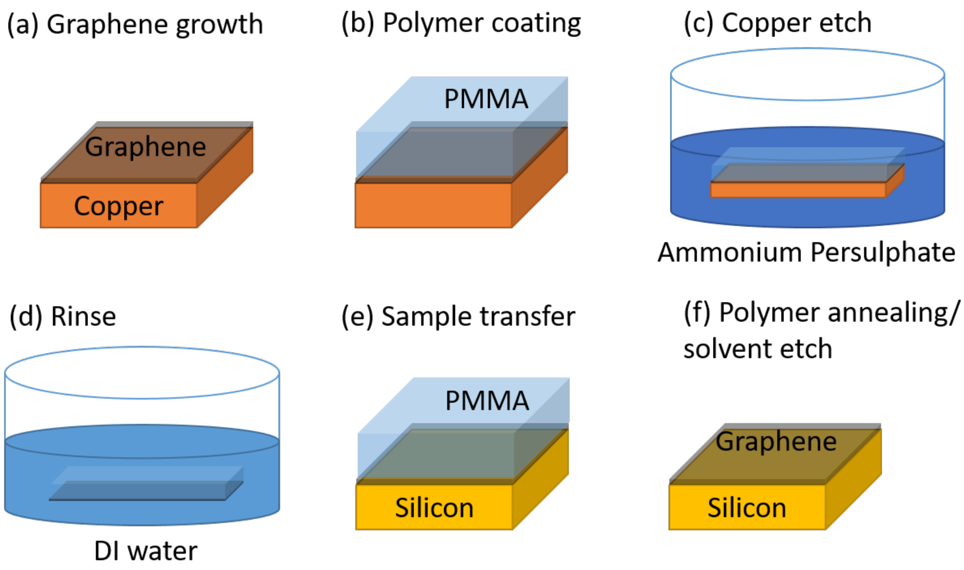

Figure 4.3: Process of graphene transfer, reproduced from [229].

cm^{-1}), D$'$ (1620 cm^{-1}) and D+G (2940 cm^{-1}). Disorder peaks cannot be seen in the pristine graphene [233]. Different disorder peaks are originated from different scattering processes within graphene, more information can be found in [231]. Figure 4.4 shows the Raman spectra (wavelength 633 nm) of pristine graphene and defect graphene [234].

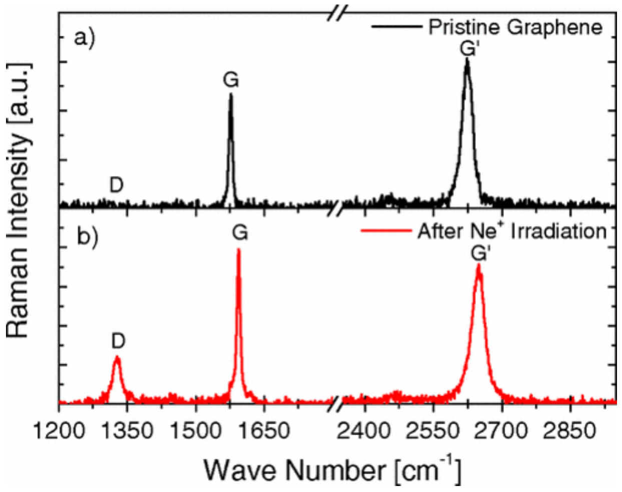

Figure 4.4: Raman spectra of (a) pristine graphene and (b) defect graphene after irradiation by Ne$^+$ at a dose of 10^{12}cm^{-2}, from [234].

Figure 4.5 shows the Raman spectrum of the un-patterned graphene transferred on the silicon waveguide. Only G and 2D peaks can be seen from the spectrum (wavelength 532 nm).

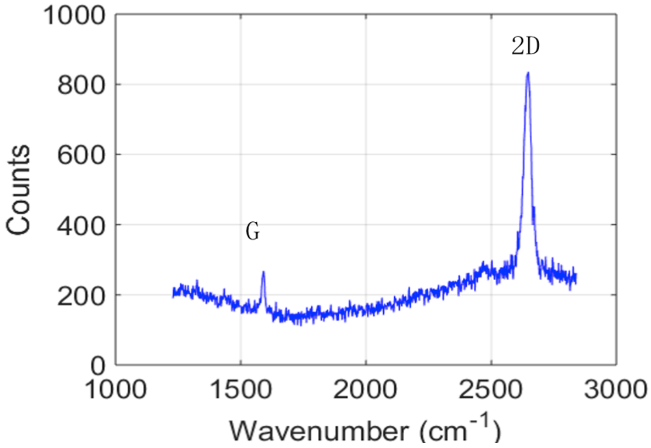

Figure 4.5: An example of a Raman spectrum of a SOI sample after graphene transfer. It can be seen that a good quality of single layer of graphene is achieved [235].

4.2.3 Graphene patterning

In order to examine the performance of graphene on top of the silicon waveguides, it is necessary to pattern the size and the position of graphene sheets on SOI accurately after transferring. At this stage, waveguides have already been patterned on the chip by myself and the graphene has been transferred by Nikolaos Aspiotis. The graphene patterning process is presented below and is carried out by myself.

- Sample preparation

  Before the sample is written by e-beam lithography, it is washed by acetone, IPA, DI water and blow dried by N_2. In order to remove moisture from the sample, it should be put in an oven at $210°C$ for at least 30 minutes before the spinning process.

- Electron-beam lithography

  AZ2070 photoresist is spun onto the wafer at a speed of 6000 rpm for 1 minute, which produces a photoresist layer of 2 micrometres thickness. Then the sample is baked for 1 minute at 110°C. E-spacer is spun on the just-baked AZ2070 surface at 2000 rpm for 100 seconds. The wafer is written in the same electron beam lithography tool. AZ2070 is a negative photoresist with high thermal stability and e-beam sensitivity. A negative photoresist is used as the majority of the area of the graphene is going to be etched away, so it saves time and is less expensive.

- Photoresist development

  Before photoresist development, e-spacer needs to be removed by DI water. Then the sample is baked for 1 minute at 110°C on a hotplate. Then AZ726 photoresist developer is applied to develop the sample after e-beam writing. The sample is placed in the developer for 3.5 minutes and then rinsed in DI water and blow dried under N_2. Figure 4.6 shows a microscope image of the sample after developing. It can be seen that AZ2070 patterning masks are formed for different structures after the developing. For the majority area not covered by photoresist, the graphene is going to be etched away in the subsequent etching step.

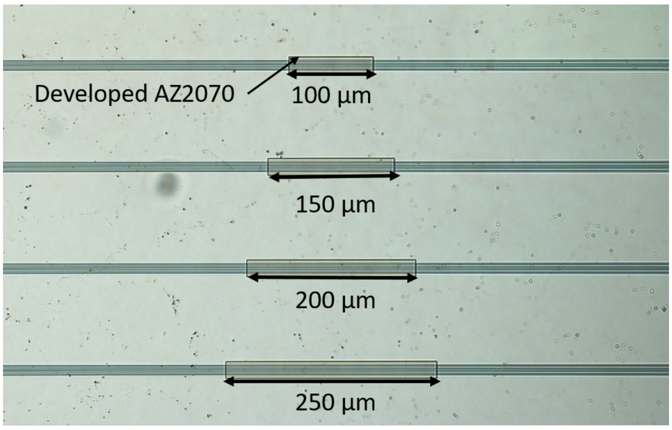

Figure 4.6: The optical microscope image of the straight waveguides covered by increasing length od graphene ribbons.

- RIE oxygen plasma etching

  The RIE oxygen plasma etching uses only oxygen (20 sccm), at a pressure of 100 mTorr and a power of 50 W for 1 minute (Figure 4.7) [236]. After the RIE oxygen etching, Raman spectroscopy is used to verify the presence of graphene. After etching, the remaining AZ2070 photoresist is stripped away by NMP solution. The stripping process involved putting the developing bowl on the heated hotplate at 80°C for 10 minutes.

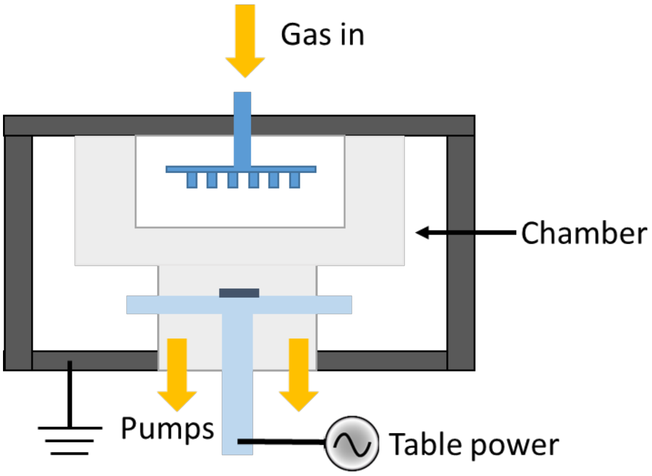

Figure 4.7: Diagram of the RIE chamber, reproduced from [236].

4.2.4 Optical behaviour of transferred graphene on silicon waveguides

By using the graphene transferring and patterning processes described above, CVD grown graphene is transferred and patterned onto the silicon-on-insulator waveguides for the purpose of investigating the performance of graphene/silicon waveguides. By using the characterisation setup described in Chapter 3 and the "cut-back" method. Figure 4.8 (a) shows the normalised transmission at 3800 nm wavelength, and (b) shows the normalised transmission at 3850 nm. The gradient of the fitted normalised transmission curve is the absorption coefficient of graphene for that wavelength. The absorption coefficients are 382 ± 0.5 dB/cm and 402 ± 0.6 dB/cm at 3800 nm and 3850 nm wavelengths, respectively.

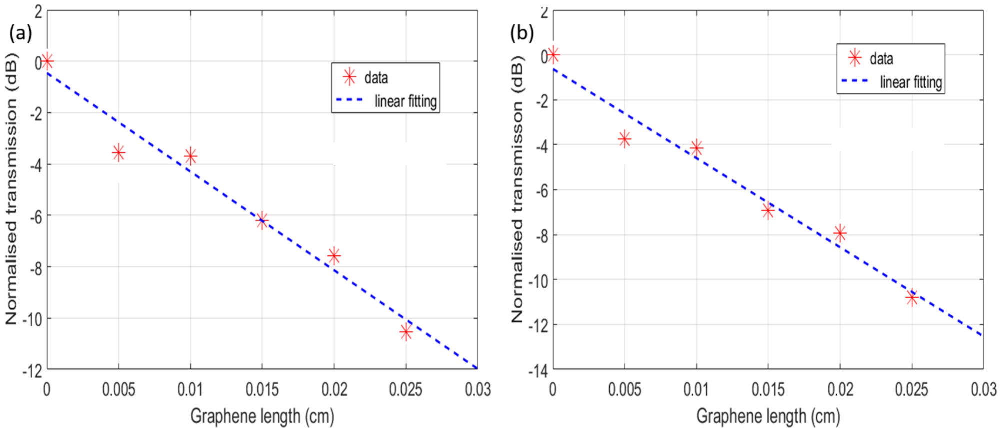

Figure 4.8: The normalised transmission of waveguides with increased lengths of graphene at (a) 3800 nm, and (b) 3850 nm.

Figure 4.9 shows the spectrum of the normalised propagation loss of the SOI strip waveguides with graphene on top. The propagation loss of is 382 ± 30 dB/cm over 3715-3880 nm wavelengths, where graphene is transferred and patterned on the SOI waveguides.

Figure 4.10 (a) shows an SEM (JEOL JSM 7500F FEG SEM [237]) of the graphene covered SOI waveguides, which confirms the graphene patterning process was successful. The designed size of graphene has been placed on the given position. Figure 4.10 (b) shows a magnified SEM image of graphene on a waveguide after processing, and residuals can be seen around the graphene sheets. Following the first attempt of transfer, more investigation was needed to determine the origin of the residuals. It was thought that they would be PMMA from the graphene transferring process or from the photoresist AZ2070 from the patterning process.

Figure 4.11 shows the Raman spectrum of the transferred and patterned graphene on top the silicon waveguides. Not only G and 2D peaks can be seen in the spectrum but

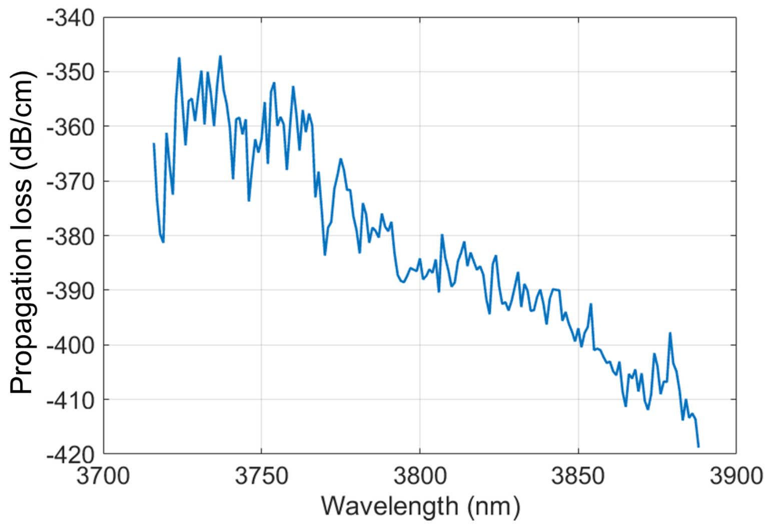

Figure 4.9: The normalised propagation loss of the SOI strip waveguides with graphene on top.

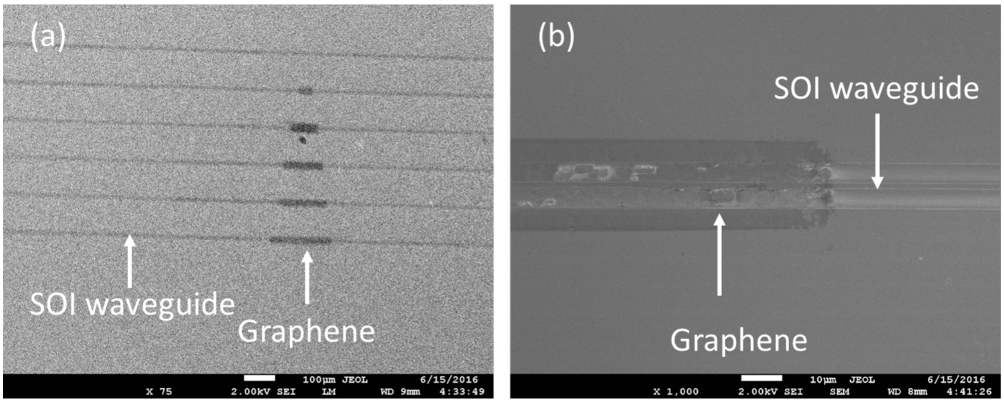

Figure 4.10: (a) SEM image of SOI waveguides covered by graphene, (b) magnified SEM image shows residuals left after processing, which may be the PMMA or AZ2070 from different processing steps.

also other defects peaks could be seen, which means that the graphene crystal lattice was broken after fabrication.

At this stage, the preliminary test of graphene transfer and patterning processes has been proved and next section is going to demonstrate the work in collaboration with a commerical company, Applied Nanolayers, on transferring graphene on silicon waveguides with a thin SiO_2 thick cladding.

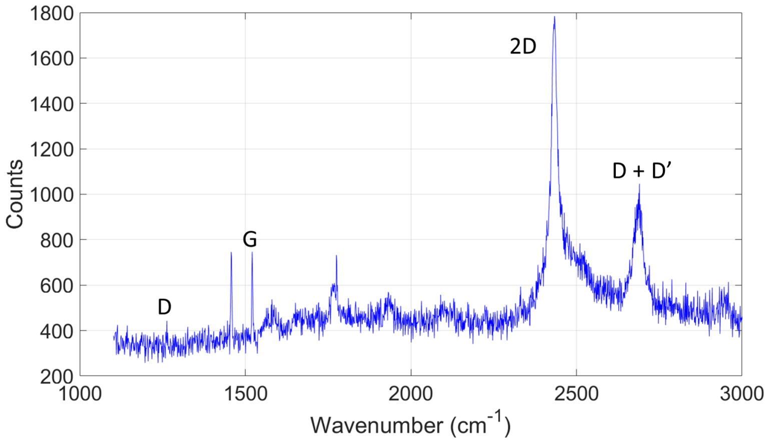

Figure 4.11: The Raman shits of graphene on SOI waveguides after transfer and patterning process.

4.3 Graphene on silicon waveguides with a thin SiO_2 top cladding

This section demonstrates the design, fabrication and characterisation of graphene on silicon waveguides with 90 nm SiO_2 top cladding. Graphene cannot be seen under an optical microscope after the AZ2070 is stripped after etching and developing, which makes the following fabrication processes more difficult. However, graphene can be seen under an optical microscope when a certain thickness of SiO_2 is deposited on the top silicon layer.

Part of this project has been carried out in collaboration with Applied Nanolayers (ANL), where graphene was transferred and patterned by ANL based on my design, and the experimental results were obtained at the University of Southampton by myself.

4.3.1 Design and simulation

Instead of fully etched 500 nm silicon to form the waveguide, there was a 50 nm slab region left, and then 90 nm SiO_2 has been deposited on top of the waveguides. This was done so that transferred graphene can be seen under the microscope on 90 nm SiO_2 [238]. Figure 4.12 shows the simulated cross-section of the 450 nm etch depth rib waveguides with a 90 nm PECVD SiO_2. The simulated waveguide propagation loss is 0.32 dB/cm at 3.8 μm wavelength.

By using the same simulation mode described before, Figure 4.13 shows the simulated cross-section when graphene is placed above the silicon rib waveguides with a 90 nm SiO_2 cladding. The simulated propagation loss of the waveguide after introducing the patterned graphene becomes 160 dB/cm at 3.8 μm. The white dash line represents the graphene layer.

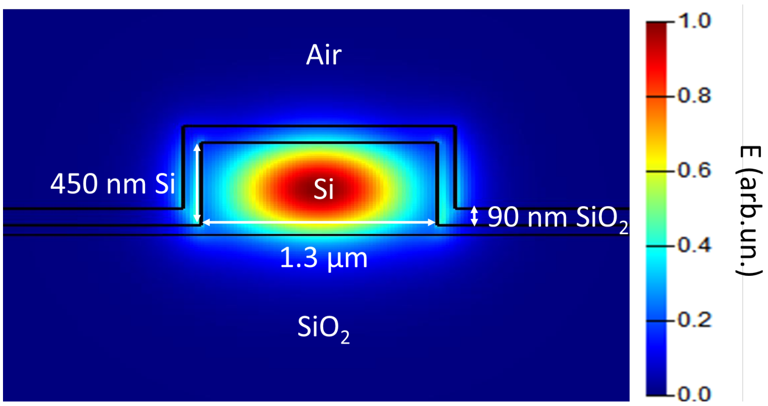

Figure 4.12: Diagram of the rib waveguide cross-section with simulated mode profile, light travelling in the perpendicular direction, with 1.3 μm waveguide width and 450nm depth and 90 nm SiO$_2$ on top.

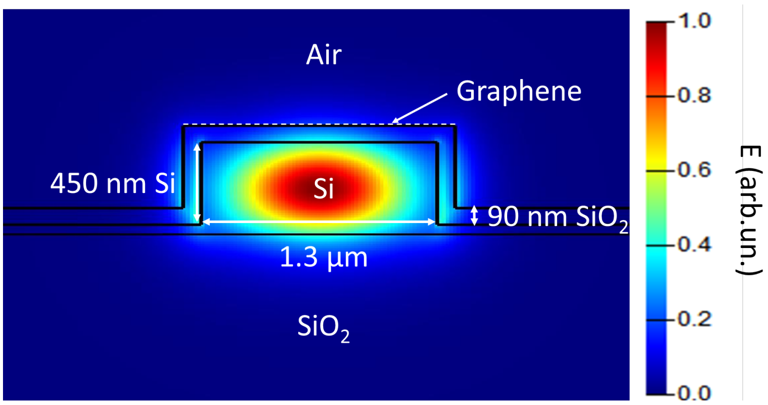

Figure 4.13: Diagram of cross-section of graphene placed on top of a rib waveguide with simulated mode profile.

By applying the same mask design method described in Chapter 3, the layout of graphene with silicon photonic waveguides is presented here. Straight waveguides with increased graphene coverage lengths were designed for the purpose of investigating absorption coefficients of graphene, which can be seen in the GDS design in Figure 4.14. The variation of the length of graphene embedded on the waveguides are from 100 - 600 μm, and in each section, the length of graphene is increased by 100 μm. Subwavelength gratings with tapers to couple light in and out of the waveguides are used. There are normalisation waveguides, and also two waveguides covered by 1000 μm long graphene sections are included.

4.3.2 Fabrication

Fabrication of the waveguides for ANL was carried out as described in Chapter 3. Figure 4.15 (a) shows the rib waveguides were formed in the ICP, Figure 4.15 (b) represents a 90 nm thick SiO$_2$ was deposited on top of the silicon waveguides by plasma enhanced

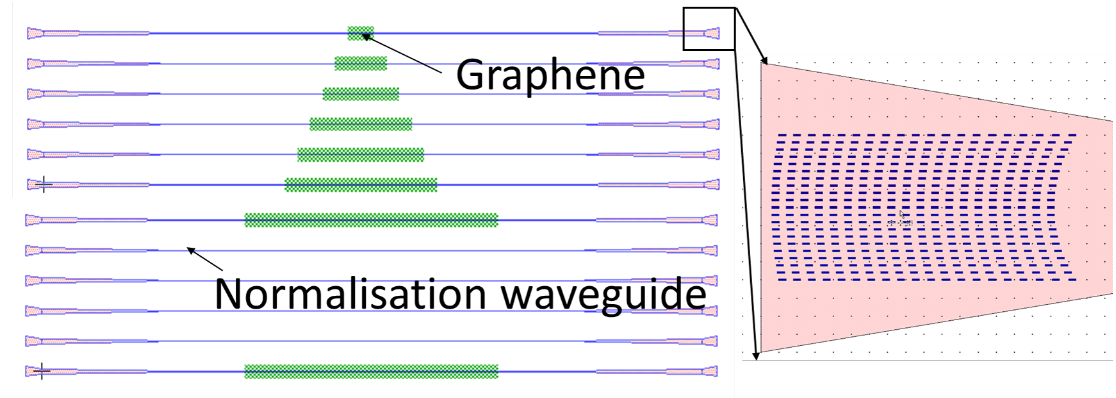

Figure 4.14: The mask design of the test structures for measuring the absorption coefficient when graphene is transferred onto the silicon waveguides. The inset represent the grating coupler design which remains the same.

chemical vapour deposition (PECVD) and Figure 4.15 (c) shows cross-section of the chip after graphene transfer and patterning.

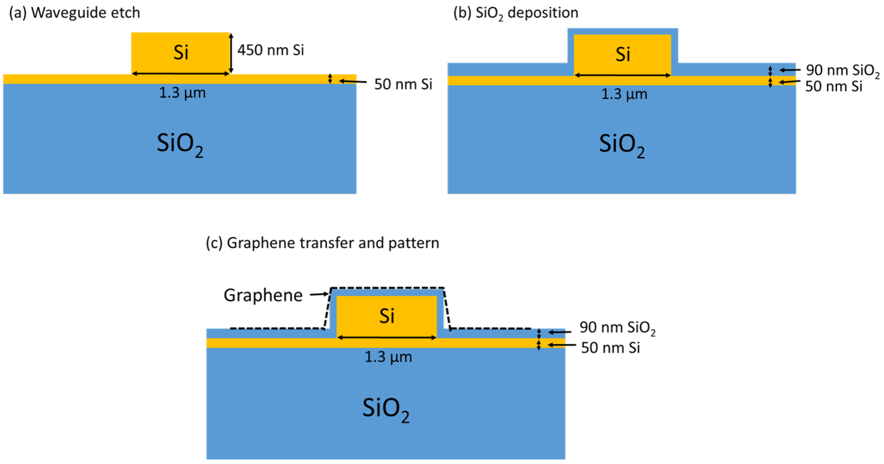

Figure 4.15: Schematic of the fabrication processes, (a) ICP etching to form the rib waveguides, (b) a 90 nm thick PECVD deposition on top of the silicon waveguides, (c) Graphene transfer and patterning.

Figure 4.16 shows the diagram of the reaction chamber [239]. SiO_2 layer is produced by chemical reaction: $SiH_4 + 2N_2O \rightarrow SiO_2 + 2N_2 + 2H_2$ that take place on the heated substrate (350○) in the chamber for the purpose of allow the generated gaseous by-products diffuse from the SiO_2 film during deposition.

4.3.3 Characterisation

The characterisation set up described previously has been used to measure the transmission of the test structures, Figure 4.17 shows the propagation loss of the silicon rib

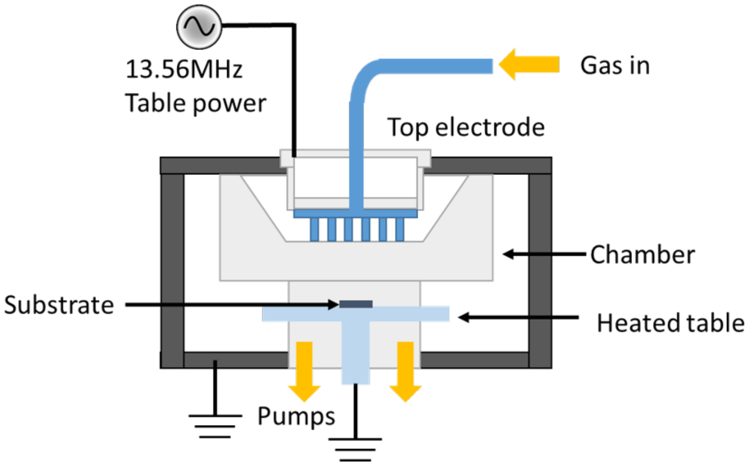

Figure 4.16: PECVD chamber diagram, modified from [239].

waveguides with 90 nm SiO_2 top cladding, which is 86 ± 11 dB/cm across the 3720-3888 nm wavelength range. Compared with the simulated 0.32 dB/cm propagation loss, the high waveguide propagation loss might come from the contamination during the graphene processing and metallisation procedure.

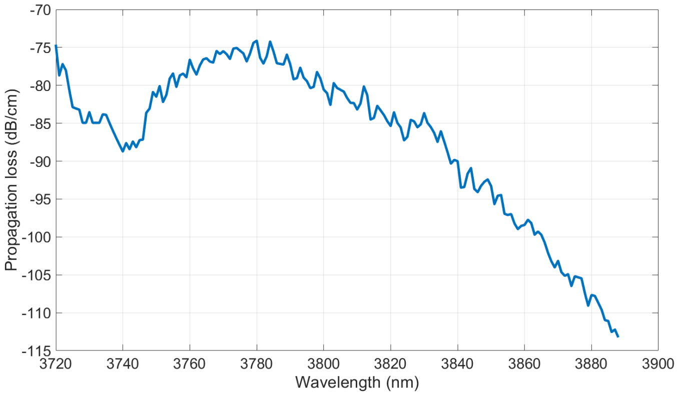

Figure 4.17: The propagation loss of the rib waveguides with top SiO_2 cladding from 3720-3888 nm wavelength.

Figure 4.18 shows the spectrum of the normalised waveguide propagation loss of the graphene/Si waveguides at the 3.8 μm wavelength, which is about 150 dB/cm . This value is close to the simulation value which is about 160 dB/cm (Figure 4.13).

Figure 4.19 shows the SEM image of the graphene on top of the waveguides after transfer and patterning, where a clearer sample surface can be seen. Compared to Figure 4.14, the graphene has been successfully fabricated as designed.

Zeiss NVision40 focused ion beam (FIB) system [240] is used to examine the silicon etch and SiO_2 deposition profiles. FIB instrument is almost identical to a SEM, but uses ion beams instead of electrons. The FIB can milling the specimen surface in nanometre precision through sputtering process. Zeiss NVision40 FIB system also contains a SEM

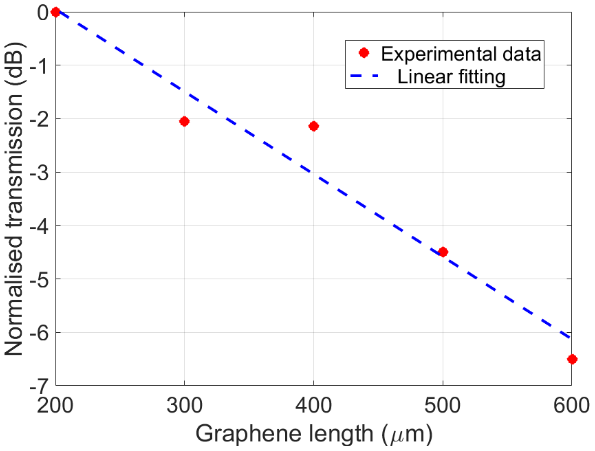

Figure 4.18: The normalised transmission of waveguides covered by increased length of graphene. The gradient of the linear fitting is the graphene absorption coefficient, which is about 150 dB/cm at 3.8 μm wavelength.

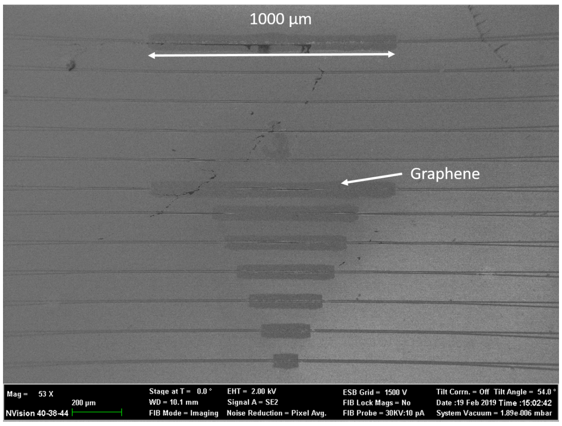

Figure 4.19: SEM image of the patterned graphene on silicon waveguides with 90 nm PECVD SiO_2.

system, where the electron and ion beams intersect at a 54° ar a coincident point near the sample surface, allowing immediate, high resolution SEM imaging of the FIB-milled surface, thus an cross-section image after FIB milling can be obtained.

Figure 4.20 shows the FIB image of the cross-section of a grating coupler, where it can be seen that the silicon has a height of 515 nm with a 47 nm rib, a 94 nm thick PECVD SiO_2 had been deposited on top of the gratings, hence the fabrication processes followed the design specifics. The waveguides have also been examined under the FIB and Figure 4.21 shows the cross-section of the waveguides, where a 62 nm slab has been formed with a thicknesses of 110 nm PECVD SiO_2 on the top of the rib and 89 nm SiO_2 deposited on the slab and side walls. In conclusion, the SEM images confirm that the fabricated dimensions matched the simulated ones.

Figure 4.22 shows the spectrum of the transferred graphene on waveguides with 90 nm SiO_2 after all the fabrication processes. G and 2D peaks can be seen in the spectrum

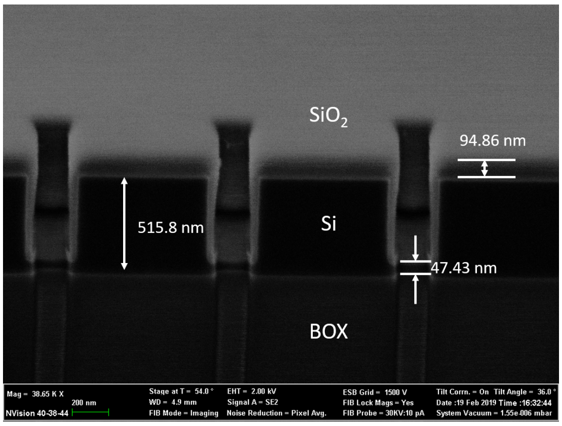

Figure 4.20: FIB image of the grating couplers of the photodetector.

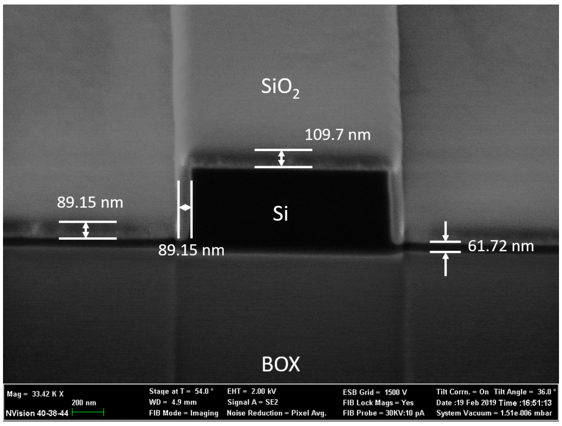

Figure 4.21: FIB image of the waveguide of the photodetector.

but also the defects peaks, which indicates that the single crystal lattice was damaged during the fabrication.

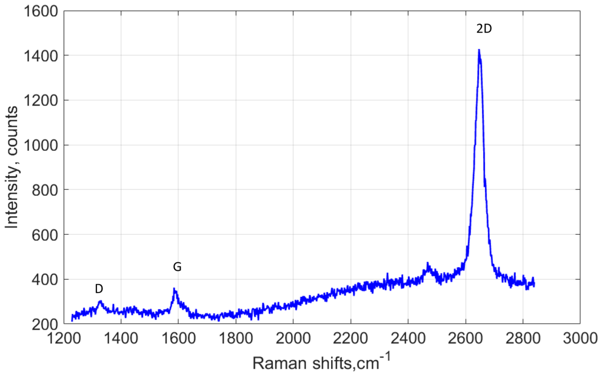

Figure 4.22: The Raman shifts of graphene on SOI after the patterning process and photoresist stripping. G and 2D peaks can be seen in the spectrum which confirms the single crystal lattice of graphene.

4.4 Graphene on the planarised Si waveguides

Learning from the SOI waveguide with 90 nm thick rib design, a planarised Si waveguide integrated graphene MIR photodetector was designed aimed at achieving better performance. Because the 3D structure created the potential of damaging graphene during patterning, a planarised surface was designed with advantage of reducing possibility of graphene breaking during fabrication.

This part of the work was carried out in collaboration with University of Cambridge, where all the passive devices fabrication was performed at the University of Southampton by myself, and the graphene transfer, pattern and metallisation procedures were carried out by Dr Junjia Wang in Cambridge based on my design. After the samples were fabricated, all the characterisation was carried out by myself. This section demonstrates the simulation, fabrication and characterisation of the passive devices, whilst the metallisation process is described in the next chapter.

4.4.1 Simulation and design

The dimensions of the waveguide have been narrowed down from 1.3 μm to 1 μm width and the etch depth changed to 500 nm, which would push the mode to the top and bottom sides of the waveguide thus the graphene-light interaction would be stronger than in the previous design. 500 nm etch depth is chosen due to it will be easier to control the etch depth. A thin and flat layer of chemical mechanical polishing (CMP) planarised SiO_2 has been designed on top of the silicon waveguide to create a flat surface for graphene transfer. Figure 4.23 shows the simulation of the 20 nm thick SiO_2 on top of the 1 μm wide fully etched SOI waveguide. The simulated propagation loss of CMP polished waveguide is 0.5 dB/cm at 3.8 μm wavelength.

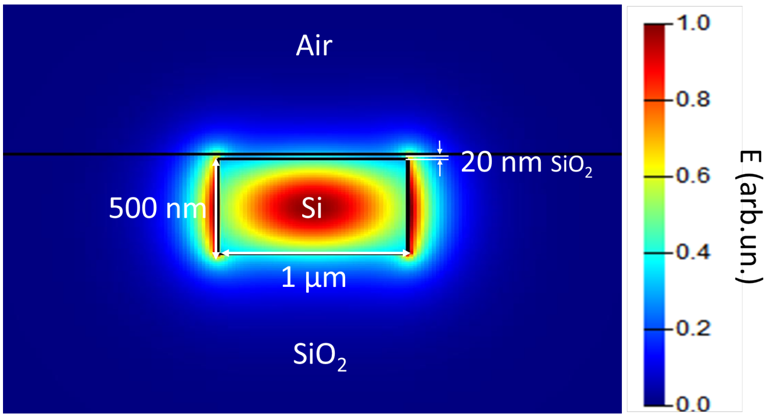

Figure 4.23: Diagram of the strip waveguide cross-section.

Figure 4.24 shows the mode profile within planarised waveguide with patterned graphene on top, the simulated propagation loss increased to about 320 dB/cm, the dash line represents the graphene.

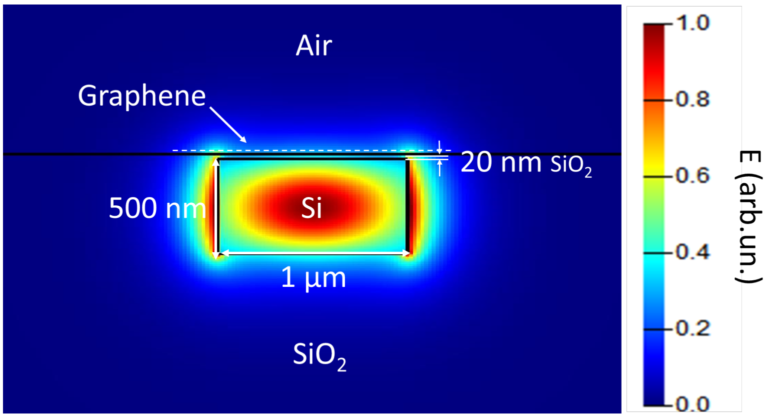

Figure 4.24: Diagram of the graphene Si strip waveguide.

Moreover, a directional coupler was introduced to split the light to make the optical alignment easier, in which 10% of light would be coupled into the reference arm for optical alignment and the rest of light would continue to the waveguide leading to the graphene photodetector. Directional couplers are made from two waveguides that are parallel and very close to each other, where the light is coupled from one waveguide into another through an evanescent field during propagation.

The directional coupler was simulated in MODE solutions, and the dimensions of the directional coupler were 17 μm in length and 400 nm gap between the two waveguides. Figure 4.25 shows the GDS design of the directional coupler normalisation structure where the length of 450 μm is exactly the length of one design of graphene photodetectors but without graphene and electrodes.

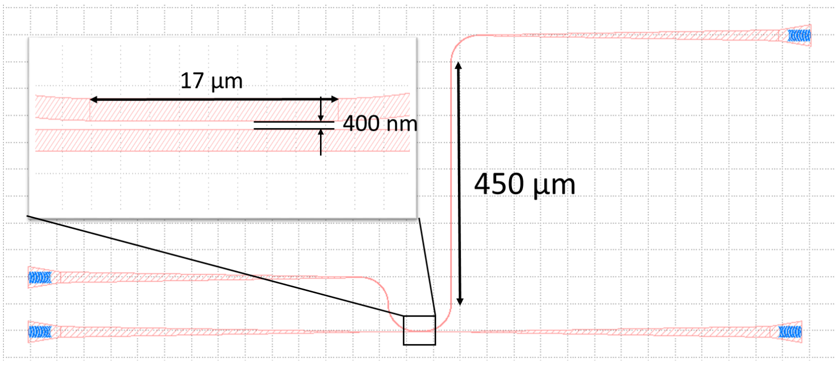

Figure 4.25: Diagram of the directional coupler normalisation structure, the inset shows the directional coupling region.

Figure 4.26 (a) shows the coupling ratio versus the coupling length of the directional coupler, where ~ 17 μm coupling length can result in 10% of light being coupled into the second waveguide, Figure 4.26 (b) shows the simulation result for a 400 nm gap between the two waveguides.

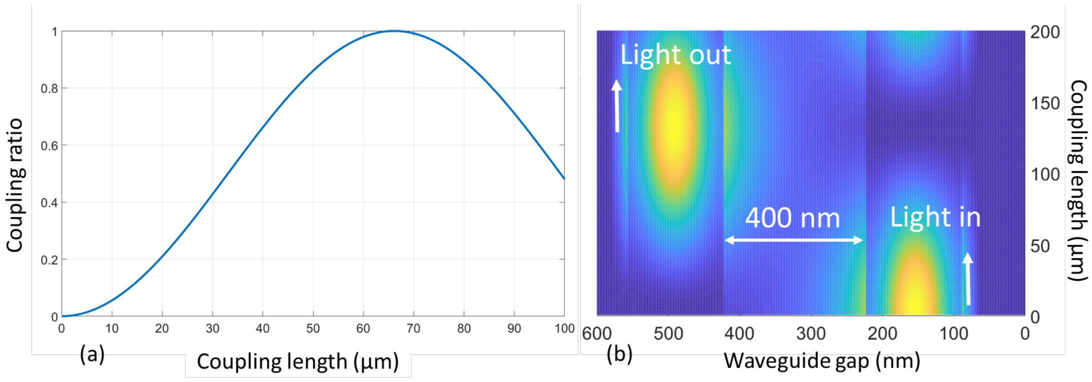

Figure 4.26: (a) The coupling ratio versus the coupling length of the designed directional coupler, (b) coupling between the two waveguides.

4.4.2 Fabrication

Fabrication of the waveguide layer of the device was carried out as described in Chapter 3. Following this the PECVD was used to deposit 1 μm thick SiO_2 on top of the wafer. Then, chemical mechanical polishing (CMP) was used to planarise the wafer surface in order to achieve a better graphene transfer quality. After CMP the wafer was cleaned in Fuming Nitric Acid (FNA) for 1 minute, and then the polished wafer was rinsed in DI water and blown dry under the N_2 gun. The dicing process has been already described in Chapter 3. Figure 4.27 shows the front view of the CMP system.

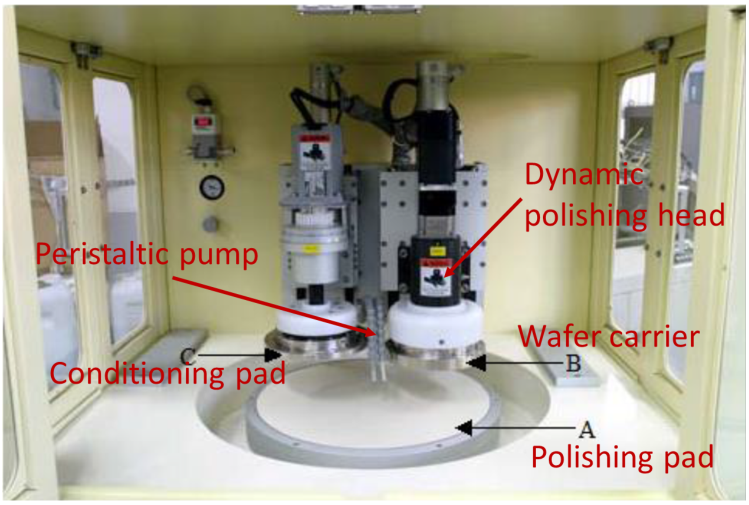

Figure 4.27: CMP system front view, reproduced from [241].

The CMP processes used an abrasive and corrosive chemical slurry (commonly a colloid) in conjunction with a polishing pad and retaining ring, always of a larger size than the size of the wafer being polished. The dynamic polishing head can rotate with multi-axis. This removes material and tends to even out potential irregular topography, making the wafer a planar surface [241]. The polishing procedures are illustrated below:

- Pre-polishing conditioning

  Pre-polishing conditioning consisted of a series of actions, where the polishing pad needed to be thoroughly wetted with DI water for 30 minutes, initially using the DI water gun to spray DI water onto the polishing pad, and then DI water was sprayed onto the polishing pad by the peristaltic pump for 10 minutes. The final step is to flow slurry onto the polishing pad for 5 minutes using the conditioning head.

- Wafer polishing

  After the polishing pad was correctly conditioned, the wafer polishing could take place. The wafer was stuck onto the wafer carrier and a wafer pressure of 75 g/cm^2 was applied on the wafer while polishing. Slurry was then pumped out from the peristaltic pump. Figure 4.28 shows the polishing process. During polishing the conditioning pad was up, and the wafer carrier head was down and rotating with the metal plate at the same time. Polishing was controlled within 10 minutes each time to achieve a uniform polishing profile. After each polishing, the thickness of the top SiO_2 was measured under the ellipsometry to calculate the polishing rate and determine the polishing time in the following.

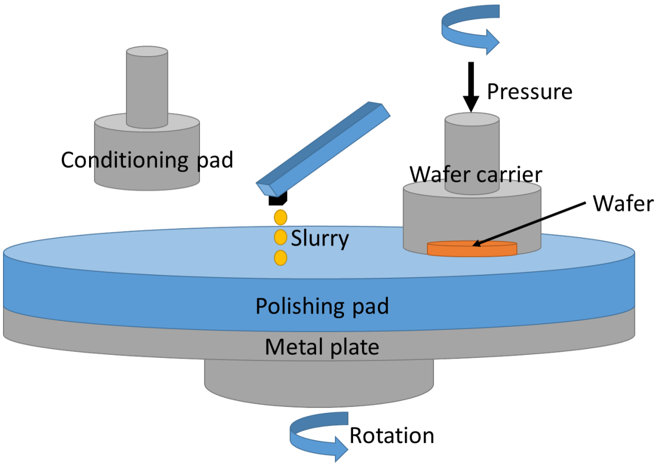

Figure 4.28: Diagram of CMP polishing.

- Post polishing and wafer cleaning

  After a CMP process, the polishing head and the polishing pad needed to be cleaned and the slurry dispense nozzle had to be cleaned by DI water to remove slurry residue left in the tube. Both heads were cleaned with a DI water gun and the polishing pad was rinsed thoroughly to remove slurry and particles produced

> during polishing. Finally, a lint free wipe was used to wipe the polishing pad, which was then blow dried by a N_2 gun.
>
> The polished wafer was dipped into FNA for 1 minute to remove any particles and slurry left on the wafer surface and then rinsed in DI water and dried by a N_2 gun.

After the wafers were polished and cleaned, next step was to dice the wafer into 15 mm × 20 mm sizes samples and then the diced samples were shipped to the University of Cambridge for the graphene transfer, patterning and electrodes metallisation. CVD grown graphene was transferred and patterned by using the same method described before.

4.4.3 Experimental results and analysis

By using the same characterisation setup and method mentioned before, unfortunately, due to the high propagation loss of the waveguides, it was not possible to measure a reliable photocurrent because the optical power entering the device was too small to measure, where the measured photocurrent was just above the noise floor. The measured propagation loss of the fabricated waveguides is shown in Figure 4.29. The propagation loss of the fabricated waveguides without patterned graphene was 168 ± 42 dB/cm. The grating coupler was measured to have a 27 dB loss at the 3.8 μm wavelength after calculation.

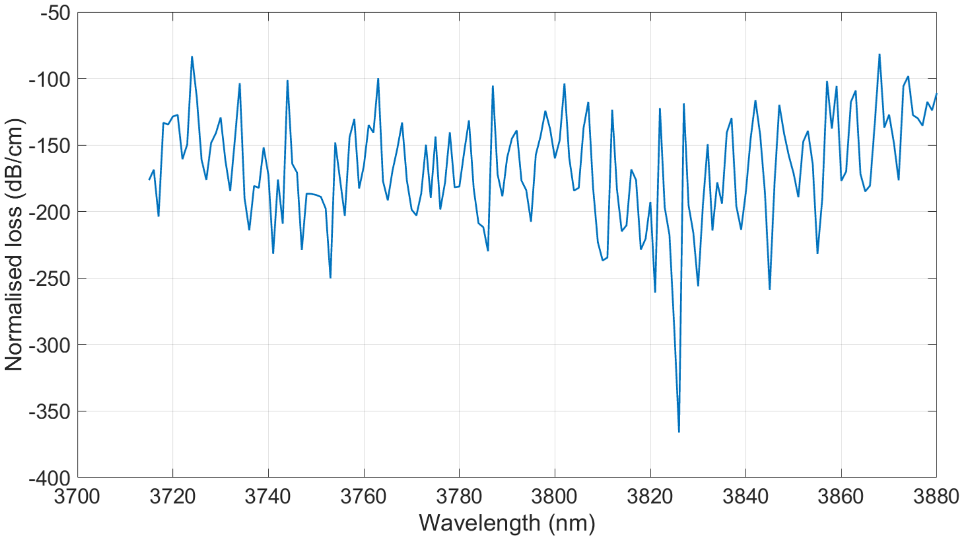

Figure 4.29: Normalised propagation loss of waveguides on the fabricated sample.

Compared with the simulated waveguide propagation loss value of 0.5 dB/cm, measured 168 ± 42 dB/cm is much higher. In order to investigate the origin of the high propagation loss and the high grating coupler loss, a diced sample from the same wafer as the fabricated waveguide, which did not go through the graphene transferring, patterning and metallisation processes was chosen for measurement of the propagation loss of the waveguides using the same characterisation setup.

- Propagation loss measurement of CMP polished waveguides

  First, the propagation loss of the waveguide after CMP polishing and normalised grating loss is shown in Figure 4.30.

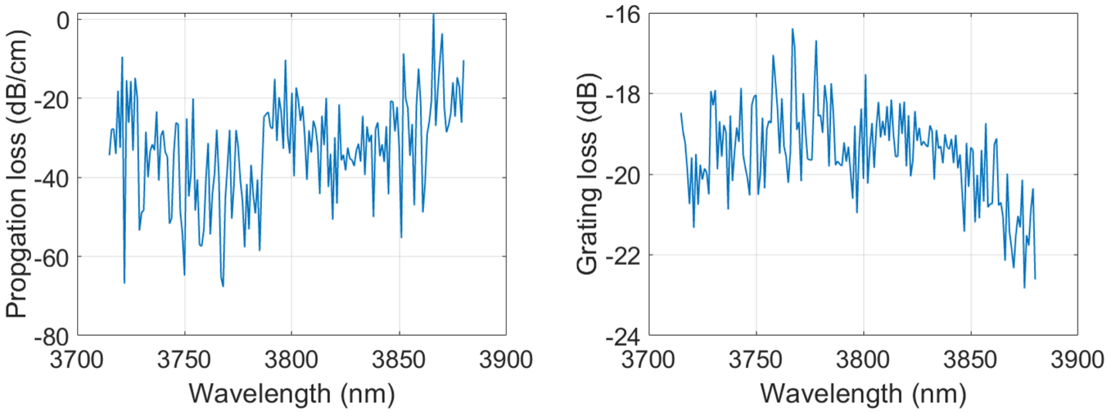

Figure 4.30: Normalised propagation loss of the waveguides after CMP and the grating coupler loss after CMP polishing.

  After the CMP, the propagation loss of the waveguides was 33 ± 13 dB/cm, and grating coupler loss was 20 ± 1 dB, which is a huge difference compared to the sample with transferred graphene indicating that a large part of the loss originated from the fabrication, such as PECVD deposition or CMP polishing.

  Moreover, 33 ± 13 dB/cm propagation loss was also very high, and that post-CMP fabrication also made it much higher. However, as CMP can be only performed on a wafer scale, the waveguide propagation loss cannot be determined before CMP polishing to compare the propagation loss values before and after CMP.

- Measurement after removal of the top SiO_2

  For the purpose of locating which steps contributed to the high loss, the sample was dipped into buffered HF (7:1) for 1 min to remove the polished CMP SiO_2 on top of the sample, and then the propagation loss and the grating coupler loss were remeasured. Figure 4.31 shows the propagation loss and grating loss after stripping the SiO_2.

  It can be seen that the propagation loss decreased from 33 ± 13 dB/cm to 11 ± 2 dB/cm, and the grating coupler loss decreased to 18 ± 0.5 dB. However, it was not possible to measure the waveguide and grating coupling losses after etching the waveguides, and before CMP because the CMP can be performed only on a

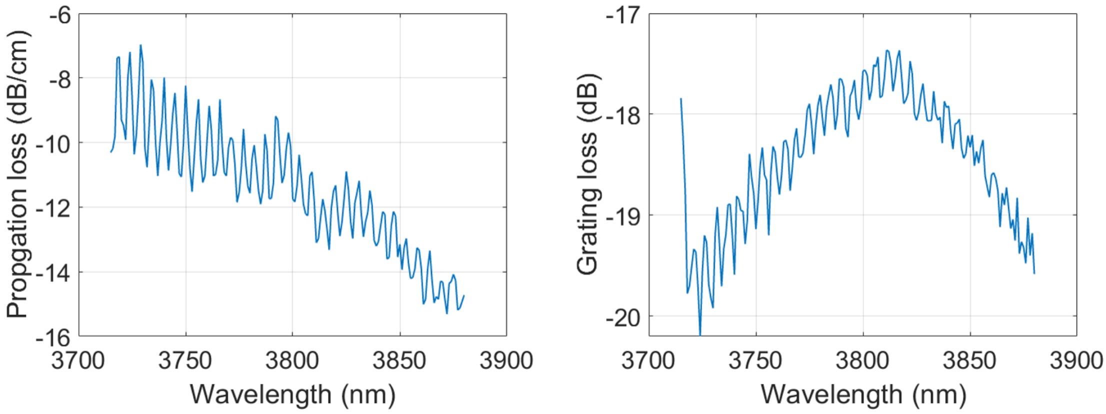

Figure 4.31: Normalised propagation loss of the waveguides and the grating coupler loss after CMP polishing and stripping polished SiO_2.

wafer scale. Thus based on the analysis so far, either the PECVD deposition of SiO_2 or the CMP polishing introduced much of the excess loss.

- Measurement after re-depositing 1 μm thick SiO_2

  In order to distinguish which step contributed more loss, 1 μm thick SiO_2 was deposited again by PECVD under the same deposition recipe, and the propagation loss of the waveguides and the grating coupler loss was measured again. Figure 4.32 shows the propagation loss of the waveguides and the grating loss after re-depositing 1 μm SiO_2 on the chip after the CMP polished SiO_2 had been removed in buffered HF.

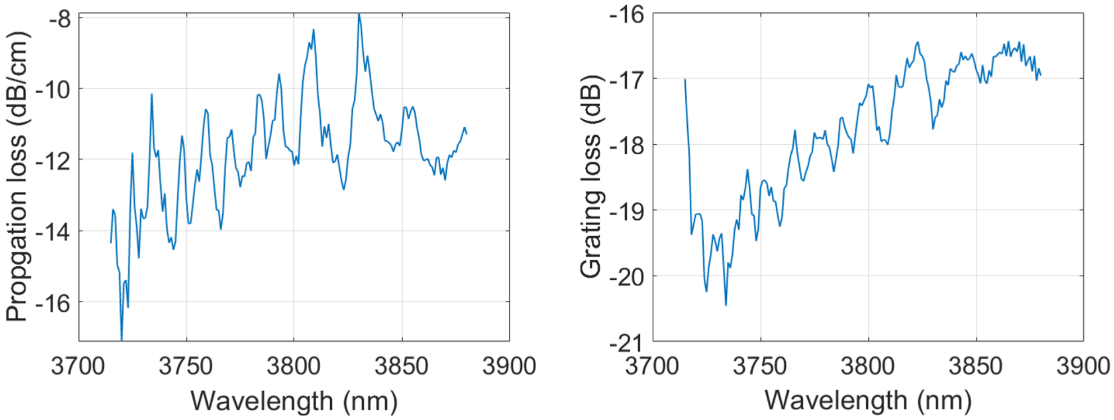

Figure 4.32: Normalised propagation loss of the waveguides and the grating coupler loss after re-depositing 1 μm SiO_2 on top of the chip.

The waveguides now had 12 ± 2 dB/cm propagation loss, while the grating coupler loss remained relatively unchanged compared to the results without top SiO_2, which was 18 ± 1 dB, it confirmed that the source of the high loss was mainly from the CMP process.

Figure 4.33 shows a SEM image of the top view of the grating coupler from a fabricated chip that was sent back from the University of Cambridge. The inset image shows that an non-uniform SiO_2 had been deposited into the subwavelength holes, which might be the reason the performance of the grating couplers was affected.

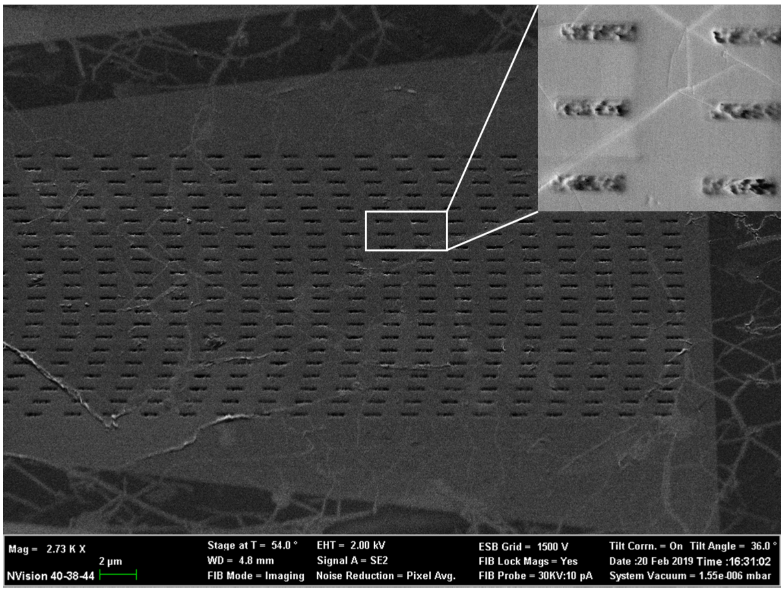

Figure 4.33: SEM image of a grating coupler from a fabricated chip, inset represents a magnified image of grating coupler holes.

Figure 4.34 shows a SEM image of the cross-section of the waveguides after polishing by CMP, and the height of the waveguide is only 317 nm, which means that roughly 180 nm Si was removed during the polishing. This is likely the cause of the high loss of the waveguide.

Simulations were performed for waveguides dimensions based on the SEM images (300 nm height and 1 μm width) with and without graphene predicted losses of more than 730 dB/cm and $\sim$ 8 dB/cm at the 3.8 μm wavelength, respectively. The CMP polished waveguide loss after stripping the SiO_2 was 11 $\pm$ 2 dB/cm, the result matched with the simulation value, additional losses might come from fabrication issues, such as residuals left during removing the SiO_2 during loss investigation that mentioned before. It was because the optical mode could not be well confined by the waveguide geometry after CMP polishing. The cross-section of the mode profile of graphene coupled with a CMP polished waveguide is shown in Figure 4.35. It could be concluded that due to the non-uniformity of polishing made during the CMP process, the damaged geometry of the waveguides caused a high waveguide loss, and the non-uniformity SiO_2 deposition caused the low performance of the grating couplers.

It should be also noted that loss could also come from the graphene transfer and patterning process, similar to the ANL case. The chamber contamination in Cambridge could have contributed to that.

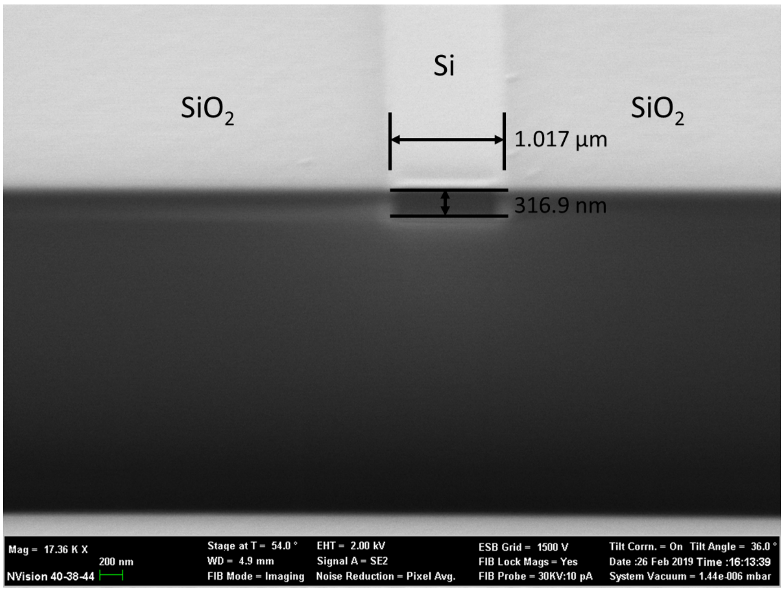

Figure 4.34: FIB image of the cross-section of the waveguide after CMP polishing.

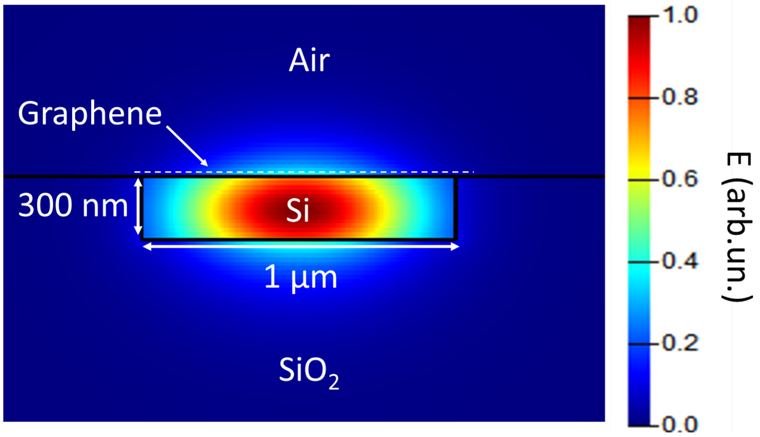

Figure 4.35: Diagram of the planarised waveguide after CMP process with dimensions of 300 nm height and 1 μm width.

Figure 4.36 shows a SEM image of a directional coupler after CMP polishing. A non-uniform PECVD SiO$_2$ deposition could be seen within the coupler gap, which affected the performance of the directional coupler. The fabrication error caused a large error in the waveguide propagation loss measurement due to the change of the waveguide dimensions and the effective indexes which made the results for the direction coupler to vary and be non-repeatable.

Figure 4.37 shows a Raman spectrum of the transferred graphene on planarised waveguides after all the fabrication processes. G and 2D peaks can be seen in the spectrum, and a small peak of D peak is also obtained.

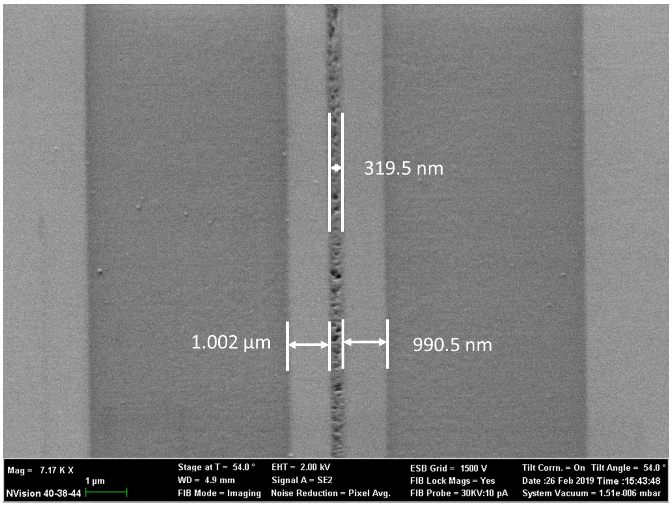

Figure 4.36: SEM image of the directional coupler after CMP.

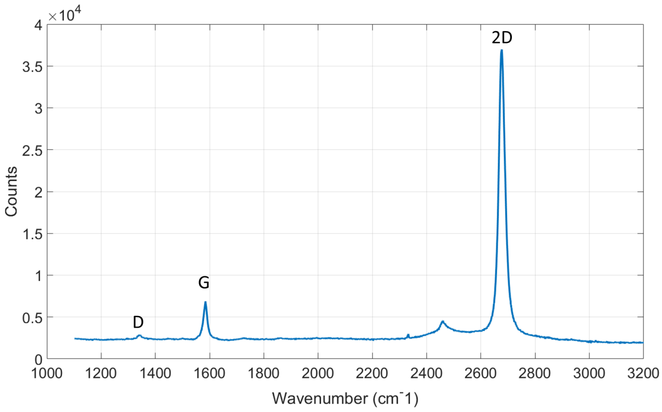

Figure 4.37: The Raman shifts of graphene on planarised silicon waveguides after transfer, patterning and metallisation processes.

4.5 Summary

This chapter describes the mid-infrared waveguides coupled with graphene. There are three stages of investigating the performance of mid-infrared waveguides with graphene: the preliminary stage that was carried out within the University of Southampton, whereas the other two stages were external collaborations.

In the preliminary stage, fabrication processes of graphene transferring and patterning processes were demonstrated. The graphene coupled silicon strip waveguides showed the propagation losses of 380 ± 30 dB/cm across 3715-3880 nm wavelength region. The residual problem was noticed after graphene transfer and patterning processes.

The second stage was a collaboration with a commercial company Applied Nanolayers. The geometry of the waveguide was modified to a 450 nm height rib waveguide instead of a fully etched 500 nm height strip waveguide and with a 90 nm thick SiO_2 top cladding, the reason for introducing the top cladding was that graphene can be optical seen under an optical microscope when graphene is placed on top of the 90 nm thick SiO_2. The propagation loss of the graphene/silicon rib waveguides with top cladding was about 150 dB/cm at 3.8 μm wavelength, which was close to the simulation value. However, the propagation loss itself was high which might came from the roughness and contamination created during fabrication. Moreover, based on the Raman spectrum, not only G and 2D peaks appeared, but also defect peaks can be noticed; this indicated that the transferring graphene on top of the non-planar geometry would break the graphene thus a fully planarised device geometry was performed in the next stage.

The third stage was a collaboration with the University of Cambridge. In order to prevent the graphene from breaking during fabrication, a planarised waveguide was designed with 20 nm CMP polished SiO_2 above the strip waveguide with 1 μm width and 500 nm height. Moreover, directional coupler was introduced for the purpose of improving the optical alignment. However, the propagation loss of the waveguide was very high and the performance of the directional couplers was unreliable. After a series of investigations, it was revealed that high loss was created from the uneven PECVD deposition and non-uniform CMP polishing profiles, but graphene transfer could have also contributed significantly. In order to reduce the high propagation loss during fabrication in the future, TEOS deposition is considered as it can perform a uniform SiO_2 deposition profile. For CMP polishing, adding dummy features to the mask design in order to create a more uniform density distribution surface can improve the polishing result.

The next chapter describes the design, fabrication and characterisation in terms of the graphene mid-infrared photodetectors based on graphene coupled with silicon waveguides from the stage two and three.

Chapter 5

Graphene mid-infrared photodetectors

5.1 Introduction

In this chapter, design, fabrication and measurement of waveguide integrated graphene MIR photodetectors are presented. Two different fabrication routes are demonstrated: graphene deposition on 3D structures and deposition on planarised surfaces.

5.2 Rib waveguide based graphene MIR photodetector

Following on from the previous chapter where graphene integration with MIR waveguides was presented, this section describes the design, fabrication and characterisation of the graphene MIR photodetector based on the SOI rib waveguides with 90 nm SiO_2 top cladding.

5.2.1 Photodetector design and fabrication

Asymmetrical electrodes were designed on the two sides of the waveguide. Figure 5.1 shows the GDS of the graphene photodetectors, where the graphene was placed and patterned on top of the 90 nm thick PECVD SiO_2 layer and electrodes were deposited on top of the graphene directly with separation of 3.5 μm and 5 μm. The grating couplers remained the same as those used previously.

Fabrication of the waveguide layer of the device was carried out as described in Chapter 3. Figure 5.2 shows the cross-section of the graphene photodetector with the same metal-graphene-metal configuration as in Figure 5.1.

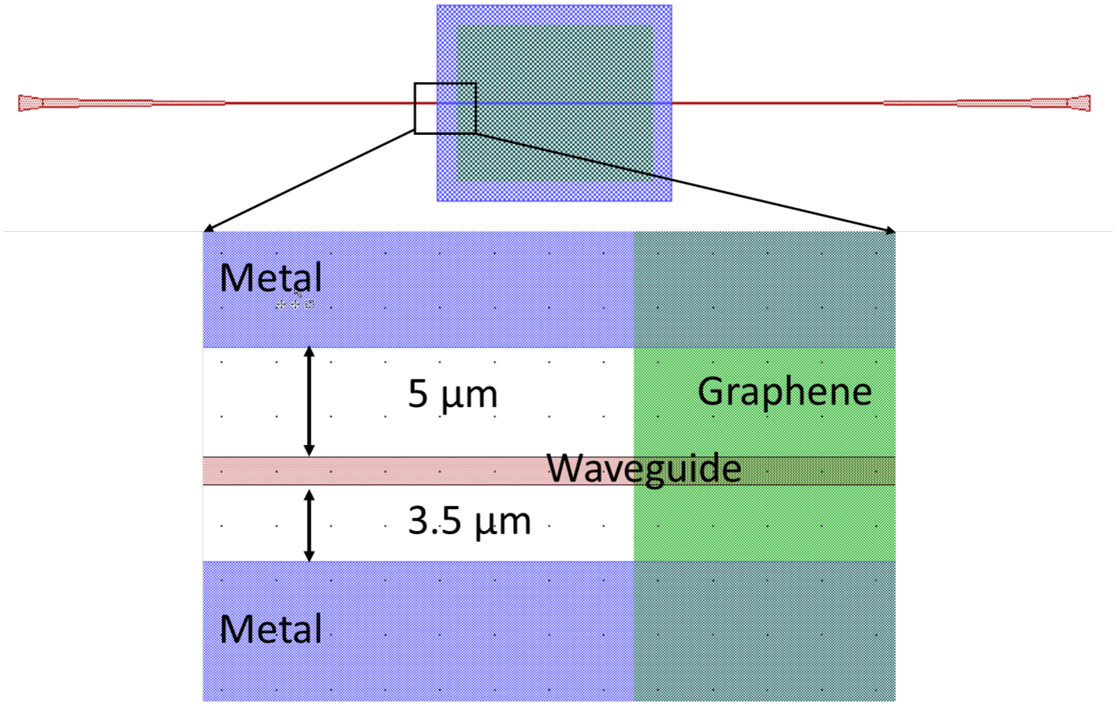

Figure 5.1: Design of the graphene photodetector, inset is the asymmetrical electrodes configuration.

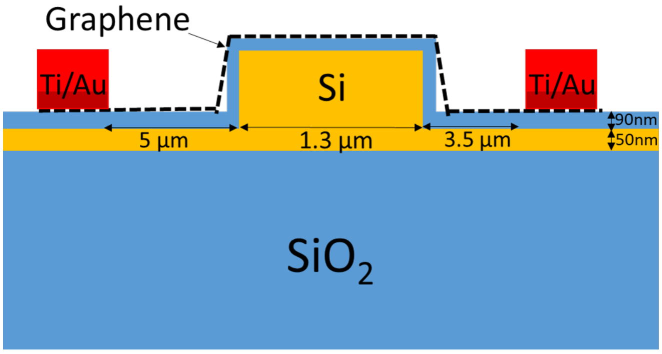

Figure 5.2: Schematic of the cross-section of SOI rib waveguide integrated graphene MIR detector.

Graphene transfer and pattern processes have been shown in Figure 4.3. The electrodes were fabricated by using the "lift-off" process, which is a widely used method for patterning structures on a target substrate surface. The"lift-off" process used in this project is described below and a diagram of the "lift-off" process is shown in Figure 5.3.

- Sample preparation

  Before the sample was written by e-beam lithography, it was put in an oven at 210°C for at least 30 minutes before spinning to remove the moisture on top of the sample.

- Resist spinning

The first layer of photoresist (MMA) was spun on top of the sample surface at 2000 rpm for 30 seconds and then baked on the hotplate at 150°C for 1 minute and 15 seconds. After the sample was cool down to room temperature, the second layer of photoresist (PMMA) was spun at 6000 rpm for 30 seconds, and baked at 180°C for 1 minute and 15 seconds. After that Espacer was spun on top of the sample surface to improve the conductivity of the sample.

- E-beam lithography and sample development

  After the sample was written in the e-beam lithography tool, the next step was to develop it. The developer was made from a 1:1 mixture of IPA and MIBK and the development time was 1 minutes. The developer was washed away by dipping the sample in the IPA for 30 seconds and then blow drying it with the N_2.

- Metal deposition and resist removal

  E-beam evaporator was used to deposit a uniform metal layer on the entire sample surface. Since the target material was deposited in the patterned area, the rest of the photoresist was washed out together with the metal deposited on top of the non-target areas, while the metal that was deposited in the target areas stayed. A stack of 10 nm Ti and 100 nm Au was chosen for the electrodes, where the 10 nm Ti acted as an adhesion layer between the planarised chip surface and Au. Au was chosen due to its excellent resistance to corrosion and oxidation among other metals.

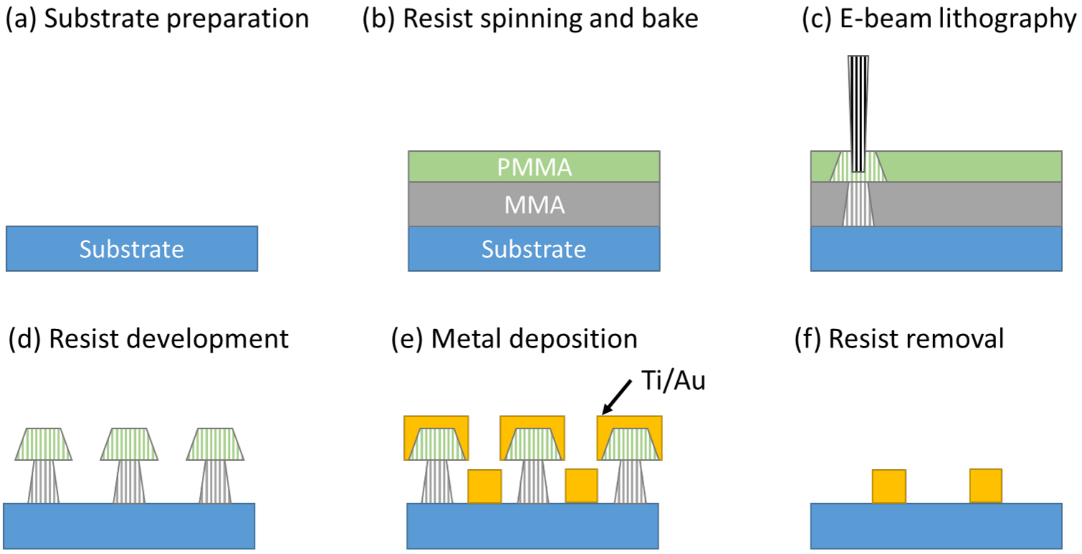

Figure 5.3: Diagram of the “lift-off” process.

5.2.2 Characterisation

In terms of optical measurements, the same equipment and experimental methods that have been described in Chapter 3 were used for the characterisation of the fabricated samples. Additional equipment was needed for the purpose of characterising the performance of the designed detectors by the application of a DC electrical signal for measuring the generated photocurrent. For DC measurements, two signal DC probes (Cascade Microtech) were applied to contact the electrodes. Each probe was held by one 3-axis stage at its base, which enabled accurate positioning. Figure 5.4 shows a schematic of how the optical fibres and electrical probes were aligned on the sample, where optical fibres were placed on the input and output grating couplers and electrical probes were on sides of the waveguides.

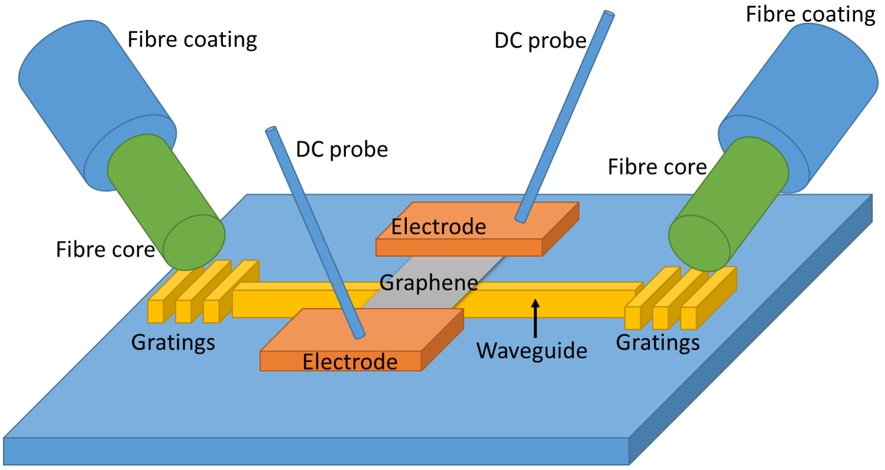

Figure 5.4: Schematic of used optical fibres and electrical probes to test the detector.

A vacuum pump (not shown Figure 5.4) was used and was connected to the sample stage which provided a vacuum force to the sample to prevent movement of the sample when lowering the electrical probes, that would otherwise affect the optical alignment. Furthermore, the probes were always lowered to make firm contact with the electrode pads on the sample before optical alignment.

For the DC measurement, the bias voltage was applied to the two electrodes. The generated photocurrent was measured by a picoammeter (Keithley 6487). The picoammeter was connected by a GPIB cable to the PC that also controlled the QCL laser controller and the lock-in amplifier, and a Python program was written for simultaneously controlling all equipment and experimental data being recorded automatically. Figure 5.5 shows a diagram of the setup.

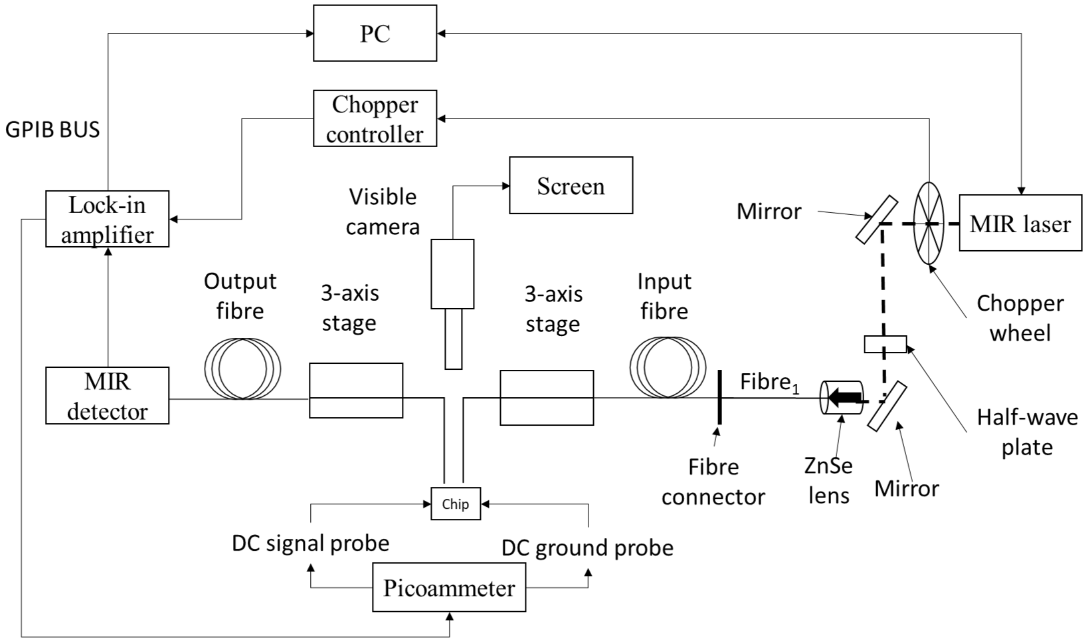

Figure 5.5: The diagram of DC measurement setup.

5.3 Experimental results and analysis

This section presents the results of the photocurrent measurements and of additional optical measurements that were required to calculate the input power to the detector, so that the photoresponsivity of the waveguide integrated graphene MIR photodetector at 3.8 μm wavelength could be calculated.

Both photodetectors used only supported reading out a relative optical transmission and could not read out the real power that came out of the graphene photodetector directly, therefore, before calculating the photoresponsivity of graphene photodetectors, loss measurements of all passive components including input and output fibres' losses were needed in order to calculate the actual optical power that goes into the graphene photodetector. A series of measurements for calculating the loss of each passive component and losses of coupling fibres were carried out.

- Input and output fibre loss measurement

  As shown in Figure 5.5, after light was coupled into the ZnSe lens, Fibre$_1$ and the input fibre (MIR Fibre$_{in}$) were connected through a fibre connector (ThorLabs, ADASTB2 [242]). A portable power meter [243] was used to read out the power reading from the end side of Fibre$_1$, where the patch cables of Fibre$_1$ was connected to the sensor of the power meter. All the data was recorded by Python code that communicated between the PC and the power meter through a USB cable. The power meter measured the whole spectrum from 3715 nm to 3880 nm and each reading recorded was the mean value of 50 measurements at each wavelength point. This method was kept the same for other measurements. Figure 5.6 shows a diagram of this step.

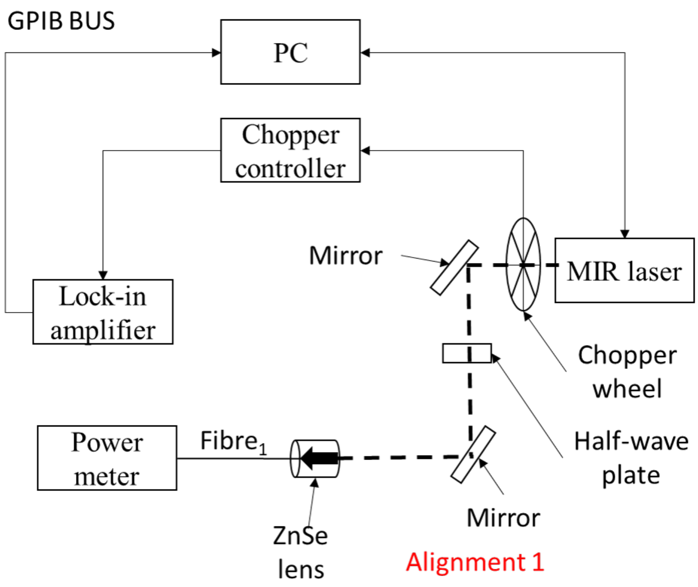

Figure 5.6: The diagram of measuring optical power at the end of Fibre$_1$

Once the optical power at the end of Fibre$_1$ was known, the power meter sensor was placed beneath the input fibre to calculate the loss of the input fibre, and multiple measurements were carried out. Figure 5.7 shows the measurement setup. Thus after measuring the optical power at the end of Fibre$_1$, the loss of the input fibre could be calculated. In terms of the output fibre, the same method has been applied. After calculation, each fibre had a 1.5 dB loss.

- Optical filter performance characterisation

  The power meter and both MIR detectors (VIGO and InfraRed) had their limitations, such as that the power meter could directly read out the optical power but had a high noise floor ($\sim$ 0.2 mW), whereas the MIR detectors were much more sensitive, but had maximum input power that were below the power meter noise floor. Thus two optical neutral density filters were used during measurement to filter out some optical power and reduce the power level to the range where the MIR detectors could work. Two spectral filters were labelled as NDIR03A and NDIR20A [244] (3dB and 20 dB attenuation respectively) which could be screwed together to make a 23 dB filter. However, because there were back reflections within the cavity between the two filters, the real performance of the filter needed to be tested. Figure 5.8 shows the diagram of the filter performance measurement.

  First, the optical power was reduced by slightly misaligning the coupling between the laser and the ZnSe lens, and then applying the filter in front of the ZnSe lens and repeating the same scan, thus the performance of the filter can be calculated

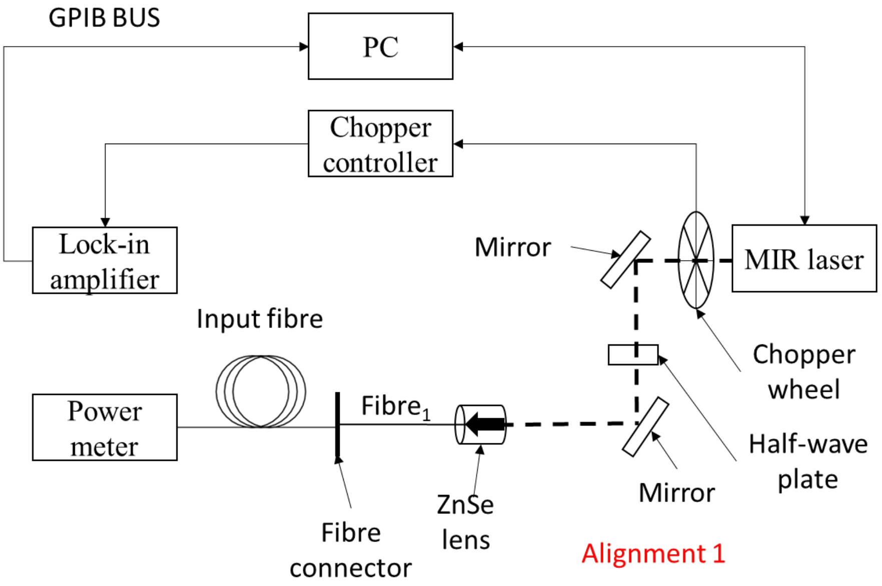

Figure 5.7: Schematic of the setup used for measuring the optical power at the end of the input fibre, for the purpose of calculating the input fibre loss.

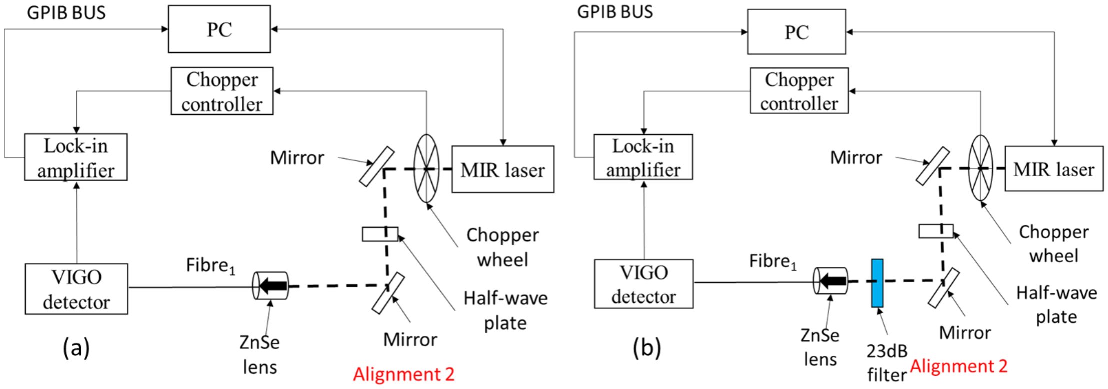

Figure 5.8: The diagram of measuring the filter performance, (a) measurement without filter, (b) measurement with filter.

based on the two measurements. Both measurements were connected by the GPIB bus and automatically recorded by the LabView program in the same way as the propagation loss measurement.

- The conversion between VIGO detector and power meter

  With the filter applied, and the out-port of Fibre$_1$ connected to the VIGO detector, the third alignment was needed to make sure that the VIGO detector reached its peak value, and then switched the out-port of Fibre$_1$ to the sensor of the power meter and removed the 23 dB filter. Combining these two sets of data with the performance of the filter, the conversion between the transmission and optical power can be calculated. Figure 5.9 (a) shows schematic of the measurement using the VIGO detector with the filter, and Figure 5.9 (b) represents a schematic of applying the power meter to record the real optical power.

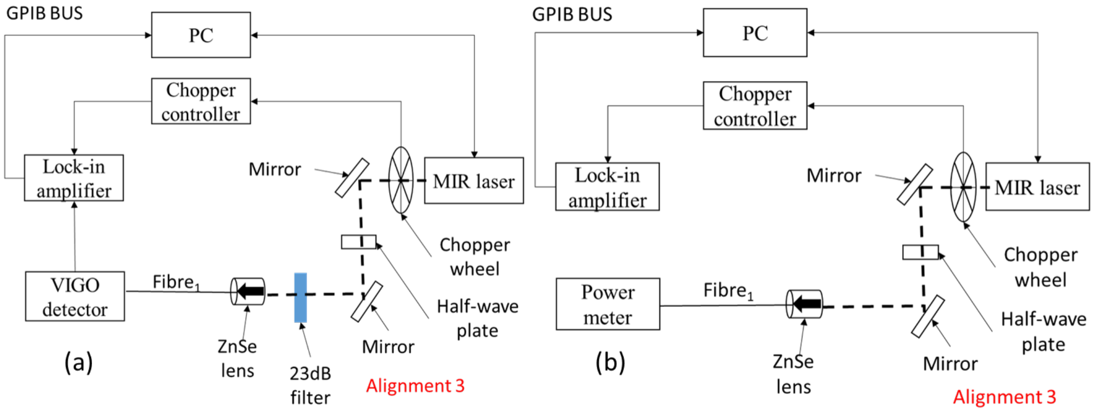

Figure 5.9: Schematics of measuring the relationship between readings of the VIGO detector and the optical powermeter, (a) using VIGO detector with the filter, and (b) applying power meter to record the real optical power.

- The relationship between the VIGO detector and the InfraRed detector

  VIGO detector has a larger bandwidth ($>$ 400 MHz) while the InfraRed detector has a higher detectivity, thus InfraRed was used to measure the photocurrent. Once the relationship between the VIGO detector and optical powermeter was known, it was possible to find out the relation between readings from the InfraRed detector and the optical powermeter.

  Figure 5.10 (a) shows that first the screws on both mirrors were tuned to let the lock-in amplifier shows a peak value, and then Figure 5.10 (b) with the same alignment the outport of Fibre$_1$ was switched from the InfraRed detector to the VIGO detector and another scan was recorded. Based on the data measured from these steps and the relation between the VIGO detector and the powermeter, the final relation between the InfraRed detector and the optical power value could be calculated.

Following all the measurements described above, Figure 5.11 shows the sensitivity of the InfraRed detector, showing the reading recorded from the lock-in amplifier versus the real optical power goes into the InfraRed detector. For example, at 3800 nm, 1.5 mV reading from the lock-in amplifier represents 1 nW of optical power coupled into the InfraRed detector.

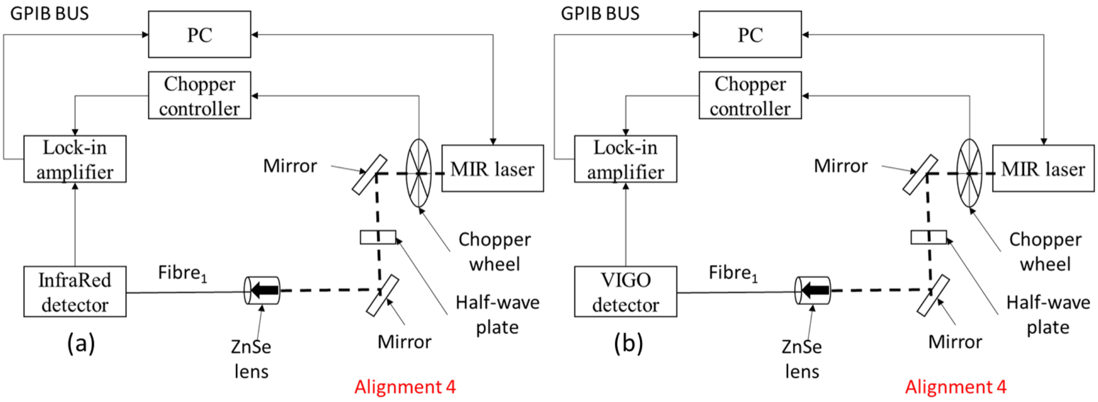

Figure 5.10: Schematics of measuring relation between readings of the VIGO and InfraRed detectors.

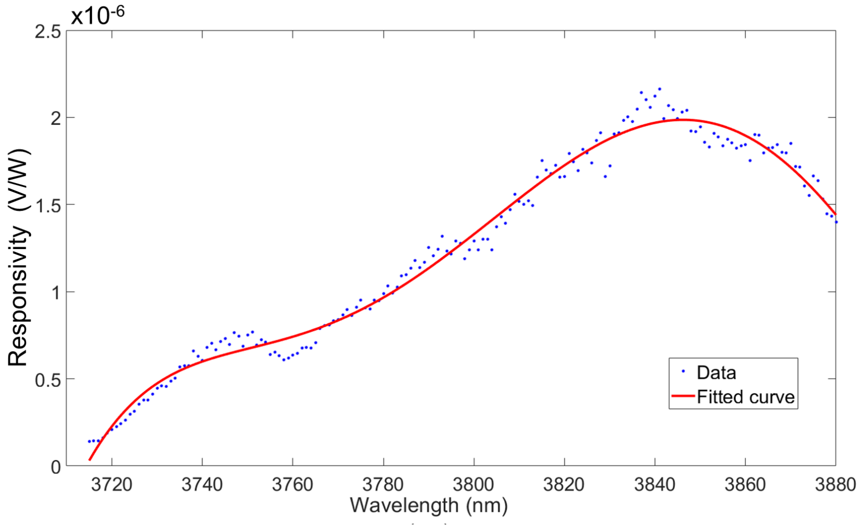

Figure 5.11: The sensitivity of the InfraRed detector.

5.3.1 Experimental results

The photocurrent is shown in Figure 5.12 as a function of increased optical power that was coupled into the graphene photodetector. The gradient of the linear fitting gives the photoresponsivity of the device at 3.8 μm under -1 V bias voltage of 2.2 mA/W.

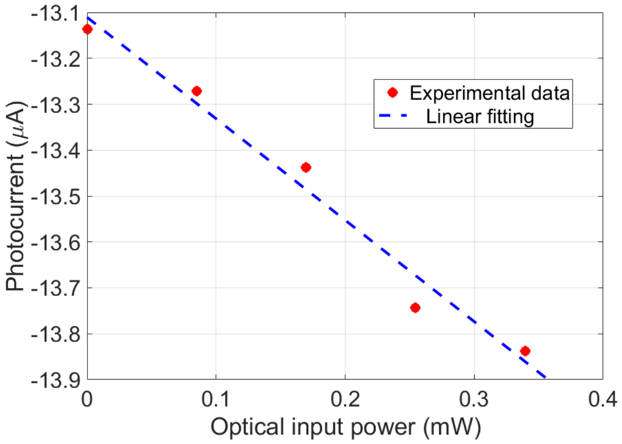

Figure 5.12: Photocurrent as a function of increased optical power that was coupled into the detector.

Figure 5.13 shows the normalised photoresponsivity versus bias voltage of the graphene photodetector at 3.8 μm wavelength. It can be seen that the trend is linear for the input optical power used.

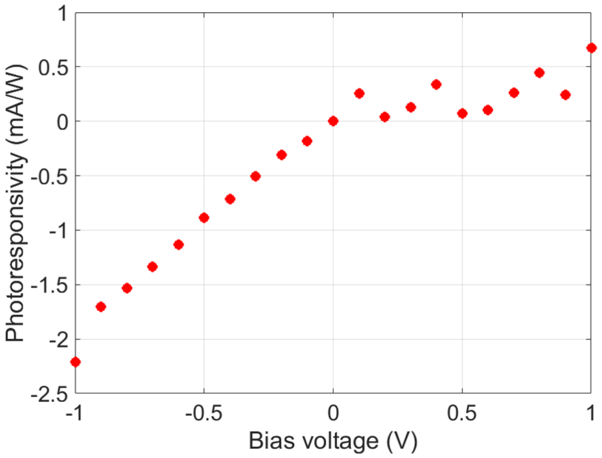

Figure 5.13: Photocurrent versus bias voltage applied to the graphene photodetector.

Figure 5.14 shows the dark current versus DC voltage of the same device. The dark current and bias voltage shows a linear relationship, where at -1 V the dark current was around -13 μA.

Figure 5.15 shows a SEM image of the cross-section of the graphene MIR photodetector, where a 571 nm height waveguide with 3.7 μm and 1.5 μm electrodes separation confirmed the success of the fabrication.

The signal was just above dark current because of high waveguide loss, which reduced the performance of the device. Compared with another waveguide integrated graphene

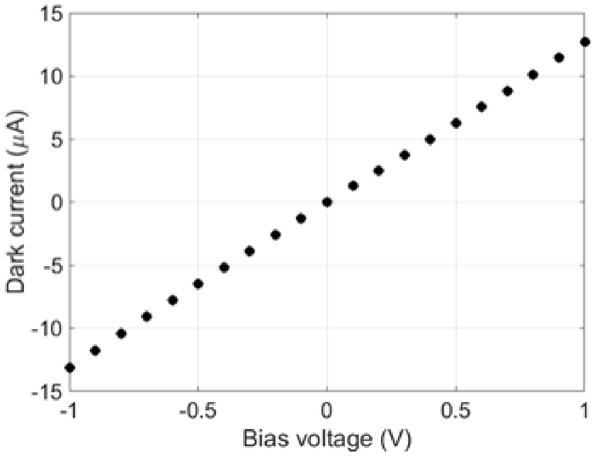

Figure 5.14: Diagram of dark current versus bias voltage.

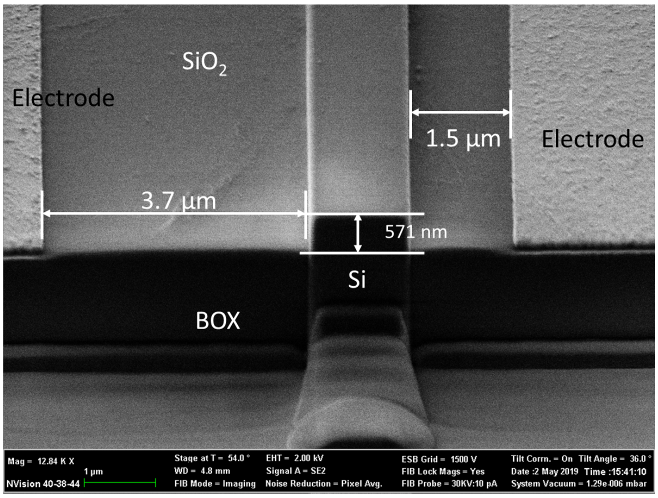

Figure 5.15: SEM image of the cross-section of the metal-graphene-metal junction.

photodetector, a higher extrinsic responsivity of 16 mA/W with 41 GHz bandwidth at 1550 nm wavelength was published in [195], instead of using SiO$_2$, 25 nm thick hydrogen silsesquioxane (HSQ) was coated on top of the waveguide.

Apart from the high waveguide loss, another contribution to low responsivity was the 3D rib structure where graphene was transferred onto and after a series of plasma etching and metallisation processes, graphene sheets showed defects from in Raman spectrum. Therefore, creating a flat surface for graphene transfer could reduce defects of the graphene during fabrication. A planarised silicon waveguide integrated graphene photodetector is described in the following section.

5.4 Planarised Si waveguide integrated graphene photodetector

As the 3D structure created potential damage of graphene during patterning, a planarised surface was designed with advantage of maintaining graphene without breaking during fabrication and enhancing the graphene-light interaction.

This part of the work was a collaboration with the University of Cambridge, where all the passive work has been done in the University of Southampton by myself, and the graphene transfer, pattern and metallisation procedures were carried out by Dr Junjia Wang at Cambridge based on my design. After the samples were fabricated, all the characterisations were carried out by myself at the University of Southampton.

5.4.1 Design and fabrication

Figure 5.16 (a) shows the design file of one graphene photodetector with an asymmetrical electrodes configuration as in the previous design. Figure 5.16 (b) shows the dimensions of asymmetrical electrodes.

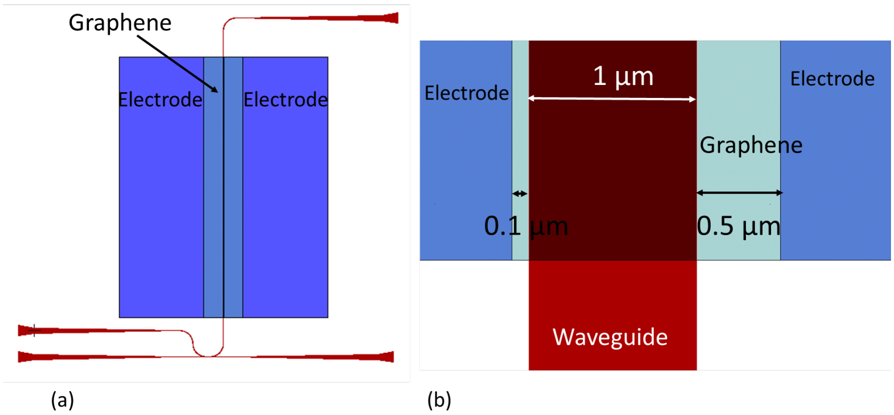

Figure 5.16: (a) Diagram of the design of the graphene MIR photodetector; (b) shows the dimension of asymmetrical electrodes.

Figure 5.17 shows the cross-section of a graphene MIR photodetector with the same asymmetrical electrodes design and a planar 20 nm thick SiO_2 top layer made by using the chemical mechanical polishing. Dr Junjia Wang performed the metallisation by using the “lift-off” process based on my design.

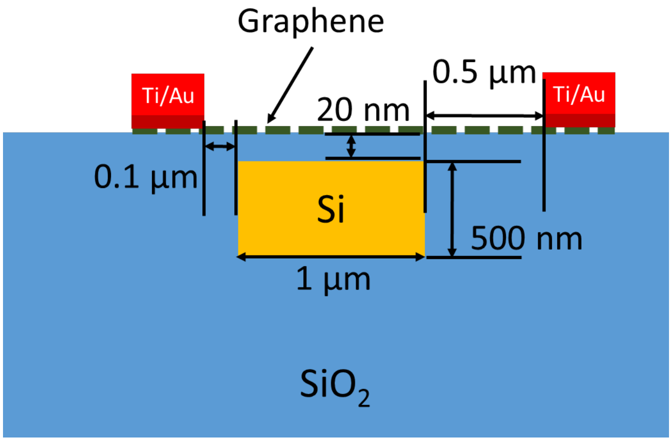

Figure 5.17: Diagram of a cross-section of a strip waveguide integrated graphene MIR photodetector.

5.5 Coupling light from the out of plane direction

By using the same characterisation setup and method mentioned before, unfortunately, due to the high propagation loss of the waveguides of ∼ 170 dB/cm (see Chapter 4 section 4.4.3), it was not possible to measure a reliable photocurrent as the laser power coupled into the device was too small to measure, and the measured photocurrent was just above the noise floor.

Figure 5.18 shows an SEM image of the cross-section of the graphene MIR photodetector, where a flat surface can be seen beneath the deposited electrodes with thickness of 106 nm. The waveguide width is ∼ 1 μm.

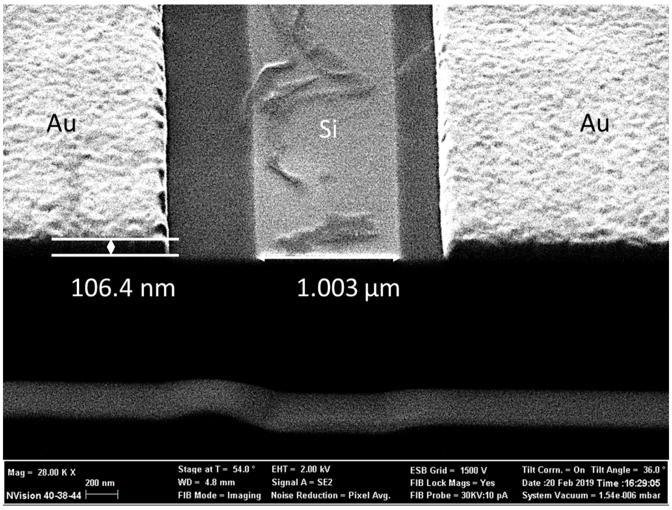

Figure 5.18: SEM image of the cross-section of the metal-graphene-metal junction.

Since the high waveguide propagation loss and grating coupling loss made it hard to measure a reliable photocurrent, instead of using the grating coupling method, the input fibre was placed above the graphene photodetector, to verify its functioning. Figure 5.19 sketches the measurement configuration, where the input fibre has been placed above a metal-graphene-metal channel with the same DC probes placed on the electrodes. The fibre remained the same fibre angle when calibrating the optical transmission with the optical power measurement.

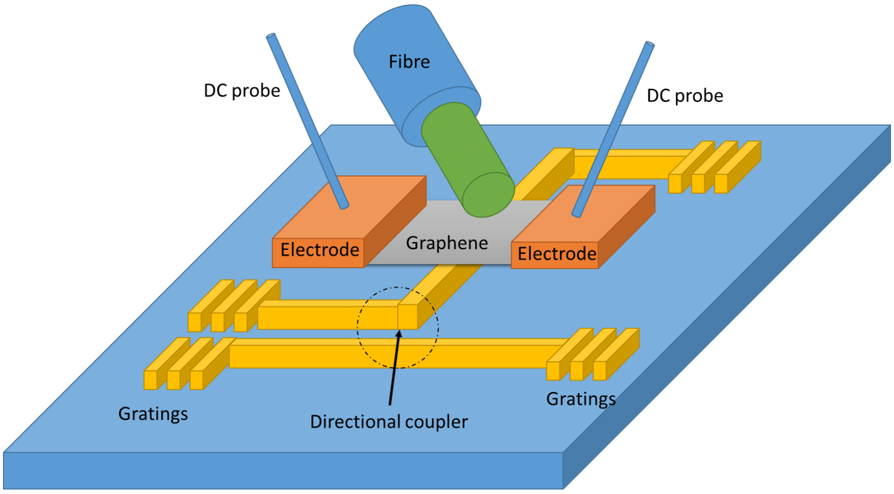

Figure 5.19: Schematic the characterisation configuration.

Instead of using the picoammeter as a voltage source and measuring the currents across two electrodes, the current source mode was used instead and the voltage was measured. The reason was that the built-in resistor of the picoammeter was similar to the resistance of the metal-graphene-metal transistor (few kΩ), thus by using a current source, it was the parallel connection instead of cascade connection, where the measurement was more accurate. The voltage was measured by the lock-in amplifier. Figure 5.20 shows the equivalent circuit diagram of the parallel connection. The built-in resistance of the lock-in amplifier was up to mega ohms thus the voltage across the graphene MIR detector could be measured. The measurement setup remained the same as for all the other measurements, except that the output fibre and detectors were not used.

Figure 5.21 shows the voltage measured by the lock-in amplifier with respect to the measuring points, where the laser was turned on and off every 25 points, the time difference between measuring points was 1 second. The current applied on the metal-graphene-metal channel was 1 μA.

The red points were measured with the picoameter current source switched off, whereas the blue points with the 1 μA current. It can be seen clearly that the voltage increases when the laser light is on (blue points). Moreover, without applying a current the change of the measured voltage was smaller than with the current source. It can be concluded that without applying the current source, the photodetection mechanism of the graphene mid-infrared photodetector is the photo-thermoelectric effect, a temperature gradient was created at the graphene-metal junctions.

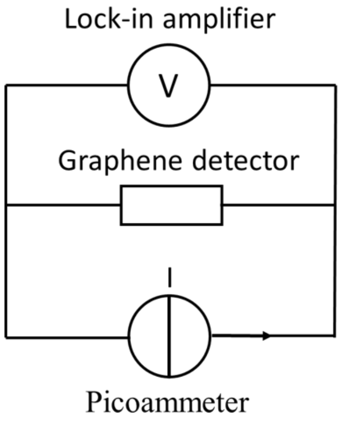

Figure 5.20: Equivalent circuit of using picoameter as a current source, and measuring the voltage across the graphene MIR photodetector using a lock-in amplifier.

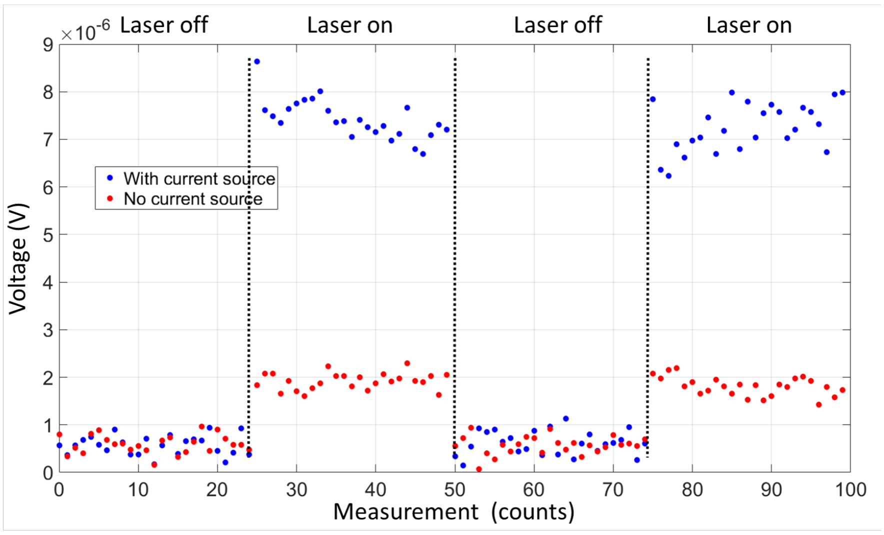

Figure 5.21: Measured voltages across the electrodes when input fibre was placed on top of the detector.

When the current source is applied between the metal-graphene-metal junction, the photodetection mechanism was the combination of the photo-thermoelectric effect and the photovoltaic effect. The current applied at the metal-graphene-metal junction enhances the separation of photocarriers.

The signal to noise ratios between the measurements with and the without current source were 10 dB and 5 dB, respectively. Under the same position, measurements of the voltage readings from the lock-in amplifier with the laser on and off were measured and plotted in Figure 5.22 with increasing QCL laser currents with the 1 μA current applied. It also confirmed that photovoltage was produced when the laser was switched on under the normal incidence when applying the current source.

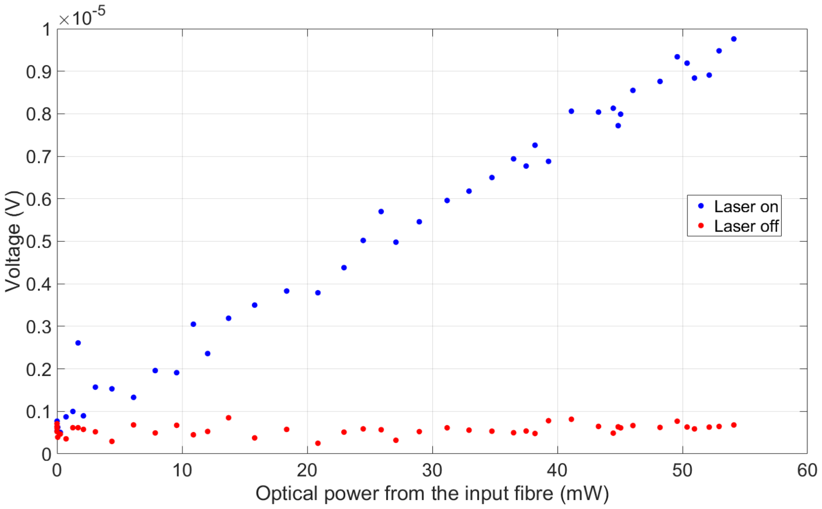

Figure 5.22: Measured voltage across the electrodes with respect to the increasing QCL laser currents, with a 1 μA current applied through the detector.

With this measurement configuration, the graphene MIR photodetector voltage was measured at different chopper frequencies as shown in Figure 5.23. Two frequency ranges were tested, one was ranging from 20-1000 Hz (a) and the other one was from 1000 Hz to 10KHz (b), which was the highest frequency that the chopper could reach. From the measured spectra, under different input frequencies, the voltages measured from graphene-metal-graphene channel remained flat. Two frequency ranges were measured due to the difference positions of the same chopper blade.

It can be seen that there were noise signals at the beginning of each measurement, and with the increase of the frequency the response of the graphene photodetector remained constant. Since 10 KHz was the maximum frequency that chopper could reach, it was not possible to test the bandwidth of the graphene photodetector. But it showed the possibility of wide bandwidth of this graphene mid-infrared photodetectors. From the literature, graphene photodetectors were promising to operate at a high frequency, such as a 40 GHz bandwidth graphene detector presented [145].

Based on the measured power at the end of the input fibre end, an estimated photoresponsivity for the light coupling on top scenario can be calculated. Figure 5.24 shows the diagram when the fibre was placed above the graphene photodetector with an angle of 15°.

The distance between two electrodes were only 2 μm, whereas the diameter of the core of the input fibre was 9 μm [218]. After light came out of the end of the input fibre, only part of the light could be absorbed by the graphene layer.

It was necessary to know how much of the light went into the graphene detector in the configuration of light is coupled from the out-of-plane direction. Thus, Lumerical Finite Different Time Domain (FDTD) solution was adopted to simulate how much of

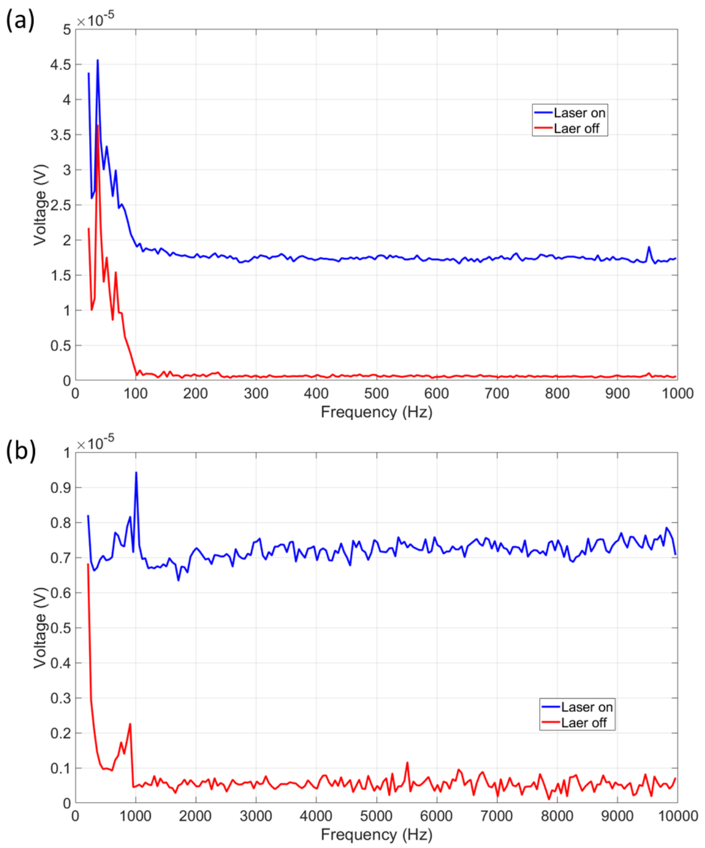

Figure 5.23: Measured voltages cross the electrodes in respect to increasing chopper frequencies under 1 μA current source; red curve represented noise and blue curve values obtained when the laser was turned on.

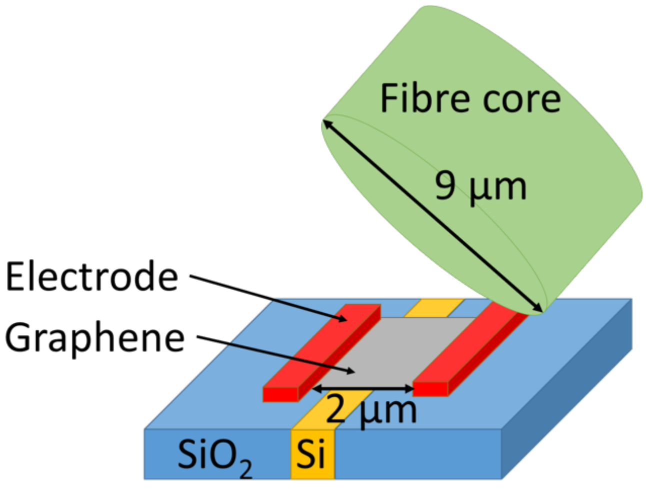

Figure 5.24: Input fibre was coupling light above the graphene detector.

the light went into the graphene photodetector. Lumerical FDTD solution uses a fully 3D Maxwell equations to solve models with complex configurations.

Figure 5.25 shows the simulation configuration, which is the side view of the experimental setup. The blue block in the image is the optical fibre with 9 μm core and 150 μm coating. The optical fibre is placed on top of the chip. The orange mesh is the simulation region, and a 2 μm wide monitor represents the metal-graphene-metal junction of the detector. The position of the monitor will be swept across the simulation region to maximise the amount of light through the junction. Based on the simulation, a maximum of 25% of transmitted light could go through the 2 μm wide monitor at a wavelength of the 3.8 μm.

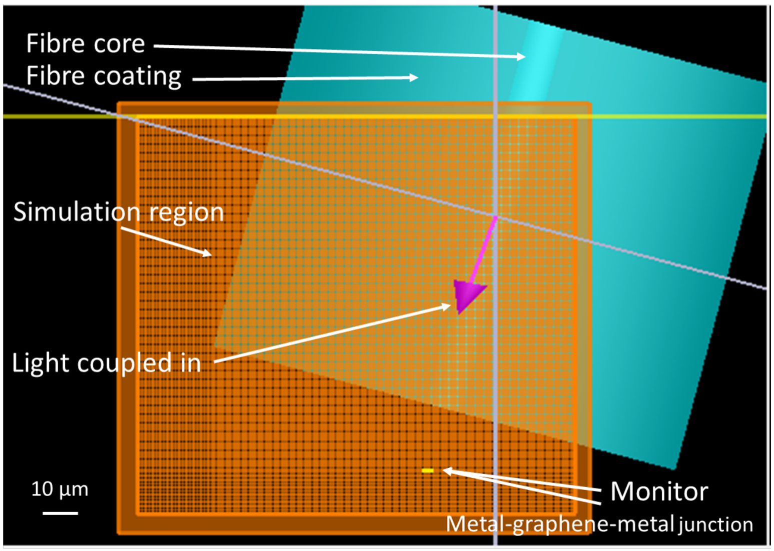

Figure 5.25: Simulation configuration for monitoring how much light went into the 2 μm wide monitor from the end of the fibre.

Based on the simulation, a maximum 25% of the power from the fibre went into the graphene photodetector, the calculated photoresponsivity was plotted in Figure 5.26. The responsivity was 0.64 mV/W based on the simulated power that was coupled into the graphene photodetector. Since only 2.3% of the incident light can be absorbed by monolayer graphene, if all the absorbed light could generate photocarriers, the internal quantum responsivity of the graphene photodetector could be up to 28 mV/W [145].

Similar work was reported on a mid-infrared graphene detector with less than 2 mV/W responsivity at 4.45 μm wavelength for out-of-plane coupling. However, the responsivity of the same device design with the metallic antenna could go up to 0.4 V/W [245]. It was shown that the use of metallic antennas could enhance in terms of the optical absorption and photocarrier collection efficiency in graphene photodetectors up to 200 times compared to devices without antennas. The photoresponse of the graphene photodetector is limited because only 2.3% of light can be absorbed under normal incidence. The external photoresponsivity can also be improved by optimising the interaction between the light and graphene.

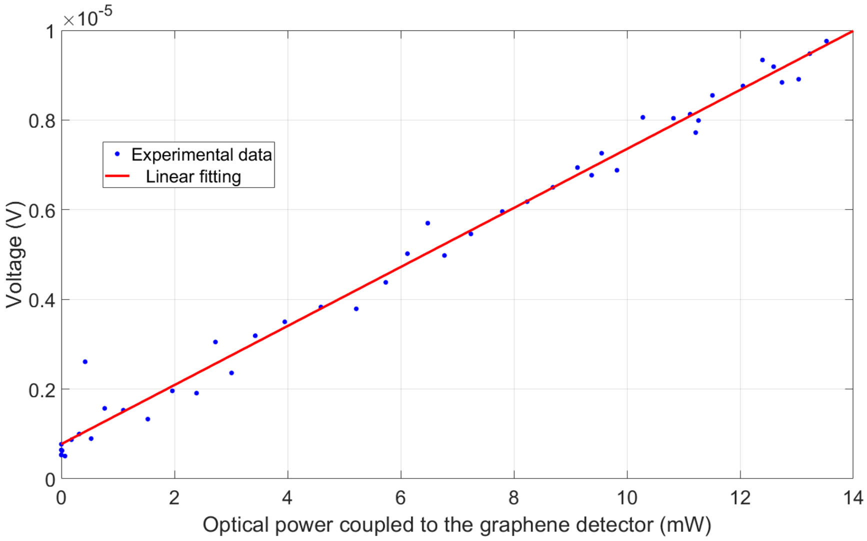

Figure 5.26: Diagram of input fibre was coupling light above the graphene detector with the simulated power went into the graphene detector.

5.6 Characterisation at 7.6 μm setup

The planarised silicon waveguide integrated graphene mid-infrared photodetectors were also characterised on the 7.6 μm setup due to 7.6 μm being close to the finger print region for remote sensing applications. The source was a quantum cascade laser from Thorlabs [246]. The fibre used was made from AsSe glass with a 11 μm diameter core [247].

Figure 5.27 shows the voltage measured by the lock-in amplifier in respect to the measuring points and each point was averaged from 100 measurements, where the laser was turned on and off every 25 points. The current applied on the metal-graphene-metal channel and had 1 μA.

The signal to noise ratios between the measurements with and without the current source were 6 dB and 3 dB, respectively. Compared with the results obtained at the wavelength of 3.8 μm, results obtained at the 7.6 μm had higher noise, which was due to less optical power being coupled into the optical fibre. Figure 5.28 shows the laser current with respect to the voltages reading from the lock-in amplifier.

When the laser was switched on, the spectrum obtained was due to the working function of the laser, i.e. during the laser current increase the wavelength changed at the same time. Another reason that caused this shape of the spectrum could be the reflection between the fibre facet and the chip surface.

Under the same position, measurements of the voltage readings from the lock-in amplifier with the laser on and off were performed. Due to the spectrum from Figure 5.28, the

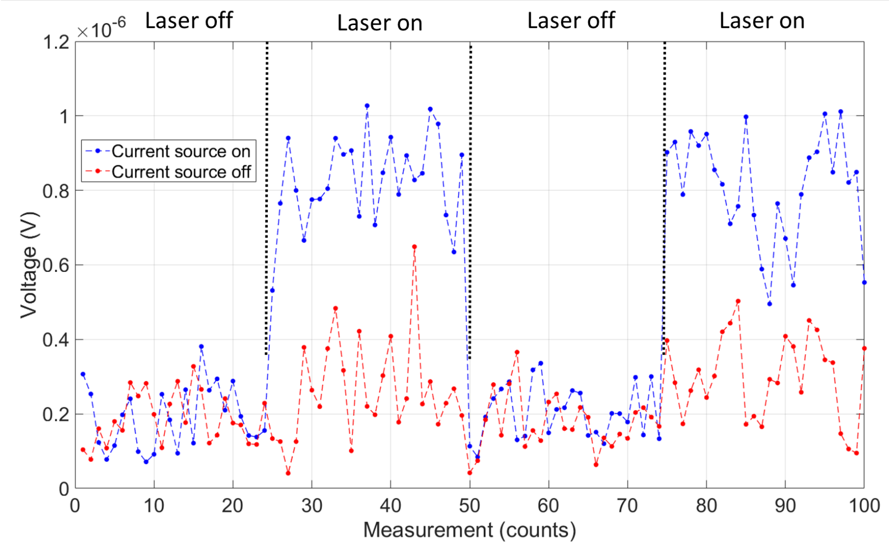

Figure 5.27: Measured voltages across the electrodes when input fibre was placed on top of the detector.

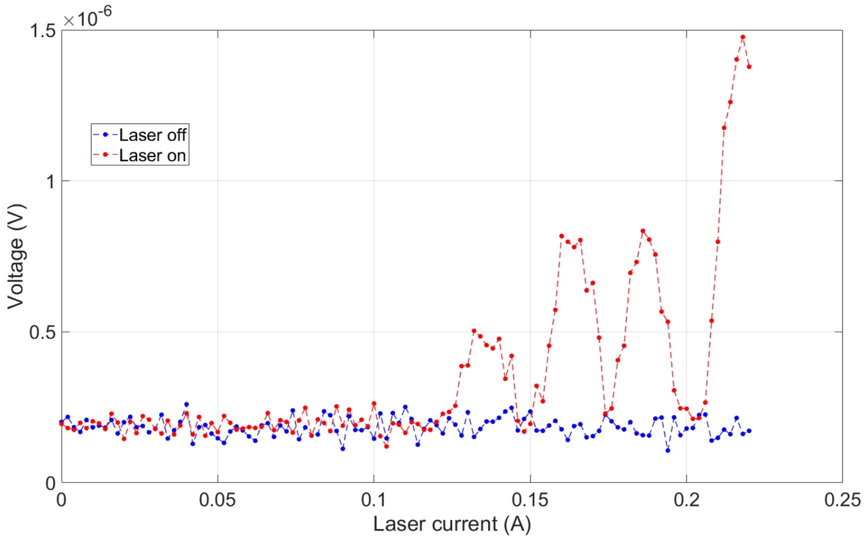

Figure 5.28: Measured voltages across the electrodes with respect to the laser current at the 7.6 μm wavelength.

relation between the optical power with voltage readings from the lock-in amplifier was not linear, which could be seen in Figure 5.29.

Due to this relation, an estimation of photoresponsivity was determined based on the voltage readings obtained from laser on and off instead of the gradient of the increasing optical power versus lock-in amplifier reading. Simulations similar to those in Figure 5.26 were performed, but this time at the wavelength of 7.6 μm, and for fibre core diameter of 11 μm and fibre cladding diameter of 125 μm. A maximum of 18% of the power was coupled into the graphene sheet (simulation monitor), thus an estimated external photoresponsivity of graphene photodetector for the out-of-plane coupling method was

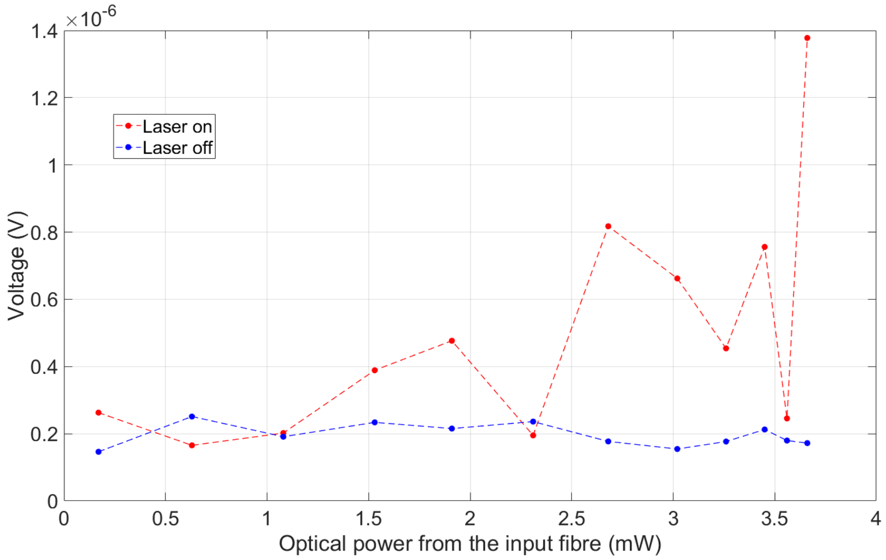

Figure 5.29: Measured voltage across the electrodes with respect to the increasing QCL laser currents, with a 1 μA current applied through the detector.

0.66 mV/W at the 7.6 μm wavelength. This was similar to the result at the 3.8 μm wavelength, thus the graphene photodetector had internal responsivity around 28 mV/W since only 2.3% of power was absorbed by monolayer graphene. It also reflected the universal absorption of graphene across wide range of wavelengths.

5.7 Summary

The responsivity of the rib graphene photodetector was 2.2 mA/W at the 3.8 μm wavelength. The high propagation loss of the waveguide limited the performance of the graphene photodetector, since the measured photocurrent was just above the dark current. Moreover, due to the 3D structure of the rib waveguides, graphene could break during fabrication. Therefore, a planarised device geometry was adopted.

High propagation loss of the waveguide was a result of PECVD, CMP procedures and graphene transfer. No reliable results were obtained for grating coupling, thus, the input fibre was placed above the metal-graphene-metal junctions to form an out-of-plane coupling. Reliable and repeatable results were obtained when using the picoameter as a current source and the lock-in amplifier as a voltage meter, indicating that the detector would work if the input waveguide and grating loss were smaller. The photoresponsivity was 0.64 mV/W based on simulated optical power that was coupled into the graphene detector from the fibre.

Both approaches suffered from fabrication issues. Apart from reducing contamination during fabrication processes, approaches such as introducing metallic antenna, optimising graphene-light interaction, or adding bias gate can all improve the photoresponsivity dramatically, which may be included in future designs.

Chapter 6

Conclusions and future work

6.1 Conclusions

Mid-infrared (MIR) group-IV photonics is promising for building photonic integrated lab-on-a-chip sensors to be used in applications such as remote sensing, biomedical diagnostics, environmental monitoring and industrial process control. In order to build the next generation of integrated photonics sensors, both MIR passive and active devices are needed. SOI platform is widely used for passive devices in the near-IR and it has the capability to be used in the MIR up to 4 μm. Above 4 μm the SiO_2 lower cladding has high loss.

Photodetectors are one of the key optoelectronic components in any photonic sensing system. Currently available products are normally made from III-V materials which are expensive and hard to fabricate, especially to integrate them with silicon photonic waveguides. 2-D materials might be able to solve the problem which III-V bulk detectors have, because of their superb optical and electrical properties, but more importantly they can be fabricated easily with much lower cost compared to III-V materials and they are easier to integrate with silicon photonics waveguides. Graphene in particular can not only interact with light over an extremely wide wavelength range but it also shows excellent conductivity, mechanical strength and compatibility with standard silicon technology, which makes it a favourable material for photodetection.

Even though graphene benefits from a strong interband transition in the MIR, only 2.3% of the incident light can be absorbed from normal incidence. On the other hand, when graphene is coupled with silicon waveguides an evanescent field is formed, thus, the graphene-light interaction length can be extended to maximise the absorption. Photodetectors based on graphene have been intensively investigated from fundamental physical mechanisms to methodologies for improving the photoresponse and a detailed review of graphene-integrated photodetectors is given in Chapter 2. However, waveguide integrated graphene mid-infrared photodetectors have not previously been demonstrated at wavelengths above 2.75 μm.

In this project, single mode SOI strip waveguides with 500 nm thickness and 1.3 μm width were presented with 2.5 dB/cm propagation loss at the 3.8 μm wavelength, which is acceptable to be used in the MIR. The low loss mid-infrared waveguides could be used as the foundation to build graphene mid-infrared integrated photodetectors. The simulation, fabrication and characterisation of mid-infrared waveguides were presented in Chapter 3.

Chapter 4 described investigation of the performance of graphene coupled silicon waveguides, which included the graphene transfer procedure, patterning process and characterisation. The investigation had three stages, the first stage was to confirm the success of the fabrication procedures, and the graphene coupled SOI waveguides had 382 ± 30 dB/cm propagation losses at 3715-3880 nm, the result matched with the simulation value (315 dB/cm at 3800 nm). A 200 dB/cm graphene absorption on silicon waveguides at 1550 nm was also published [102], the discrepancy could be attributable to the waveguide geometry, operating wavelength and residuals left after graphene transfer and patterning processes.

In order to improve the quality of graphene transfer my SOI samples were sent to Applied Nanolayers (ANL) company who performed the graphene transfer. They also patterned graphene above the silicon waveguides with a 90 nm thick SiO_2 top cladding that was required for better alignment. The propagation loss of graphene coupled with silicon waveguides with top cladding was about 150 dB at the 3.8 μm wavelength. The loss was lower than in the first stage as there was a 90 nm SiO_2 cladding decreasing graphene-optical mode interaction and hence absorption. However, the 3D waveguide geometry might damage the graphene as indicated by there bring a defect peak from the Raman spectrum.

Therefore, in the third stage of the investigation, graphene was transferred on top of silicon waveguides that were planarised using chemical mechanical polishing, for the purpose of creating a flat surface to transfer the graphene onto, and to avoid breakages at the waveguide edges. The samples were sent to the Cambridge Graphene Centre at the University of Cambridge for graphene processing and metallisation. However, due to fabrication issues, the waveguides were over polished after non-uniform PECVD deposition and further contamination was introduced during the graphene transfer process, resulting in high waveguide loss and high grating coupling loss. Both the second and the third stages showed high waveguide losses even without coupling with graphene, which influenced the performances of the photodetectors that were made from these waveguides. This underlines the main issue with graphene fabrication, potential contamination during graphene transfer which can result in high losses of photonic devices. A potential solution could be a direct CVD growth of graphene on Si or Ge platforms.

Two types of SOI waveguide integrated graphene mid-infrared detectors were presented in Chapter 5. The first type of the graphene detector was the rib waveguide with 90 nm thick SiO_2 cladding that had an asymmetric electrode configuration. A 2.2 mA/W responsivity was obtained under the -1 V bias, which is the longest wavelength demonstration to date of waveguide integrated graphene photodetector. Due to a waveguide loss, the photocurrent was just above the dark current (-13 μA at -1 V bias). The signal to noise ratio was about 0.3 dB, which made it harder to carry out the measurement since not enough optical power was absorbed by the graphene. The second design of the graphene integrated mid-infrared photodetector was based on the planarised silicon waveguides. Due to CMP polishing and non-uniform PECVD deposition, the geometry of the waveguides was significantly changed compared to the designed geometry and additional loss was introduced during the graphene processing and metallisation at the University of Cambridge, thus no reliable results were obtained when coupling light into the detectors through the input waveguides. Another issue was that graphene was not covered with a protective layer after the transfer and it could have degraded throughout the experimental characterisation in Southampton. However, subsequently, the input fibre was placed on top of metal-graphene-metal junctions to investigate detection using an out-of-plane coupling method. By applying a 1μA current source on the metal-graphene-metal junction, a maximum responsivity of 0.64 mV/W was estimated at the 3.8 μm wavelength, based on the FDTD simulation of the maximum amount of light coupled into the metal-graphene-metal junctions. The chip was also characterised from the normal incidence under the 7.7 μm wavelength setup and a 0.66 mV/W responsivity was obtained. This is the first demonstration of monolayer graphene photodetector at this wavelength. It confirmed that graphene is a promising material for photodetection for even longer wavelengths.

Despite the fabrication issues, SOI waveguide integrated graphene mid-infrared photodetectors have been demonstrated. Results obtained from both types of integrated graphene photodetectors are lower than the work have been reviewed in the literature. The highest responsivity has been published in the mid infrared was 0.13 A/W at the 2.75 μm wavelength [172]. A integrated graphene photodetector that was also based on the metal-graphene-metal junction had a 6.1 mA/W responsivity at the NIR [163]. Compared with performances of commercially available products made from III-V materials, 2.2 mA/W responsivity from the work presented is low and has a large space to improve. Since commercial detectors normally need cooling and fabrication can be complex and expensive, the advantage of the graphene detector is also obvious as it can work at room temperature and can be relativelyeasily fabricated. On the other hand, compared to other integrated graphene photodetector work that has been published (in hundreds of mA/W), the work presented in this thesis has less gap to close compared to the commercial products.

These results have shown the potential of graphene integrated with silicon waveguides for building graphene photodetectors based on the evanescent field coupling method if the fabrication can be improved and losses can be reduced. Higher performances can be achieved by developing more sophisticated device geometries to enhance graphene/light interaction by introducing metallic antennas to increase the graphene absorption.

6.2 Future work

From the results obtained in the presented work, the most important tasks are to reduce the losses from the fabrication and to improve the graphene-light interaction to enhance the graphene absorption. Many approaches have been described in the literature. If the graphene integrated mid-infrared photodetector is intended to be used in sensing applications in the fingerprint range, a new type of waveguide platform is needed, because the SOI platform can only support up to 4 μm. From the literature review, many group-IV material platforms that could possible be used in the mid-infrared have been presented. Each platform has its own disadvantages and one of the biggest issues is the limited transparency windows they have. Among all of the platforms, Ge-on-Si has the widest transmission range. Moreover, these waveguides can be suspended and germanium membrane waveguide is a new type of germanium based platform, where the full transparency window of germanium can be explored, which makes it extremely useful in the fingerprint region for sensing applications. On the other hand, graphene can be directly grown onto the germanium surface [248], thus the graphene transfer process can be avoided, which would simplify the total fabrication flow and potentially the high losses created during the graphene transfer processes could be avoided.

There is still a long way to go in terms of the large scale and practical applications for graphene and other 2-D materials. As reviewed before, there are more than four photodetection mechanisms of graphene and other 2-D materials, and further investigations are required to fully understand the mechanisms dominating in different situations. It is also necessary to optimise the performance, such as by tailoring the device configuration or by optimising material engineering. For example, in order to achieve fast response, the photoelectric effect is the best choice whilst photo-thermoelectric effect and bolometric effects have to be eliminated. For the purpose of increasing the photoresponse of the device, carefully designed device configurations can increase the overlap between the graphene and the mode. On the other hand, material engineering should be carefully designed in order to maintain the quality of the 2-D materials, because the carrier mobility and response speed will be decreased if there are damages or defects in 2-D materials.

New properties of graphene have been discovered, such as the unique properties of Dirac plasmons inside graphene [249–252]. This offers a new path in designing high-performance graphene photodetectors. Plasmons in graphene can lead to an increase of the response by a factor of 40 and can be tuned by chemical/electrostatic doping [253], which is important because a strong optical field confinement can be achieved.

The goal of achieving a full suite of group IV integrated photonic circuits involves the development of several active devices, such as modulators, lasers and photodetectors. It is worth noticing that graphene and other 2D materials can be integrated into optoelectronic devices other than photodetectors [254, 255, 54]. The idea of coupling graphene with silicon photonics was first proposed and realised in optical modulators. In one demonstration of largescale monolayer graphene integration with silicon waveguides the optical absorption of graphene was modulated by changing the doping level electrically, where a broadband optical modulation across the 1.3-1.6 μm range was presented [256, 257]. Apart from electrical modulation, photo-absorption of graphene can be tuned by controlling the transmission optically. An all optical modulation was demonstrated within a graphene integrated silicon waveguide structure [258]. It is possible to achieve a more sophisticated modulator by combing silicon waveguides with other carefully designed devices such as ring resonators to enhance the modulation depth of graphene modulator, which showed a more efficient amplitude modulation by changing the absorption of graphene [259, 260]. It has also been shown that an electro-optic modulator can be formed by integrating a graphene/hBN stack with a photonic crystal cavity in order to enhance the modulation depth [261].

On the other hand, since it is a gapless material, the semimetallic nature of graphene implies that graphene is not an ideal material to be used as a light source. Fortunately, the wide range of 2-D materials has more to offer. Using other 2-D materials may fill the gap of applications, for example monolayer TMDs are semiconductors with direct bandgaps and exhibit excellent quantum emission properties [262]. Another advantage of monolayer transition metal dichalcogenides (TMDs) is that their large exciton binding energy [263], which results in long lifetime excitons that are very promising to be used as light emission materials. There are demonstrations of laser diodes made from TMDs integrated with photonic devices such as micro-disk resonators and photonic crystal cavities, which achieved amplified spontaneous emissions [264, 265], and possibly coherent light sources eventually. Besides, black phosphorus is another semiconductor 2-D material with a direct bandgap regardless of the number of layers. It has a wide-range of tunable bandgap from 0.3 eV in 3D bulk formation to 2 eV in monolayer, which offers a potential of high light-matter interaction in the mid-infrared range, and it has been proposed to be implemented into integrated modulator already [266]. Above all, graphene and 2-D materials integrated with group IV photonics can be used for realising lab-on-a-chip sensors in the finger print region for remote sensing applications.

Appendix A

Appendix

A.1 Type (1)Macro files

The code presented in the following is an example showing that a code was used to draw a set of waveguides with increasing waveguide lengths. This example uses types of files include: (a) grating couplers, (2) waveguides, (3) tapers.

```
/**************************************
* Macro Name: InsertionLoss
File Name: InsertionLoss.cpp
* Creator  : Z.Qu
* Revision History: v1
* 19/10/16
********************
#define MACRONAME InsertionLoss
#define MACROSTRING "InsertionLoss"

#include "..\headers\stdHeaders.h"  //Include the standard set of headers
#include "..\headers\components.h" //Include the component function files

////////////////// main function ///////////////
void MACRONAME(void)
{

//////////////////Set up layers////////////////
LCell pCell = LCell_GetVisible();
LFile pFile = LCell_GetFile(pCell);
LPoint centre = LPoint_Set(0, 0);
```

```
//Initialize default layers:
layers_CLASS layers;
layers.list = layers.setdefaultlist(pFile);


////// 1. declare all component types, and set all common variables:
//Declare subwavelength grating coupler type:
SW_GC_TYPE SWGC;
SWGC.gratingP = 2 * 1000;
SWGC.direction = -1;
SWGC.lambda = 3760;
SWGC.fx = 0.5;
SWGC.fy = 0.25;
SWGC.LineNum = 10;
SWGC.width = 20;
SWGC.Theta = 12;

//Declare waveguide struct and variables:
WG_TYPE WG;
WG.W = 1.3*1000;
WG.L = 200*1000;

//Declare lhs taper struct and set variables;
Taper_TYPE TAPlhs;
TAPlhs.W1 = WG.W;
TAPlhs.W2 = 1.3*1000;
TAPlhs.angle=0;
TAPlhs.L = 560*1000;

//Declare output taper struct and set variables;
Taper_TYPE TAPrhs;
TAPrhs.W1 = SWGC.width;
TAPrhs.W2 = 1.3*1000;
TAPrhs.L = TAPlhs.L;
TAPrhs.angle=0;

//Declare graphene box struct and set variables;
WG_TYPE WGgraphene;
WGgraphene.W = 150*1000;//dont change
WGgraphene.L = 500*1000;
```

```
////Declare electrodes struct and set variables;
WG_TYPE WGelectrode1;
WGelectrode1.L = 400*1000;
WGelectrode1.W = 1000*1000;
WGelectrode1.angle = 0;

WG_TYPE WGelectrode2;
WGelectrode2.L = 400*1000;
WGelectrode2.W = 1000*1000;
WGelectrode2.angle =0;

//Declare Bend and set variables
bend_TYPE Bend;
Bend.W = 1.3*1000;
Bend.radius = 50*1000;


/////// 2. Draw waveguides of different lengths

int i;
int n = 10; //Set number of length variations
long offset = 100*1000; //Set offset between adjacent waveguides.
long dL = 200*1000;    //Set graphene length difference.
long L1 = 5*1000; // Set offset of distance between two electrodes

for (i=0; i<n; i++)
{
SWGC.InPort.x = centre.x;
SWGC.InPort.y = centre.y + i*offset;
SWGC.direction = -1;
GC_focus_swg_taper(pCell, layer, SWGC, TAPlhs, SWGC.OutPort);

/* //Draw first  input bend
Bend.InPort = SWGC.OutPort;
Bend.start_angle = 0;
Bend.end_angle = 90;
bend(pCell, layer[0], Bend, Bend.OutPort); //bend 1 */

WG.InPort = SWGC.OutPort;
WG.angle = 0;
```

```
WG.L = WG.L + i*dL;
waveguide(pCell, layer[0], WG, WG.OutPort);

/* //Draw graphene window:
WGgraphene.InPort.x = WG.InPort.x;
WGgraphene.InPort.y = WG.InPort.y + 50*1000;
WGgraphene.angle = 90;
WGgraphene.L = WGgraphene.L - dL;
waveguide(pCell, layer[1], WGgraphene, WGgraphene.OutPort);

// Draw electrodes
WGelectrode1.InPort.x = WG.InPort.x - WGelectrode1.L - 0.5*WG.W;
WGelectrode1.InPort.y = WG.InPort.y + 50*1000 + 0.5* WGgraphene.L;
waveguide(pCell, layer[2], WGelectrode1, WGelectrode1.OutPort);

WGelectrode2.InPort.x = WG.InPort.x + 0.5*WG.W + i*L1;
WGelectrode2.InPort.y = WG.InPort.y + 50*1000 + 0.5* WGgraphene.L;
waveguide(pCell, layer[2], WGelectrode2, WGelectrode2.OutPort); */

//Draw output bend
/* Bend.InPort = WG.OutPort;
Bend.start_angle = 90;
Bend.end_angle = 0;
bend(pCell, layer[0], Bend, Bend.OutPort); //bend 2 */

SWGC.InPort  = WG.OutPort;
SWGC.direction = 1;
GC_focus_swg_taper(pCell, layer, SWGC, TAPrhs, SWGC.OutPort);

}//end for

}//end InsertionLoss (end main)
```

A.2 Type (2) macro file

The following file is an example of code that draws a photodetection region where contains a directional coupler to split the light into the reference arm and the waveguide connected to the graphene photodetector, also with the graphene detector with electrodes on the sides.

```
/************************
```

```
* Macro Name: DirecCoup_500umPD
File Name: DirecCoup_500umPD.cpp
* Creator  : Z.Qu
* Revision History: v1
* 19/10/16

#define MACRONAME DirecCoup_500umPD
#define MACROSTRING "DirecCoup_500umPD"

#include "..\headers\stdHeaders.h"  //Include the standard set of headers
#include "..\headers\components.h" //Include the component function files

//////////////////// main function //////////////
void MACRONAME(void)
{

////////////////////Set up layers///////////////
LCell pCell = LCell_GetVisible();
LFile pFile = LCell_GetFile(pCell);
LPoint centre = LPoint_Set(0, 0);

//Initialize default layers:
layers_CLASS layers;
layers.list = layers.setdefaultlist(pFile);


//////  1. declare all component types, and set all common variables:
//Declare subwavelength grating coupler type:
SW_GC_TYPE SWGC;
SWGC.gratingP = 2 * 1000;
SWGC.direction = -1;
SWGC.lambda = 3760;
SWGC.fx = 0.5;
SWGC.fy = 0.25;
SWGC.LineNum = 10;
SWGC.width = 20;
SWGC.Theta = 12;

//Declare waveguide struct and variables:
WG_TYPE WG;
WG.W = 1.3*1000;
```

```
WG.L = 1100*1000;

//Declare Directional coupler approach waveguide variables;
WG_TYPE WGDCApproach;
WGDCApproach.W = 1.3*1000;
WGDCApproach.L = 17*1000;

//Declare lhs taper struct and set variables;
Taper_TYPE TAPlhs;
TAPlhs.W1 = WG.W;
TAPlhs.W2 = 1.3*1000;
TAPlhs.angle=0;
TAPlhs.L = 560*1000;

//Declare output taper struct and set variables;
Taper_TYPE TAPrhs;
TAPrhs.W1 = SWGC.width;
TAPrhs.W2 = 1.3*1000;
TAPrhs.L = TAPlhs.L;
TAPrhs.angle=0;

//Declare graphene box struct and set variables;
WG_TYPE WGgraphene;
WGgraphene.W = 150*1000;//dont change
WGgraphene.L = 500*1000;


////Declare electrodes struct and set variables;
WG_TYPE WGelectrode1;
WGelectrode1.L = 400*1000;
WGelectrode1.W = 500*1000;
WGelectrode1.angle = 0;

WG_TYPE WGelectrode2;
WGelectrode2.L = 400*1000;
WGelectrode2.W = 500*1000;
WGelectrode2.angle =0;

//Declare Bend and set variables
bend_TYPE Bend;
Bend.W = 1.3*1000;
```

```
Bend.radius = 50*1000;

//Declare directional coupler section
WG_TYPE WGDCoupler;
WGDCoupler.W = 1.3*1000;



/////// 2. Draw waveguides of different lengths
int i;
int n = 9; //Set number of length variations
long offset = 900*1000; //Set offset between adjacent waveguides.
long dL = 1000*1000; //Set graphene length difference.
long L1 = 0.5*1000; // Set offset of distance between two electrodes

for (i=0; i<n; i++)
{
SWGC.InPort.x = centre.x;
SWGC.InPort.y = centre.y + i*offset;
SWGC.direction = -1;
GC_focus_swg_taper(pCell, layer, SWGC, TAPlhs, SWGC.OutPort);

//Draw first input bend
Bend.InPort = SWGC.OutPort;
Bend.start_angle = 0;
Bend.end_angle = 270;
bend(pCell, layer[0], Bend, Bend.OutPort); //bend 1

//Draw second input bend
Bend.InPort = Bend.OutPort;
Bend.start_angle = 270;
Bend.end_angle = 0;
bend(pCell, layer[0], Bend, Bend.OutPort); //bend 2

//Draw waveguide DC part with 17um length
WG.InPort.x = Bend.OutPort.x;
WG.InPort.y= Bend.OutPort.y;
WG.L = 17*1000;
WG.angle = 0;

waveguide(pCell, layer[0], WG, WG.OutPort);
```

```
//Draw third input bend
Bend.InPort = WG.OutPort;
Bend.start_angle = 0;
Bend.end_angle = 90;
bend(pCell, layer[0], Bend, Bend.OutPort); //bend 3

//Draw waveguide
WG.InPort = Bend.OutPort;
WG.angle = 90;
WG.L = 700*1000;
waveguide(pCell, layer[0], WG, WG.OutPort);

//Draw graphene window:
WGgraphene.InPort.x = WG.InPort.x;
WGgraphene.InPort.y = WG.InPort.y + 100*1000;
WGgraphene.angle = 90;

waveguide(pCell, layer[1], WGgraphene, WGgraphene.OutPort);

// Draw electrodes
WGelectrode1.InPort.x = WG.InPort.x - WGelectrode1.L - 0.5*WG.W - 500;
WGelectrode1.InPort.y = WG.InPort.y + 100*1000 + 0.5* WGgraphene.L;
waveguide(pCell, layer[2], WGelectrode1, WGelectrode1.OutPort);

WGelectrode2.InPort.x = WG.InPort.x + 0.5*WG.W + i*L1 + 500;
WGelectrode2.InPort.y = WG.InPort.y + 100*1000 + 0.5* WGgraphene.L;
waveguide(pCell, layer[2], WGelectrode2, WGelectrode2.OutPort);

//Draw output bend
Bend.InPort = WG.OutPort;
Bend.start_angle = 90;
Bend.end_angle = 0;
bend(pCell, layer[0], Bend, Bend.OutPort); //bend 2


SWGC.InPort  = Bend.OutPort;
SWGC.direction = 1;
GC_focus_swg_taper(pCell, layer, SWGC, TAPrhs, SWGC.OutPort);

//Draw Subwavelength grating at the input side of DC coupler
```

```
SWGC.InPort.x = centre.x; //
SWGC.InPort.y = centre.y  - 101.7*1000 + i*offset;
SWGC.direction = -1;
GC_focus_swg_taper(pCell, layer, SWGC, TAPrhs, SWGC.OutPort);

//Draw directional coupler
WGDCoupler.InPort.x = SWGC.OutPort.x;
WGDCoupler.InPort.y = SWGC.OutPort.y;
WGDCoupler.angle = 0;
WGDCoupler.L = 200*1000;
waveguide(pCell, layer[0], WGDCoupler, WGDCoupler.OutPort);

//Draw Subwavelength grating at the output side of DC coupler
SWGC.InPort  = WGDCoupler.OutPort;
SWGC.direction = 1;
GC_focus_swg_taper(pCell, layer, SWGC, TAPrhs, SWGC.OutPort);

}//end for

}//end DirecCoup_500umPD (end main)
```

References

[1] Richard Soref. Mid-infrared photonics in silicon and germanium. *Nature Photonics*, 4(8):495–497, 2010.

[2] David AB Miller. Device requirements for optical interconnects to silicon chips. *Proceedings of the IEEE*, 97(7):1166–1185, 2009.

[3] Graham T Reed, G Mashanovich, FY Gardes, and DJ Thomson. Silicon optical modulators. *Nature photonics*, 4(8):518–526, 2010.

[4] Youfang Hu, DJ Thomson, AZ Khokhar, S Stanković, CJ Mitchell, FY Gardes, J Soler Penades, GZ Mashanovich, and GT Reed. Angled multimode interferometer for bidirectional wavelength division (de) multiplexing. *Royal Society open science*, 2(10):150270, 2015.

[5] K Takada, M Abe, T Shibata, and K Okamoto. 10-GHz-spaced 1010-channel tandem awg filter consisting of one primary and ten secondary AWGs. *IEEE Photonics Technology Letters*, 13(6):577–578, 2001.

[6] Dazeng Feng, Wei Qian, Hong Liang, B Jonathan Luff, and Mehdi Asghari. High-speed receiver technology on the SOI platform. *IEEE journal of selected topics in quantum electronics*, 19(2):3800108–3800108, 2013.

[7] Yang Wang, Shitao Gao, Ke Wang, and Efstratios Skafidas. Ultra-broadband and low-loss optical power splitter based on tapered silicon waveguides. In *Optical Interconnects Conference (OI), 2015 IEEE*, pages 80–81. IEEE, 2015.

[8] Ting Hu, Haodong Qiu, Zecen Zhang, Xin Guo, Chongyang Liu, Mohamed S Rouifed, Callum G Littlejohns, Graham T Reed, and Hong Wang. A compact ultrabroadband polarization beam splitter utilizing a hybrid plasmonic Y-branch. *IEEE Photonics Journal*, 8(4):1–9, 2016.

[9] Ansheng Liu, Ling Liao, Doron Rubin, Hat Nguyen, Berkehan Ciftcioglu, Yoel Chetrit, Nahum Izhaky, and Mario Paniccia. High-speed optical modulation based on carrier depletion in a silicon waveguide. *Optics Express*, 15(2):660–668, 2007.

[10] Graham T Reed, David J Thomson, Frederic Y Gardes, Youfang Hu, Jean-Marc Fedeli, and Goran Z Mashanovich. High-speed carrier-depletion silicon Mach-Zehnder optical modulators with lateral PN junctions. *Frontiers in Physics*, 2:77, 2014.

[11] Dazeng Feng, Shirong Liao, Hong Liang, Joan Fong, Bhavin Bijlani, Roshanak Shafiiha, B Jonathan Luff, Ying Luo, Jack Cunningham, Ashok V Krishnamoorthy, et al. High speed GeSi electro-absorption modulator at 1550 nm wavelength on SOI waveguide. *Optics express*, 20(20):22224–22232, 2012.

[12] Roman Bruck, Kevin Vynck, Philippe Lalanne, Ben Mills, David J Thomson, Goran Z Mashanovich, Graham T Reed, and Otto L Muskens. All-optical spatial light modulator for reconfigurable silicon photonic circuits. *Optica*, 3(4):396–402, 2016.

[13] Jurgen Michel, Jifeng Liu, and Lionel C Kimerling. High-performance Ge-on-Si photodetectors. *Nature photonics*, 4(8):527, 2010.

[14] Dazeng Feng, Shirong Liao, Po Dong, Ning-Ning Feng, Hong Liang, Dawei Zheng, Cheng-Chih Kung, Joan Fong, Roshanak Shafiiha, Jack Cunningham, et al. High-speed Ge photodetector monolithically integrated with large cross-section silicon-on-insulator waveguide. *Applied Physics Letters*, 95(26):261105, 2009.

[15] Olufemi I Dosunmu, Douglas D Cannon, Matthew K Emsley, Lionel C Kimerling, and M Selim Unlu. High-speed resonant cavity enhanced Ge photodetectors on reflecting Si substrates for 1550-nm operation. *IEEE Photonics Technology Letters*, 17(1):175–177, 2005.

[16] Intel. Silicon Photonics Optical Transceivers. `https://www.intel.co.uk/content/www/uk/en/products/network-io/high-performance-fabrics/silicon-photonics.html//`, 2019. Accessed: 17/08/2019.

[17] Luxtera. 2 x 100G-PSM4 OptoPHY Product Family. `http://www.luxtera.com/embedded-optics//`, 2019. Accessed: 17/08/2019.

[18] IBM. Silicon Photonics. `https://www.zurich.ibm.com/st/photonics/optics.html//`, 2019. Accessed: 17/08/2019.

[19] Rocklary Photonics. Technology, Driving the next generation of silicon photonics. `https://rockleyphotonics.com/technology//`, 2019. Accessed: 17/08/2019.

[20] Nikolai N Klimov, Sunil Mittal, Michaela Berger, and Zeeshan Ahmed. On-chip silicon waveguide bragg grating photonic temperature sensor. *Optics letters*, 40(17):3934–3936, 2015.

[21] S Santosh Kumar and BD Pant. Design principles and considerations for the ideal silicon piezoresistive pressure sensor: a focused review. *Microsystem technologies*, 20(7):1213–1247, 2014.

[22] H Taghinejad, M Taghinejad, M Abdolahad, A Saeidi, and S Mohajerzadeh. Fabrication and modeling of high sensitivity humidity sensors based on doped silicon nanowires. *Sensors and Actuators B: Chemical*, 176:413–419, 2013.

[23] Shixuan Yang and Nanshu Lu. Gauge factor and stretchability of silicon-on-polymer strain gauges. *Sensors*, 13(7):8577–8594, 2013.

[24] J Gonzalo Wangüemert-Pérez, Pavel Cheben, Alejandro Ortega-Moñux, Carlos Alonso-Ramos, Diego Pérez-Galacho, Robert Halir, Iñigo Molina-Fernández, Dan-Xia Xu, and Jens H Schmid. Evanescent field waveguide sensing with subwavelength grating structures in silicon-on-insulator. *Optics letters*, 39(15):4442–4445, 2014.

[25] Yuewang Huang, Salih K Kalyoncu, Qiancheng Zhao, Rasul Torun, and Ozdal Boyraz. Silicon-on-sapphire waveguides design for mid-IR evanescent field absorption gas sensors. *Optics Communications*, 313:186–194, 2014.

[26] Wei-Cheng Lai, Swapnajit Chakravarty, Xiaolong Wang, Cheyun Lin, and Ray T Chen. On-chip methane sensing by near-IR absorption signatures in a photonic crystal slot waveguide. *Optics letters*, 36(6):984–986, 2011.

[27] K Misiakos, I Raptis, E Makarona, A Botsialas, A Salapatas, P Oikonomou, A Psarouli, PS Petrou, SE Kakabakos, Kari Tukkiniemi, et al. All-silicon monolithic Mach-Zehnder interferometer as a refractive index and bio-chemical sensor. *Optics express*, 22(22):26803–26813, 2014.

[28] Maverick. The Maverick Detection System . `https://www.genalyte.com/about-us/our-technology/`, 2019. Accessed: 19/01/2019.

[29] Ronald W Waynant, Ilko K Ilev, and Israel Gannot. Mid–infrared laser applications in medicine and biology. *Philosophical Transactions of the Royal Society of London A: Mathematical, Physical and Engineering Sciences*, 359(1780):635–644, 2001.

[30] Philip Wägli, Yu-Chi Chang, Alexandra Homsy, Lubos Hvozdara, Hans Peter Herzig, and Nico F de Rooij. Microfluidic droplet-based liquid–liquid extraction and on-chip IR spectroscopy detection of cocaine in human saliva. *Analytical chemistry*, 85(15):7558–7565, 2013.

[31] Boris Mizaikoff. Mid-infrared evanescent wave sensors-a novel approach for subsea monitoring. *Measurement Science and Technology*, 10(12):1185, 1999.

[32] Graham T Reed. *Silicon photonics: the state of the art.* John Wiley & Sons, 2008.

[33] KSA Novoselov, Andre K Geim, SVb Morozov, Da Jiang, MIc Katsnelson, IVa Grigorieva, SVb Dubonos, and AAb Firsov. Two-dimensional gas of massless Dirac fermions in graphene. *nature*, 438(7065):197–200, 2005.

[34] Branimir Radisavljevic, Aleksandra Radenovic, Jacopo Brivio, i V Giacometti, and A Kis. Single-layer MoS_2 transistors. *Nature nanotechnology*, 6(3):147, 2011.

[35] Mingsheng Xu, Tao Liang, Minmin Shi, and Hongzheng Chen. Graphene-like two-dimensional materials. *Chemical reviews*, 113(5):3766–3798, 2013.

[36] Sheneve Z Butler, Shawna M Hollen, Linyou Cao, Yi Cui, Jay A Gupta, Humberto R Gutiérrez, Tony F Heinz, Seung Sae Hong, Jiaxing Huang, Ariel F Ismach, et al. Progress, challenges, and opportunities in two-dimensional materials beyond graphene. *ACS nano*, 7(4):2898–2926, 2013.

[37] Hai Li, Jumiati Wu, Zongyou Yin, and Hua Zhang. Preparation and applications of mechanically exfoliated single-layer and multilayer MoS_2 and WSe_2 nanosheets. *Accounts of chemical research*, 47(4):1067–1075, 2014.

[38] Manish Chhowalla, Hyeon Suk Shin, Goki Eda, Lain-Jong Li, Kian Ping Loh, and Hua Zhang. The chemistry of two-dimensional layered transition metal dichalcogenide nanosheets. *Nature chemistry*, 5(4):263, 2013.

[39] Goki Eda, Hisato Yamaguchi, Damien Voiry, Takeshi Fujita, Mingwei Chen, and Manish Chhowalla. Photoluminescence from chemically exfoliated MoS_2. *Nano letters*, 11(12):5111–5116, 2011.

[40] Jonathan N Coleman, Mustafa Lotya, Arlene O?Neill, Shane D Bergin, Paul J King, Umar Khan, Karen Young, Alexandre Gaucher, Sukanta De, Ronan J Smith, et al. Two-dimensional nanosheets produced by liquid exfoliation of layered materials. *Science*, 331(6017):568–571, 2011.

[41] Kostya S Novoselov, Andre K Geim, SV Morozov, D Jiang, Y_ Zhang, SV Dubonos, IV Grigorieva, and AA Firsov. Electric field effect in atomically thin carbon films. *Science*, 306(5696):666–669, 2004.

[42] Matthew J Allen, Vincent C Tung, and Richard B Kaner. Honeycomb carbon: a review of graphene. *Chemical reviews*, 110(1):132–145, 2009.

[43] Konstantin S Novoselov, VI Fal, L Colombo, PR Gellert, MG Schwab, K Kim, et al. A roadmap for graphene. *nature*, 490(7419):192, 2012.

[44] Eduardo JH Lee, Kannan Balasubramanian, Ralf Thomas Weitz, Marko Burghard, and Klaus Kern. Contact and edge effects in graphene devices. *Nature nanotechnology*, 3(8):486–490, 2008.

[45] Kin Fai Mak, Long Ju, Feng Wang, and Tony F Heinz. Optical spectroscopy of graphene: from the far infrared to the ultraviolet. *Solid State Communications*, 152(15):1341–1349, 2012.

[46] Fengnian Xia, Hugen Yan, and Phaedon Avouris. The interaction of light and graphene: basics, devices, and applications. *Proceedings of the IEEE*, 101(7):1717–1731, 2013.

[47] Zhenhua Sun and Haixin Chang. Graphene and graphene-like two-dimensional materials in photodetection: mechanisms and methodology. *ACS nano*, 8(5):4133–4156, 2014.

[48] Ankur Gupta, Tamilselvan Sakthivel, and Sudipta Seal. Recent development in 2D materials beyond graphene. *Progress in Materials Science*, 73:44–126, 2015.

[49] Yumeng Shi, Henan Li, and Lain-Jong Li. Recent advances in controlled synthesis of two-dimensional transition metal dichalcogenides via vapour deposition techniques. *Chemical Society Reviews*, 44(9):2744–2756, 2015.

[50] Deep Jariwala, Vinod K Sangwan, Lincoln J Lauhon, Tobin J Marks, and Mark C Hersam. Emerging device applications for semiconducting two-dimensional transition metal dichalcogenides. *ACS nano*, 8(2):1102–1120, 2014.

[51] Likai Li, Yijun Yu, Guo Jun Ye, Qingqin Ge, Xuedong Ou, Hua Wu, Donglai Feng, Xian Hui Chen, and Yuanbo Zhang. Black phosphorus field-effect transistors. *Nature nanotechnology*, 9(5):372, 2014.

[52] Han Liu, Yuchen Du, Yexin Deng, and D Ye Peide. Semiconducting black phosphorus: synthesis, transport properties and electronic applications. *Chemical Society Reviews*, 44(9):2732–2743, 2015.

[53] Fengnian Xia, Han Wang, Di Xiao, Madan Dubey, and Ashwin Ramasubramaniam. Two-dimensional material nanophotonics. *Nature Photonics*, 8(12):899–907, 2014.

[54] Kin Fai Mak and Jie Shan. Photonics and optoelectronics of 2D semiconductor transition metal dichalcogenides. *Nature Photonics*, 10(4):216, 2016.

[55] Wencan Jin, Po-Chun Yeh, Nader Zaki, Datong Zhang, Jerzy T Sadowski, Abdullah Al-Mahboob, Arend M van Der Zande, Daniel A Chenet, Jerry I Dadap, Irving P Herman, et al. Direct measurement of the thickness-dependent electronic band structure of MoS_2 using angle-resolved photoemission spectroscopy. *Physical review letters*, 111(10):106801, 2013.

[56] Anthony Ayari, Enrique Cobas, Ololade Ogundadegbe, and Michael S Fuhrer. Realization and electrical characterization of ultrathin crystals of layered transition-metal dichalcogenides. *Journal of applied physics*, 101(1):014507, 2007.

[57] Han Liu, Adam T Neal, Zhen Zhu, Zhe Luo, Xianfan Xu, David Tománek, and Peide D Ye. Phosphorene: an unexplored 2D semiconductor with a high hole mobility. *ACS nano*, 8(4):4033–4041, 2014.

[58] Michele Buscema, Dirk J Groenendijk, Sofya I Blanter, Gary A Steele, Herre SJ Van Der Zant, and Andres Castellanos-Gomez. Fast and broadband photoresponse of few-layer black phosphorus field-effect transistors. *Nano letters*, 14(6):3347–3352, 2014.

[59] Deji Akinwande, Nicholas Petrone, and James Hone. Two-dimensional flexible nanoelectronics. *Nature communications*, 5:5678, 2014.

[60] Yi-Hsien Lee, Xin-Quan Zhang, Wenjing Zhang, Mu-Tung Chang, Cheng-Te Lin, Kai-Di Chang, Ya-Chu Yu, Jacob Tse-Wei Wang, Chia-Seng Chang, Lain-Jong Li, et al. Synthesis of large-area MoS_2 atomic layers with chemical vapor deposition. *Advanced materials*, 24(17):2320–2325, 2012.

[61] Nihar R Pradhan, Daniel Rhodes, Yan Xin, Shahriar Memaran, Lakshmi Bhaskaran, Muhandis Siddiq, Stephen Hill, Pulickel M Ajayan, and Luis Balicas. Ambipolar molybdenum diselenide field-effect transistors: field-effect and hall mobilities. *ACS nano*, 8(8):7923–7929, 2014.

[62] Daisuke Kiriya, Mahmut Tosun, Peida Zhao, Jeong Seuk Kang, and Ali Javey. Air-stable surface charge transfer doping of MoS_2 by benzyl viologen. *Journal of the American Chemical Society*, 136(22):7853–7856, 2014.

[63] Richard A Soref, Joachim Schmidtchen, and Klaus Petermann. Large single-mode rib waveguides in GeSi-Si and Si-on-SiO/sub 2. *IEEE Journal of Quantum Electronics*, 27(8):1971–1974, 1991.

[64] Vinita Mittal, Neil P Sessions, James S Wilkinson, and Ganapathy Senthil Murugan. Optical quality ZnSe films and low loss waveguides on Si substrates for mid-infrared applications. *Optical Materials Express*, 7(3):712–725, 2017.

[65] S Roux, L Cerutti, E Tournie, B Gérard, G Patriarche, A Grisard, and E Lallier. Low-loss orientation-patterned GaSb waveguides for mid-infrared parametric conversion. *Optical Materials Express*, 7(8):3011–3016, 2017.

[66] Aldo Gutierrez-Arroyo, Emeline Baudet, Loïc Bodiou, Jonathan Lemaitre, Isabelle Hardy, François Faijan, Bruno Bureau, Virginie Nazabal, and Joël Charrier. Optical characterization at 7.7 μm of an integrated platform based on chalcogenide waveguides for sensing applications in the mid-infrared. *Optics express*, 24(20):23109–23117, 2016.

[67] Shankar Kumar Selvaraja, Wim Bogaerts, Philippe Absil, Dries Van Thourhout, and Roel Baets. Record low-loss hybrid rib/wire waveguides for silicon photonic circuits. *Group IV Photonics*, 2010, 2010.

[68] Goran Z Mashanovich, Frederic Y Gardes, David J Thomson, Youfang Hu, Ke Li, Milos Nedeljkovic, J Soler Penades, Ali Z Khokhar, Colin J Mitchell, Stevan

Stankovic, et al. Silicon photonic waveguides and devices for near-and mid-ir applications. *IEEE J. Sel. Top. Quantum Electron.*, 21(4):8200112, 2015.

[69] Goran Z Mashanovich, Milan M Milošević, Milos Nedeljkovic, Nathan Owens, Boqian Xiong, Ee Jin Teo, and Youfang Hu. Low loss silicon waveguides for the mid-infrared. *Optics Express*, 19(8):7112–7119, 2011.

[70] Milan M Milosevic, Milos Nedeljkovic, Taha M Ben Masaud, Ehsan Jaberansary, Harold MH Chong, Neil G Emerson, Graham T Reed, and Goran Z Mashanovich. Silicon waveguides and devices for the mid-infrared. *Applied Physics Letters*, 101(12), 2012.

[71] Yu-Chi Chang, Vincent Paeder, Lubos Hvozdara, Jean-Michel Hartmann, and Hans Peter Herzig. Low-loss germanium strip waveguides on silicon for the mid-infrared. *Optics letters*, 37(14):2883–2885, 2012.

[72] JM Hartmann, A Abbadie, N Cherkashin, H Grampeix, and L Clavelier. Epitaxial growth of Ge thick layers on nominal and 6 off Si (0 0 1); Ge surface passivation by Si. *Semiconductor Science and Technology*, 24(5):055002, 2009.

[73] Gunther Roelkens, Utsav Dave, Alban Gassenq, Nannicha Hattasan, Chen Hu, Bart Kuyken, Francois Leo, Aditya Malik, Muhammad Muneeb, Eva Ryckeboer, et al. Silicon-based heterogeneous photonic integrated circuits for the mid-infrared. *Optical Materials Express*, 3(9):1523–1536, 2013.

[74] Aditya Singh Malik, Muhammad Muneeb, Yosuke Shimura, Joris Van Campenhout, Roger Loo, and Günther Roelkens. Germanium-on-silicon mid-infrared waveguides and Mach-Zehnder interferometers. In *IEEE Photonics Conference 2013 (IPC-2013)*, pages 104–105. IEEE, 2013.

[75] M Nedeljkovic, J Soler Penades, C Mitchell, A Khokhar, S Stankovic, T Dominguez Bucio, C Littlejohns, F Gardes, and G Mashanovich. Surface Grating Coupled Low Loss Ge-on-Si Rib Waveguides and Multimode Interferometers. 2015.

[76] Milos Nedeljkovic, Jordi Soler Penades, Vinita Mittal, Ganapathy Senthil Murugan, Ali Z Khokhar, Callum Littlejohns, Lewis G Carpenter, Corin BE Gawith, James S Wilkinson, and Goran Z Mashanovich. Germanium-on-silicon waveguides operating at mid-infrared wavelengths up to 8.5 μm. *Optics express*, 25(22):27431–27441, 2017.

[77] Saeed Khan, Jeff Chiles, Jichi Ma, and Sasan Fathpour. Silicon-on-nitride waveguides for mid-and near-infrared integrated photonics. *Applied Physics Letters*, 102(12):121104, 2013.

[78] Pao Tai Lin, Vivek Singh, Lionel Kimerling, and Anuradha Murthy Agarwal. Planar silicon nitride mid-infrared devices. *Applied Physics Letters*, 102(25):251121, 2013.

[79] Alexander Spott, Jon Peters, Michael L Davenport, Eric J Stanton, Charles D Merritt, William W Bewley, Igor Vurgaftman, Chul Soo Kim, Jerry R Meyer, Jeremy Kirch, et al. Quantum cascade laser on silicon. *Optica*, 3(5):545–551, 2016.

[80] Fangxin Li, Stuart D Jackson, Christian Grillet, Eric Magi, Darren Hudson, Steven J Madden, Yashodhan Moghe, Christopher O'Brien, Andrew Read, Steven G Duvall, et al. Low propagation loss silicon-on-sapphire waveguides for the mid-infrared. *Optics express*, 19(16):15212–15220, 2011.

[81] Tom Baehr-Jones, Alexander Spott, Rob Ilic, Andrew Spott, Boyan Penkov, William Asher, and Michael Hochberg. Silicon-on-sapphire integrated waveguides for the mid-infrared. *Optics express*, 18(12):12127–12135, 2010.

[82] Alexander Spott, Yang Liu, Tom Baehr-Jones, Rob Ilic, and Michael Hochberg. Silicon waveguides and ring resonators at 5.5 μ m. *Applied Physics Letters*, 97(21):213501, 2010.

[83] Fangxin Li, Stuart D Jackson, Christian Grillet, Eric Magi, Darren Hudson, Steven J Madden, Yashodhan Moghe, Christopher OBrien, Andrew Read, Steven G Duvall, et al. High quality waveguides for the mid-infrared wavelength range in a silicon-on-sapphire platform. *arXiv preprint arXiv:1705.10038*, 2017.

[84] J Soler Penades, Alejandro Ortega-Moñux, Milos Nedeljkovic, JG Wangüemert-Pérez, Robert Halir, AZ Khokhar, Carlos Alonso-Ramos, Zhibo Qu, Iñigo Molina-Fernández, Pavel Cheben, et al. Suspended silicon mid-infrared waveguide devices with subwavelength grating metamaterial cladding. *Optics express*, 24(20):22908–22916, 2016.

[85] J. Soler Penadés, A. Sánchez-Postigo, M. Nedeljkovic, A. Ortega-Mo nux, J. G. Wangüemert-Pérez, Y. Xu, R. Halir, Z. Qu, A. Z. Khokhar, A. Osman, W. Cao, C. G. Littlejohns, P. Cheben, I. Molina-Fernández, and G. Z. Mashanovich. Suspended silicon waveguides for long-wave infrared wavelengths. *Opt. Lett.*, 43(4):795–798, Feb 2018.

[86] Mickael Brun, Pierre Labeye, Gilles Grand, Jean-Michel Hartmann, Fahem Boulila, Mathieu Carras, and Sergio Nicoletti. Low loss sige graded index waveguides for mid-ir applications. *Optics express*, 22(1):508–518, 2014.

[87] JM Ramirez, Q Liu, V Vakarin, J Frigerio, A Ballabio, X Le Roux, D Bouville, L Vivien, G Isella, and D Marris-Morini. Graded SiGe waveguides with broadband low-loss propagation in the mid infrared. *Optics express*, 26(2):870–877, 2018.

[88] Yuanbo Zhang, Yan-Wen Tan, Horst L Stormer, and Philip Kim. Experimental observation of the quantum Hall effect and Berry's phase in graphene. *nature*, 438(7065):201, 2005.

[89] Kin Fai Mak, Changgu Lee, James Hone, Jie Shan, and Tony F Heinz. Atomically thin MoS_2: a new direct-gap semiconductor. *Physical review letters*, 105(13):136805, 2010.

[90] Andrea Splendiani, Liang Sun, Yuanbo Zhang, Tianshu Li, Jonghwan Kim, Chi-Yung Chim, Giulia Galli, and Feng Wang. Emerging photoluminescence in monolayer MoS_2. *Nano letters*, 10(4):1271–1275, 2010.

[91] Andre K Geim and Irina V Grigorieva. Van der Waals heterostructures. *Nature*, 499(7459):419–425, 2013.

[92] Goki Eda and Stefan A Maier. Two-dimensional crystals: managing light for optoelectronics. *Acs Nano*, 7(7):5660–5665, 2013.

[93] A Morita. Semiconducting black phosphorus. *Applied Physics A*, 39(4):227–242, 1986.

[94] Vy Tran, Ryan Soklaski, Yufeng Liang, and Li Yang. Layer-controlled band gap and anisotropic excitons in few-layer black phosphorus. *Physical Review B*, 89(23):235319, 2014.

[95] Yongzhe Zhang, Tao Liu, Bo Meng, Xiaohui Li, Guozhen Liang, Xiaonan Hu, and Qi Jie Wang. Broadband high photoresponse from pure monolayer graphene photodetector. *Nature communications*, 4:1811, 2013.

[96] L Vicarelli, MS Vitiello, D Coquillat, A Lombardo, AC Ferrari, W Knap, M Polini, V Pellegrini, and A Tredicucci. Graphene field-effect transistors as room-temperature terahertz detectors. *Nature materials*, 11(10):865–871, 2012.

[97] AB Kuzmenko, Erik Van Heumen, Fabrizio Carbone, and Dirk Van Der Marel. Universal optical conductance of graphite. *Physical review letters*, 100(11):117401, 2008.

[98] Steven J Koester and Mo Li. Waveguide-coupled graphene optoelectronics. *Selected Topics in Quantum Electronics, IEEE Journal of*, 20(1):84–94, 2014.

[99] ZQ Li, Eric A Henriksen, Z Jiang, Zhao Hao, Michael C Martin, P Kim, HL Stormer, and Dimitri N Basov. Dirac charge dynamics in graphene by infrared spectroscopy. *Nature Physics*, 4(7):532–535, 2008.

[100] Phaedon Avouris and Marcus Freitag. Graphene photonics, plasmonics, and optoelectronics. *Selected Topics in Quantum Electronics, IEEE Journal of*, 20(1):72–83, 2014.

[101] Phaedon Avouris. Graphene: electronic and photonic properties and devices. *Nano letters*, 10(11):4285–4294, 2010.

[102] Huan Li, Yoska Anugrah, Steven J Koester, and Mo Li. Optical absorption in graphene integrated on silicon waveguides. *Applied Physics Letters*, 101(11):111110, 2012.

[103] RR Nair, P Blake, AN Grigorenko, KS Novoselov, TJ Booth, T Stauber, NMR Peres, and AK Geim. Fine structure constant defines visual transparency of graphene. *Science*, 320(5881):1308–1308, 2008.

[104] Marco Bernardi, Maurizia Palummo, and Jeffrey C Grossman. Extraordinary sunlight absorption and one nanometer thick photovoltaics using two-dimensional monolayer materials. *Nano letters*, 13(8):3664–3670, 2013.

[105] J Li, S Majety, R Dahal, WP Zhao, JY Lin, and HX Jiang. Dielectric strength, optical absorption, and deep ultraviolet detectors of hexagonal boron nitride epilayers. *Applied Physics Letters*, 101(17):171112, 2012.

[106] Santanu Das, Moonkyung Kim, Jo-won Lee, and Wonbong Choi. Synthesis, properties, and applications of 2-D materials: a comprehensive review. *Critical Reviews in Solid State and Materials Sciences*, 39(4):231–252, 2014.

[107] William S Hummers Jr and Richard E Offeman. Preparation of graphitic oxide. *Journal of the american chemical society*, 80(6):1339–1339, 1958.

[108] Inhwa Jung, Matthew Pelton, Richard Piner, Dmitriy A Dikin, Sasha Stankovich, Supinda Watcharotone, Martina Hausner, and Rodney S Ruoff. Simple approach for high-contrast optical imaging and characterization of graphene-based sheets. *Nano Letters*, 7(12):3569–3575, 2007.

[109] AN Obraztsov, EA Obraztsova, AV Tyurnina, and AA Zolotukhin. Chemical vapor deposition of thin graphite films of nanometer thickness. *Carbon*, 45(10):2017–2021, 2007.

[110] Xuesong Li, Carl W Magnuson, Archana Venugopal, Rudolf M Tromp, James B Hannon, Eric M Vogel, Luigi Colombo, and Rodney S Ruoff. Large-area graphene single crystals grown by low-pressure chemical vapor deposition of methane on copper. *Journal of the American Chemical Society*, 133(9):2816–2819, 2011.

[111] Zhengzong Sun, Zheng Yan, Jun Yao, Elvira Beitler, Yu Zhu, and James M Tour. Growth of graphene from solid carbon sources. *Nature*, 468(7323):549, 2010.

[112] Abdeladim Guermoune, Tarun Chari, Filip Popescu, Shadi S Sabri, Jonathan Guillemette, Helgi S Skulason, Thomas Szkopek, and Mohamed Siaj. Chemical vapor deposition synthesis of graphene on copper with methanol, ethanol, and propanol precursors. *Carbon*, 49(13):4204–4210, 2011.

[113] Y Gamo, A Nagashima, M Wakabayashi, M Terai, and C Oshima. Atomic structure of monolayer graphite formed on Ni (111). *Surface Science*, 374(1):61–64, 1997.

[114] Hirokazu Ueta, Morihiko Saida, Chikara Nakai, Yoichi Yamada, Masahiro Sasaki, and Shigehiko Yamamoto. Highly oriented monolayer graphite formation on Pt (1 1 1) by a supersonic methane beam. *Surface science*, 560(1-3):183–190, 2004.

[115] S Marchini, S Günther, and J Wintterlin. Scanning tunneling microscopy of graphene on Ru (0001). *Physical Review B*, 76(7):075429, 2007.

[116] Rebecca S Edwards and Karl S Coleman. Graphene film growth on polycrystalline metals. *Accounts of chemical research*, 46(1):23–30, 2012.

[117] Sukang Bae, Hyeongkeun Kim, Youngbin Lee, Xiangfan Xu, Jae-Sung Park, Yi Zheng, Jayakumar Balakrishnan, Tian Lei, Hye Ri Kim, Young Il Song, et al. Roll-to-roll production of 30-inch graphene films for transparent electrodes. *Nature nanotechnology*, 5(8):574–578, 2010.

[118] George Vakerlis, Ward D Halverson, Diwakar Garg, and Paul N Dyer. Radio frequency plasma enhanced chemical vapor deposition process and reactor, 1991. US Patent 5,052,339.

[119] Claire Berger, Zhimin Song, Tianbo Li, Xuebin Li, Asmerom Y Ogbazghi, Rui Feng, Zhenting Dai, Alexei N Marchenkov, Edward H Conrad, Phillip N First, et al. Ultrathin epitaxial graphite: 2D electron gas properties and a route toward graphene-based nanoelectronics. *The Journal of Physical Chemistry B*, 108(52):19912–19916, 2004.

[120] Chuhei Oshima and Ayato Nagashima. Ultra-thin epitaxial films of graphite and hexagonal boron nitride on solid surfaces. *Journal of Physics: Condensed Matter*, 9(1):1, 1997.

[121] Ch Riedl, C Coletti, T Iwasaki, AA Zakharov, and U Starke. Quasi-free-standing epitaxial graphene on SiC obtained by hydrogen intercalation. *Physical review letters*, 103(24):246804, 2009.

[122] Joshua D Caldwell, Travis J Anderson, James C Culbertson, Glenn G Jernigan, Karl D Hobart, Fritz J Kub, Marko J Tadjer, Joseph L Tedesco, Jennifer K Hite, Michael A Mastro, et al. Technique for the dry transfer of epitaxial graphene onto arbitrary substrates. *ACS nano*, 4(2):1108–1114, 2010.

[123] Sakulsuk Unarunotai, Yuya Murata, Cesar E Chialvo, Hoon-sik Kim, Scott MacLaren, Nadya Mason, Ivan Petrov, and John A Rogers. Transfer of graphene layers grown on SiC wafers to other substrates and their integration into field effect transistors. *Applied Physics Letters*, 95(20):202101.

[124] Md. Sajibul Alam Bhuyan, Md. Nizam Uddin, Md. Maksudul Islam, Ferdaushi Alam Bipasha, and Sayed Shafayat Hossain. Synthesis of graphene. *International Nano Letters*, 6(2):65–83, Jun 2016.

[125] Athanasios B Bourlinos, Vasilios Georgakilas, Radek Zboril, Theodore A Steriotis, and Athanasios K Stubos. Liquid-phase exfoliation of graphite towards solubilized graphenes. *small*, 5(16):1841–1845, 2009.

[126] Yenny Hernandez, Valeria Nicolosi, Mustafa Lotya, Fiona M Blighe, Zhenyu Sun, Sukanta De, IT McGovern, Brendan Holland, Michele Byrne, Yurii K Gun'Ko, et al. High-yield production of graphene by liquid-phase exfoliation of graphite. *Nature nanotechnology*, 3(9):563–568, 2008.

[127] Na Liu, Fang Luo, Haoxi Wu, Yinghui Liu, Chao Zhang, and Ji Chen. One-step ionic-liquid-assisted electrochemical synthesis of ionic-liquid-functionalized graphene sheets directly from graphite. *Advanced Functional Materials*, 18(10):1518–1525, 2008.

[128] Natnael Behabtu, Jay R Lomeda, Micah J Green, Amanda L Higginbotham, Alexander Sinitskii, Dmitry V Kosynkin, Dmitri Tsentalovich, A Nicholas G Parra-Vasquez, Judith Schmidt, Ellina Kesselman, et al. Spontaneous high-concentration dispersions and liquid crystals of graphene. *Nature nanotechnology*, 5(6):406, 2010.

[129] Weixia Zhang, Jiecheng Cui, Cheng-an Tao, Yiguang Wu, Zhanping Li, Li Ma, Yuquan Wen, and Guangtao Li. A strategy for producing pure single-layer graphene sheets based on a confined self-assembly approach. *Angewandte Chemie*, 121(32):5978–5982, 2009.

[130] Alexander E Karu and Michael Beer. Pyrolytic formation of highly crystalline graphite films. *Journal of Applied Physics*, 37(5):2179–2181, 1966.

[131] Alfonso Reina, Xiaoting Jia, John Ho, Daniel Nezich, Hyungbin Son, Vladimir Bulovic, Mildred S Dresselhaus, and Jing Kong. Large area, few-layer graphene films on arbitrary substrates by chemical vapor deposition. *Nano letters*, 9(1):30–35, 2008.

[132] Alexander Mattausch and Oleg Pankratov. Density functional study of graphene overlayers on SiC. *physica status solidi (b)*, 245(7):1425–1435, 2008.

[133] ZH Ni, W Chen, XF Fan, JL Kuo, T Yu, ATS Wee, and ZX Shen. Raman spectroscopy of epitaxial graphene on a SiC substrate. *Physical Review B*, 77(11):115416, 2008.

[134] M Sprinkle, P Soukiassian, WA De Heer, C Berger, and EH Conrad. Epitaxial graphene: the material for graphene electronics. *physica status solidi (RRL)–Rapid Research Letters*, 3(6):A91–A94, 2009.

[135] Dmitry V Kosynkin, Amanda L Higginbotham, Alexander Sinitskii, Jay R Lomeda, Ayrat Dimiev, B Katherine Price, and James M Tour. Longitudinal unzipping of carbon nanotubes to form graphene nanoribbons. *Nature*, 458(7240):872, 2009.

[136] Liying Jiao, Li Zhang, Xinran Wang, Georgi Diankov, and Hongjie Dai. Narrow graphene nanoribbons from carbon nanotubes. *Nature*, 458(7240):877, 2009.

[137] Marcus Freitag, Tony Low, Fengnian Xia, and Phaedon Avouris. Photoconductivity of biased graphene. *Nature Photonics*, 7(1):53–59, 2013.

[138] Damon B Farmer, Roksana Golizadeh-Mojarad, Vasili Perebeinos, Yu-Ming Lin, George S Tulevski, James C Tsang, and Phaedon Avouris. Chemical doping and electron- hole conduction asymmetry in graphene devices. *Nano letters*, 9(1):388–392, 2008.

[139] Max C Lemme, Frank HL Koppens, Abram L Falk, Mark S Rudner, Hongkun Park, Leonid S Levitov, and Charles M Marcus. Gate-activated photoresponse in a graphene p-n junction. *Nano letters*, 11(10):4134–4137, 2011.

[140] Eva C Peters, Eduardo JH Lee, Marko Burghard, and Klaus Kern. Gate dependent photocurrents at a graphene p-n junction. *Applied Physics Letters*, 97(19):193102, 2010.

[141] Gayathri Rao, Marcus Freitag, Hsin-Ying Chiu, Ravi S Sundaram, and Phaedon Avouris. Raman and photocurrent imaging of electrical stress-induced p-n junctions in graphene. *ACS nano*, 5(7):5848–5854, 2011.

[142] T Mueller, F Xia, M Freitag, J Tsang, Ph Avouris, et al. Role of contacts in graphene transistors: A scanning photocurrent study. *Physical Review B*, 79(24):245430, 2009.

[143] FHL Koppens, T Mueller, Ph Avouris, AC Ferrari, MS Vitiello, and M Polini. Photodetectors based on graphene, other two-dimensional materials and hybrid systems. *Nature nanotechnology*, 9(10):780, 2014.

[144] Jinhua Li, Liyong Niu, Zijian Zheng, and Feng Yan. Photosensitive graphene transistors. *Advanced Materials*, 26(31):5239–5273, 2014.

[145] Fengnian Xia, Thomas Mueller, Yuming Lin, Alberto Valdes-Garcia, and Phaedon Avouris. Ultrafast graphene photodetector. *Nature nanotechnology*, 4(12):839–843, 2009.

[146] Xiaodong Xu, Nathaniel M Gabor, Jonathan S Alden, Arend M van der Zande, and Paul L McEuen. Photo-thermoelectric effect at a graphene interface junction. *Nano letters*, 10(2):562–566, 2009.

[147] Nathaniel M Gabor, Justin CW Song, Qiong Ma, Nityan L Nair, Thiti Taychatanapat, Kenji Watanabe, Takashi Taniguchi, Leonid S Levitov, and Pablo Jarillo-Herrero. Hot carrier-assisted intrinsic photoresponse in graphene. *Science*, 334(6056):648–652, 2011.

[148] Justin CW Song, Mark S Rudner, Charles M Marcus, and Leonid S Levitov. Hot carrier transport and photocurrent response in graphene. *Nano letters*, 11(11):4688–4692, 2011.

[149] Dong Sun, Grant Aivazian, Aaron M Jones, Jason S Ross, Wang Yao, David Cobden, and Xiaodong Xu. Ultrafast hot-carrier-dominated photocurrent in graphene. *Nature nanotechnology*, 7(2):114–118, 2012.

[150] Valeri N Kotov, Bruno Uchoa, Vitor M Pereira, F Guinea, and AH Castro Neto. Electron-electron interactions in graphene: Current status and perspectives. *Reviews of Modern Physics*, 84(3):1067, 2012.

[151] Jens Christian Johannsen, Søren Ulstrup, Federico Cilento, Alberto Crepaldi, Michele Zacchigna, Cephise Cacho, IC Edmond Turcu, Emma Springate, Felix Fromm, Christian Raidel, et al. Direct view of hot carrier dynamics in graphene. *Physical review letters*, 111(2):027403, 2013.

[152] Michele Lazzeri, S Piscanec, Francesco Mauri, AC Ferrari, and J Robertson. Electron transport and hot phonons in carbon nanotubes. *Physical review letters*, 95(23):236802, 2005.

[153] Xinghan Cai, Andrei B Sushkov, Ryan J Suess, Mohammad M Jadidi, Gregory S Jenkins, Luke O Nyakiti, Rachael L Myers-Ward, Shanshan Li, Jun Yan, D Kurt Gaskill, et al. Sensitive room-temperature terahertz detection via the photothermoelectric effect in graphene. *Nature nanotechnology*, 9(10):814, 2014.

[154] PL Richards. Bolometers for infrared and millimeter waves. *Journal of Applied Physics*, 76(1):1–24, 1994.

[155] Mikhail Dyakonov and Michael Shur. Detection, mixing, and frequency multiplication of terahertz radiation by two-dimensional electronic fluid. *Electron Devices, IEEE Transactions on*, 43(3):380–387, 1996.

[156] Gerasimos Konstantatos, Michela Badioli, Louis Gaudreau, Johann Osmond, Maria Bernechea, F Pelayo Garcia de Arquer, Fabio Gatti, and Frank HL Koppens. Hybrid graphene-quantum dot phototransistors with ultrahigh gain. *Nature nanotechnology*, 7(6):363–368, 2012.

[157] Youngbin Lee, Jeong Kwon, Euyheon Hwang, Chang-Ho Ra, Won Jong Yoo, Jong-Hyun Ahn, Jong Hyeok Park, and Jeong Ho Cho. High-performance perovskite–graphene hybrid photodetector. *Advanced Materials*, 27(1):41–46, 2015.

[158] Yuanda Liu, Fengqiu Wang, Xiaomu Wang, Xizhang Wang, Emmanuel Flahaut, Xiaolong Liu, Yao Li, Xinran Wang, Yongbing Xu, Yi Shi, et al. Planar carbon nanotube–graphene hybrid films for high-performance broadband photodetectors. *Nature communications*, 6:8589, 2015.

[159] Dayong Zhang, Lin Gan, Yang Cao, Qing Wang, Limin Qi, and Xuefeng Guo. Understanding Charge Transfer at PbS-Decorated Graphene Surfaces toward a Tunable Photosensor. *Advanced Materials*, 24(20):2715–2720, 2012.

[160] Zhenhua Sun, Zhike Liu, Jinhua Li, Guo-an Tai, Shu-Ping Lau, and Feng Yan. Infrared photodetectors based on CVD-grown graphene and PbS quantum dots with ultrahigh responsivity. *Advanced materials*, 24(43):5878–5883, 2012.

[161] TJ Echtermeyer, L Britnell, PK Jasnos, A Lombardo, RV Gorbachev, AN Grigorenko, AK Geim, AC Ferrari, and KS Novoselov. Strong plasmonic enhancement of photovoltage in graphene. *Nature communications*, 2:458, 2011.

[162] Yuan Liu, Rui Cheng, Lei Liao, Hailong Zhou, Jingwei Bai, Gang Liu, Lixin Liu, Yu Huang, and Xiangfeng Duan. Plasmon resonance enhanced multicolour photodetection by graphene. *Nature communications*, 2:579, 2011.

[163] Thomas Mueller, Fengnian Xia, and Phaedon Avouris. Graphene photodetectors for high-speed optical communications. *Nature Photonics*, 4(5):297–301, 2010.

[164] Michael Engel, Mathias Steiner, Antonio Lombardo, Andrea C Ferrari, Hilbert v Löhneysen, Phaedon Avouris, and Ralph Krupke. Light–matter interaction in a microcavity-controlled graphene transistor. *Nature communications*, 3:906, 2012.

[165] Andreas Pospischil, Markus Humer, Marco M Furchi, Dominic Bachmann, Romain Guider, Thomas Fromherz, and Thomas Mueller. Cmos-compatible graphene photodetector covering all optical communication bands. *Nature Photonics*, 7(11):892–896, 2013.

[166] Xuetao Gan, Ren-Jye Shiue, Yuanda Gao, Inanc Meric, Tony F Heinz, Kenneth Shepard, James Hone, Solomon Assefa, and Dirk Englund. Chip-integrated ultrafast graphene photodetector with high responsivity. *Nature Photonics*, 7(11):883–887, 2013.

[167] Jan Mertens, Anna L Eiden, Daniel O Sigle, Fumin Huang, Antonio Lombardo, Zhipei Sun, Ravi S Sundaram, Alan Colli, Christos Tserkezis, Javier Aizpurua, et al. Controlling subnanometer gaps in plasmonic dimers using graphene. *Nano letters*, 13(11):5033–5038, 2013.

[168] Marcus Freitag, Tony Low, Wenjuan Zhu, Hugen Yan, Fengnian Xia, and Phaedon Avouris. Photocurrent in graphene harnessed by tunable intrinsic plasmons. *Nature communications*, 4:1951, 2013.

[169] Chun-Chung Chen, Mehmet Aykol, Chia-Chi Chang, AFJ Levi, and Stephen B Cronin. Graphene-silicon Schottky diodes. *Nano letters*, 11(5):1863–1867, 2011.

[170] Xinming Li, Hongwei Zhu, Kunlin Wang, Anyuan Cao, Jinquan Wei, Chunyan Li, Yi Jia, Zhen Li, Xiao Li, and Dehai Wu. Graphene-on-silicon Schottky junction solar cells. *Advanced Materials*, 22(25):2743–2748, 2010.

[171] Xiaohong An, Fangze Liu, Yung Joon Jung, and Swastik Kar. Tunable graphene-silicon heterojunctions for ultrasensitive photodetection. *Nano letters*, 13(3):909–916, 2013.

[172] Xiaomu Wang, Zhenzhou Cheng, Ke Xu, Hon Ki Tsang, and Jian-Bin Xu. High-responsivity graphene/silicon-heterostructure waveguide photodetectors. *Nature Photonics*, 7(11):888–891, 2013.

[173] Ilya Goykhman, Ugo Sassi, Boris Desiatov, Noa Mazurski, Silvia Milana, Domenico De Fazio, Anna Eiden, Jacob Khurgin, Joseph Shappir, Uriel Levy, et al. On-Chip Integrated, Silicon-Graphene Plasmonic Schottky Photodetector with High Responsivity and Avalanche Photogain. *Nano letters*, 16(5):3005–3013, 2016.

[174] Victor Ryzhii. The theory of quantum-dot infrared phototransistors. *Semiconductor science and technology*, 11(5):759, 1996.

[175] Mary A Rowe, EJ Gansen, Marion Greene, RH Hadfield, TE Harvey, MY Su, Sae Woo Nam, RP Mirin, and D Rosenberg. Single-photon detection using a quantum dot optically gated field-effect transistor with high internal quantum efficiency. *Applied physics letters*, 89(25):253505, 2006.

[176] Jun Yan, Mann Ho Kim, Jennifer A Elle, Andrei B Sushkov, Greg S Jenkins, Howard M Milchberg, Michael S Fuhrer, and HD Drew. Dual-gated bilayer graphene hot-electron bolometer. *Nature nanotechnology*, 7(7):472–478, 2012.

[177] Heli Vora, Piranavan Kumaravadivel, Bent Nielsen, and Xu Du. Bolometric response in graphene based superconducting tunnel junctions. *Applied Physics Letters*, 100(15):153507, 2012.

[178] Kin Chung Fong and KC Schwab. Ultrasensitive and wide-bandwidth thermal measurements of graphene at low temperatures. *Physical Review X*, 2(3):031006, 2012.

[179] Davide Spirito, Dominique Coquillat, Sergio L De Bonis, Antonio Lombardo, Matteo Bruna, Andrea C Ferrari, Vittorio Pellegrini, Alessandro Tredicucci, Wojciech Knap, and Miriam S Vitiello. High performance bilayer-graphene terahertz detectors. *Applied Physics Letters*, 104(6):061111, 2014.

[180] Martin Mittendorff, Stephan Winnerl, Josef Kamann, Jonathan Eroms, Dieter Weiss, Harald Schneider, and Manfred Helm. Ultrafast graphene-based broadband THz detector. *Applied Physics Letters*, 103(2):021113, 2013.

[181] Sarah Riazimehr, Daniel Schneider, Chanyoung Yim, Satender Kataria, Vikram Passi, Andreas Bablich, Georg S Duesberg, and Max C Lemme. Spectral sensitivity of a graphene/silicon pn-junction photodetector. In *Ultimate Integration on Silicon (EUROSOI-ULIS), 2015 Joint International EUROSOI Workshop and International Conference on*, pages 77–80. IEEE, 2015.

[182] Kun Xu, Chen Xu, Yiyang Xie, Jun Deng, Yanxu Zhu, Weiling Guo, Meng Xun, Kenneth BK Teo, Hongda Chen, and Jie Sun. Graphene GaN-based Schottky ultraviolet detectors. *IEEE Transactions on Electron Devices*, 62(9):2802–2808, 2015.

[183] Marcus Freitag, Tony Low, and Phaedon Avouris. Increased responsivity of suspended graphene photodetectors. *Nano letters*, 13(4):1644–1648, 2013.

[184] Oriol Lopez-Sanchez, Dominik Lembke, Metin Kayci, Aleksandra Radenovic, and Andras Kis. Ultrasensitive photodetectors based on monolayer MoS_2. *Nature nanotechnology*, 8(7):497, 2013.

[185] Michael A Krainak, Xiaoli Sun, Guangning Yang, and Wei Lu. Comparison of linear-mode avalanche photodiode lidar receivers for use at one-micron wavelength. In *Advanced Photon Counting Techniques IV*, volume 7681, page 76810Y. International Society for Optics and Photonics, 2010.

[186] Wenjing Zhang, Jing-Kai Huang, Chang-Hsiao Chen, Yung-Huang Chang, Yuh-Jen Cheng, and Lain-Jong Li. High-gain phototransistors based on a CVD MoS_2 monolayer. *Advanced materials*, 25(25):3456–3461, 2013.

[187] Andreas Pospischil, Marco M Furchi, and Thomas Mueller. Solar-energy conversion and light emission in an atomic monolayer pn diode. *Nature nanotechnology*, 9(4):257–261, 2014.

[188] Marco M Furchi, Andreas Pospischil, Florian Libisch, Joachim Burgdorfer, and Thomas Mueller. Photovoltaic effect in an electrically tunable van der Waals heterojunction. *Nano letters*, 14(8):4785–4791, 2014.

[189] Chul-Ho Lee, Gwan-Hyoung Lee, Arend M Van Der Zande, Wenchao Chen, Yilei Li, Minyong Han, Xu Cui, Ghidewon Arefe, Colin Nuckolls, Tony F Heinz, et al. Atomically thin p-n junctions with van der Waals heterointerfaces. *Nature nanotechnology*, 9(9):676, 2014.

[190] Zhenxing Wang, Kai Xu, Yuanchang Li, Xueying Zhan, Muhammad Safdar, Qisheng Wang, Fengmei Wang, and Jun He. Role of Ga vacancy on a multilayer GaTe phototransistor. *ACS nano*, 8(5):4859–4865, 2014.

[191] Líam Britnell, RM Ribeiro, A Eckmann, R Jalil, BD Belle, A Mishchenko, Y-J Kim, RV Gorbachev, T Georgiou, SV Morozov, et al. Strong light-matter interactions in heterostructures of atomically thin films. *Science*, 340(6138):1311–1314, 2013.

[192] Chanyoung Yim, Maria O'brien, Niall McEvoy, Sarah Riazimehr, Heiko Schäfer-Eberwein, Andreas Bablich, Ravinder Pawar, Giuseppe Iannaccone, Clive Downing, Gianluca Fiori, et al. Heterojunction hybrid devices from vapor phase grown MoS_2. *Scientific reports*, 4:5458, 2014.

[193] Wenjing Zhang, Chih-Piao Chuu, Jing-Kai Huang, Chang-Hsiao Chen, Meng-Lin Tsai, Yung-Huang Chang, Chi-Te Liang, Yu-Ze Chen, Yu-Lun Chueh, Jr-Hau He, et al. Ultrahigh-gain photodetectors based on atomically thin graphene-MoS_2 heterostructures. *Scientific reports*, 4:3826, 2014.

[194] Yimin Kang, Han-Din Liu, Mike Morse, Mario J Paniccia, Moshe Zadka, Stas Litski, Gadi Sarid, Alexandre Pauchard, Ying-Hao Kuo, Hui-Wen Chen, et al. Monolithic germanium/silicon avalanche photodiodes with 340 GHz gain–bandwidth product. *Nature photonics*, 3(1):59, 2009.

[195] Daniel Schall, Daniel Neumaier, Muhammad Mohsin, Bartos Chmielak, Jens Bolten, Caroline Porschatis, Andreas Prinzen, Christopher Matheisen, Wolfgang Kuebart, Bernhard Junginger, et al. 50 GBit/s photodetectors based on wafer-scale graphene for integrated silicon photonic communication systems. *Acs Photonics*, 1(9):781–784, 2014.

[196] Nathan Youngblood, Che Chen, Steven J Koester, and Mo Li. Waveguide-integrated black phosphorus photodetector with high responsivity and low dark current. *Nature Photonics*, 9(4):247, 2015.

[197] Alexander Urich, Karl Unterrainer, and Thomas Mueller. Intrinsic response time of graphene photodetectors. *Nano letters*, 11(7):2804–2808, 2011.

[198] Mathieu Massicotte, Peter Schmidt, Fabien Vialla, Kevin G Schädler, Antoine Reserbat-Plantey, Kenji Watanabe, Takashi Taniguchi, Klaas-Jan Tielrooij, and Frank HL Koppens. Picosecond photoresponse in van der Waals heterostructures. *Nature nanotechnology*, 11(1):42, 2016.

[199] Jiaqi He, Nardeep Kumar, Matthew Z Bellus, Hsin-Ying Chiu, Dawei He, Yongsheng Wang, and Hui Zhao. Electron transfer and coupling in graphene–tungsten disulfide van der Waals heterostructures. *Nature communications*, 5:5622, 2014.

[200] Jie Mao, Yongqiang Yu, Liu Wang, Xiujuan Zhang, Yuming Wang, Zhibin Shao, and Jiansheng Jie. Ultrafast, broadband photodetector based on $MoSe_2$/silicon heterojunction with vertically standing layered structure using graphene as transparent electrode. *Advanced Science*, 3(11):1600018, 2016.

[201] Mingsheng Long, Erfu Liu, Peng Wang, Anyuan Gao, Hui Xia, Wei Luo, Baigeng Wang, Junwen Zeng, Yajun Fu, Kang Xu, et al. Broadband photovoltaic detectors based on an atomically thin heterostructure. *Nano letters*, 16(4):2254–2259, 2016.

[202] Dominik Kufer, Ivan Nikitskiy, Tania Lasanta, Gabriele Navickaite, Frank HL Koppens, and Gerasimos Konstantatos. Hybrid 2D–0D MoS_2–PbS quantum dot photodetectors. *Advanced materials*, 27(1):176–180, 2015.

[203] Po-Han Chang, Chia-Shuo Li, Fang-Yu Fu, Kuo-You Huang, Ang-Sheng Chou, and Chih-I Wu. Ultrasensitive Photoresponsive Devices Based on Graphene/BiI_3 van der Waals Epitaxial Heterostructures. *Advanced Functional Materials*, 28(23):1800179, 2018.

[204] Wenjing Zhang, Ming-Hui Chiu, Chang-Hsiao Chen, Wei Chen, Lain-Jong Li, and Andrew Thye Shen Wee. Role of metal contacts in high-performance phototransistors based on WSe_2 monolayers. *ACS nano*, 8(8):8653–8661, 2014.

[205] Feng Wang, Zhenxing Wang, Kai Xu, Fengmei Wang, Qisheng Wang, Yun Huang, Lei Yin, and Jun He. Tunable GaTe-MoS_2 van der Waals p–n junctions with novel optoelectronic performance. *Nano letters*, 15(11):7558–7566, 2015.

[206] Jing Wu, Gavin Kok Wai Koon, Du Xiang, Cheng Han, Chee Tat Toh, Eeshan S Kulkarni, Ivan Verzhbitskiy, Alexandra Carvalho, Aleksandr S Rodin, Steven P Koenig, et al. Colossal ultraviolet photoresponsivity of few-layer black phosphorus. *ACS nano*, 9(8):8070–8077, 2015.

[207] Kiran Kumar Manga, Junzhong Wang, Ming Lin, Jie Zhang, Milos Nesladek, Venkatram Nalla, Wei Ji, and Kian Ping Loh. High-performance broadband photodetector using solution-processible PbSe–TiO_2–graphene hybrids. *Advanced materials*, 24(13):1697–1702, 2012.

[208] Anyuan Gao, Erfu Liu, Mingsheng Long, Wei Zhou, Yiyan Wang, Tianlong Xia, Weida Hu, Baigeng Wang, and Feng Miao. Gate-tunable rectification inversion and photovoltaic detection in graphene/WSe_2 heterostructures. *Applied Physics Letters*, 108(22):223501, 2016.

[209] Photon Design. Fimmwave. `https://http://www.photondesign.com./products/fimmwave.htm/`, 2019. Accessed: 01/03/2019.

[210] Lumerical. Product Overview. `https://www.lumerical.com/products/`, 2019. Accessed: 01/03/2019.

[211] Tanner EDA. L-edit. `https://www.mentor.com/tannereda/photonics/`, 2018. Accessed: 31/12/2018.

[212] Genisys-gmbh. BEAMER. `https://genisys-gmbh.com/beamer.html/`, 2019. Accessed: 12/01/2019.

[213] Oxford Instruments. Inductively Coupled Plasma (*ICP*) Etch. `https://plasma.oxinst.com/campaigns/technology/icp`, 2018. Accessed: 03/08/2018.

[214] Milos Nedeljković. *Silicon photonic modulators for the mid-infrared.* PhD thesis, University of Southampton, Physical Sciences and Engineering, 2013.

[215] DRS Daylight Solutions. Mid-IR Laser. `https://live-daylight-solutions.pantheonsite.io/products/`, 2018. Accessed: 03/08/2018.

[216] Inc. InfraRed Associates. HgCdTe (MCT) Detectors. `https://http://irassociates.com/index.php?page=hgcdte/`, 2018. Accessed: 03/08/2018.

[217] Vigo System S.A. Infrared Detectors. `https://www.vigo.com.pl/products/infrared-detectors/Photovoltaic-Detectors/pv-4te-series`, 2018. Accessed: 03/08/2018.

[218] Thorlabs. Mid-Infrared Optical Fibre . `https://www.thorlabs.com/newgrouppage9.cfm?objectgroup_id=7062#ad-image-0/`, 2019. Accessed: 19/04/2019.

[219] Ametek. 7265 Dual Phase DSP Lock-in Amplifier . `https://www.ameteksi.com/products/lock-in-amplifiers/7265-dual-phase-lock-in-amplifier/`, 2019. Accessed: 19/01/2019.

[220] Goran Z Mashanovich, Frederic Y Gardes, David J Thomson, Youfang Hu, Ke Li, Milos Nedeljkovic, Jordi Soler Penades, Ali Z Khokhar, Colin J Mitchell, Stevan Stankovic, et al. Silicon photonic waveguides and devices for near-and mid-IR applications. *IEEE Journal of Selected Topics in Quantum Electronics*, 21(4):407–418, 2014.

[221] J Soler Penadés, C Alonso-Ramos, AZ Khokhar, M Nedeljkovic, LA Boodhoo, A Ortega-Moñux, I Molina-Fernández, P Cheben, and GZ Mashanovich. Suspended SOI waveguide with sub-wavelength grating cladding for mid-infrared. *Optics letters*, 39(19):5661–5664, 2014.

[222] Lorenzo Pavesi and David J Lockwood. *Silicon photonics*, volume 1. Springer Science & Business Media, 2004.

[223] Jordi Soler Penades. *Group IV Mid-Infrared Devices for Sensing.* PhD thesis, University of Southampton, Physical Sciences and Engineering, 2017.

[224] Modeling methodology Lumerical Application Gallery. Graphene Modeling methodology . `https://apps.lumerical.com/other_application_graphene_simulation_tips.html/`, 2019. Accessed: 19/01/2019.

[225] Yongle Wu, Meijun Qu, and Yuanan Liu. A generalized lossy transmission-line model for tunable graphene-based transmission lines with attenuation phenomenon. *Scientific reports*, 6:31760, 2016.

[226] Ali Farmani, Abbas Zarifkar, Mohammad H Sheikhi, and Mehdi Miri. Design of a tunable graphene plasmonic-on-white graphene switch at infrared range. *Superlattices and Microstructures*, 112:404–414, 2017.

[227] George W Hanson. Dyadic Green's functions and guided surface waves for a surface conductivity model of graphene. *Journal of Applied Physics*, 103(6):064302, 2008.

[228] LA Falkovsky. Optical properties of graphene. In *Journal of Physics: Conference Series*, volume 129, page 012004. IOP Publishing, 2008.

[229] Xuesong Li, Yanwu Zhu, Weiwei Cai, Mark Borysiak, Boyang Han, David Chen, Richard D Piner, Luigi Colombo, and Rodney S Ruoff. Transfer of large-area graphene films for high-performance transparent conductive electrodes. *Nano letters*, 9(12):4359–4363, 2009.

[230] Renishaw. Raman products. `https://www.renishaw.com/en/raman-products--25893?gclid=CjwKCAjwtajrBRBVEiwA8w2Q8K-MVVInCbu2nOl7Vlsa5zAAhvOicvw8j-waMo8DyHqMSK_XTk7AXhoCrWkQAvD_BwE//`, 2019. Accessed: 31/08/2019.

[231] Andrea C Ferrari. Raman spectroscopy of graphene and graphite: disorder, electron–phonon coupling, doping and nonadiabatic effects. *Solid state communications*, 143(1-2):47–57, 2007.

[232] R Saito, M Hofmann, G Dresselhaus, A Jorio, and MS Dresselhaus. Raman spectroscopy of graphene and carbon nanotubes. *Advances in Physics*, 60(3):413–550.

[233] F Tuinstra and J Lo Koenig. Raman spectrum of graphite. *The Journal of Chemical Physics*, 53(3):1126–1130, 1970.

[234] Jian-Hao Chen, WG Cullen, C Jang, MS Fuhrer, and ED Williams. Defect scattering in graphene. *Physical review letters*, 102(23):236805, 2009.

[235] Mildred S Dresselhaus, Ado Jorio, Mario Hofmann, Gene Dresselhaus, and Riichiro Saito. Perspectives on carbon nanotubes and graphene raman spectroscopy. *Nano letters*, 10(3):751–758, 2010.

[236] Oxford Instruments. PlasmaPro 800 RIE. `https://plasma.oxinst.com/products/rie/plasmapro-800/`, 2018. Accessed: 03/08/2018.

[237] JEOL. JSM-7500F Field Emission Scanning Electron Microscope. `https://www.jeol.co.jp/en/products/detail/JSM-7500F.html//`, 2019. Accessed: 19/04/2019.

[238] Kosuke Nagashio, Tomonori Nishimura, Koji Kita, and Akira Toriumi. Systematic investigation of the intrinsic channel properties and contact resistance of monolayer and multilayer graphene field-effect transistor. *Japanese Journal of Applied Physics*, 49(5R):051304, 2010.

[239] Oxford Instruments. Inductively Coupled Plasma (*ICP*) Etch. `https://plasma.oxinst.com/products/pecvd/`, 2018. Accessed: 03/08/2018.

[240] ZEISS. Focused Ion Beam Scanning Electron Microscopes. `https://www.zeiss.com/microscopy/int/products/fib-sem-instruments.html/`, 2019. Accessed: 19/04/2019.

[241] Axus Technology. POLI-500 CMP Tool . `http://www.axustech.com/poli-500-cmp-tool/`, 2019. Accessed: 19/01/2019.

[242] Thorlabs. Fiber Optic L-Bracket Mating Sleeves . `https://www.thorlabs.com/newgrouppage9.cfm?objectgroup_id=6775/`, 2019. Accessed: 19/01/2019.

[243] Thorlabs. Digital Handheld Optical Power and Energy Meter Console . `https://www.thorlabs.com/newgrouppage9.cfm?objectgroup_id=3341/`, 2019. Accessed: 19/01/2019.

[244] Thorlabs. IR Reflective ND Filters . `https://www.thorlabs.com/newgrouppage9.cfm?objectgroup_id=6007/`, 2019. Accessed: 19/01/2019.

[245] Yu Yao, Raji Shankar, Patrick Rauter, Yi Song, Jing Kong, Marko Loncar, and Federico Capasso. High-responsivity mid-infrared graphene detectors with antenna-enhanced photocarrier generation and collection. *Nano letters*, 14(7):3749–3754, 2014.

[246] Thorlabs. Quantum Cascade Lasers (QCLs), 4.05 - 11 μm. `https://www.thorlabs.com/newgrouppage9.cfm?objectgroup_id=6932/`, 2019. Accessed: 19/04/2019.

[247] SelenOptics. Mid Infrared Optical Fibers. `https://http://www.selenoptics.com//`, 2019. Accessed: 19/04/2019.

[248] Gang Wang, Miao Zhang, Yun Zhu, Guqiao Ding, Da Jiang, Qinglei Guo, Su Liu, Xiaoming Xie, Paul K Chu, Zengfeng Di, et al. Direct growth of graphene film on germanium substrate. *Scientific reports*, 3, 2013.

[249] EH Hwang and S Das Sarma. Dielectric function, screening, and plasmons in two-dimensional graphene. *Physical Review B*, 75(20):205418, 2007.

[250] Marinko Jablan, Hrvoje Buljan, and Marin Soljačić. Plasmonics in graphene at infrared frequencies. *Physical review B*, 80(24):245435, 2009.

[251] Frank HL Koppens, Darrick E Chang, and F Javier Garcia de Abajo. Graphene plasmonics: a platform for strong light–matter interactions. *Nano letters*, 11(8):3370–3377, 2011.

[252] Qiaoliang Bao and Kian Ping Loh. Graphene photonics, plasmonics, and broadband optoelectronic devices. *ACS nano*, 6(5):3677–3694, 2012.

[253] Jianing Chen, Michela Badioli, Pablo Alonso-González, Sukosin Thongrattanasiri, Florian Huth, Johann Osmond, Marko Spasenović, Alba Centeno, Amaia Pesquera, Philippe Godignon, et al. Optical nano-imaging of gate-tunable graphene plasmons. *Nature*, 487(7405):77, 2012.

[254] Kinam Kim, Jae-Young Choi, Taek Kim, Seong-Ho Cho, and Hyun-Jong Chung. A role for graphene in silicon-based semiconductor devices. *Nature*, 479(7373):338–344, 2011.

[255] Zhipei Sun, Amos Martinez, and Feng Wang. Optical modulators with 2D layered materials. *Nature Photonics*, 10(4):227, 2016.

[256] Ming Liu, Xiaobo Yin, Erick Ulin-Avila, Baisong Geng, Thomas Zentgraf, Long Ju, Feng Wang, and Xiang Zhang. A graphene-based broadband optical modulator. *Nature*, 474(7349):64–67, 2011.

[257] Ming Liu, Xiaobo Yin, and Xiang Zhang. Double-layer graphene optical modulator. *Nano letters*, 12(3):1482–1485, 2012.

[258] Longhai Yu, Jiajiu Zheng, Yang Xu, Daoxin Dai, and Sailing He. Local and nonlocal optically induced transparency effects in graphene–silicon hybrid nanophotonic integrated circuits. *ACS nano*, 8(11):11386–11393, 2014.

[259] Ciyuan Qiu, Weilu Gao, Robert Vajtai, Pulickel M Ajayan, Junichiro Kono, and Qianfan Xu. Efficient modulation of 1.55 μm radiation with gated graphene on a silicon microring resonator. *Nano letters*, 14(12):6811–6815, 2014.

[260] Yunhong Ding, Xiaolong Zhu, Sanshui Xiao, Hao Hu, Lars Hagedorn Frandsen, N Asger Mortensen, and Kresten Yvind. Effective electro-optical modulation with high extinction ratio by a graphene–silicon microring resonator. *Nano letters*, 15(7):4393–4400, 2015.

[261] Yuanda Gao, Ren-Jye Shiue, Xuetao Gan, Luozhou Li, Cheng Peng, Inanc Meric, Lei Wang, Attila Szep, Dennis Walker Jr, James Hone, et al. High-speed electro-optic modulator integrated with graphene-boron nitride heterostructure and photonic crystal nanocavity. *Nano letters*, 15(3):2001–2005, 2015.

[262] Qing Hua Wang, Kourosh Kalantar-Zadeh, Andras Kis, Jonathan N Coleman, and Michael S Strano. Electronics and optoelectronics of two-dimensional transition metal dichalcogenides. *Nature nanotechnology*, 7(11):699, 2012.

[263] Xiaodong Xu, Wang Yao, Di Xiao, and Tony F Heinz. Spin and pseudospins in layered transition metal dichalcogenides. *Nature Physics*, 10(5):343, 2014.

[264] Jason C Reed, Alexander Y Zhu, Hai Zhu, Fei Yi, and Ertugrul Cubukcu. Wavelength tunable microdisk cavity light source with a chemically enhanced mos$_2$ emitter. *Nano letters*, 15(3):1967–1971, 2015.

[265] Sanfeng Wu, Sonia Buckley, John R Schaibley, Liefeng Feng, Jiaqiang Yan, David G Mandrus, Fariba Hatami, Wang Yao, Jelena Vučković, Arka Majumdar, et al. Monolayer semiconductor nanocavity lasers with ultralow thresholds. *Nature*, 520(7545):69, 2015.

[266] Charles Lin, Roberto Grassi, Tony Low, and Amr S Helmy. Multilayer black phosphorus as a versatile mid-infrared electro-optic material. *Nano letters*, 16(3):1683–1689, 2016.